People's Democratic Republic of Algeria

Ministry of Higher Education and Scientific Research

Yahia Fares University of Medea

Faculty of Technology

Department of Process and Environmental Engineering

Laboratory of Biomaterials and Transport Phenomena (LBMPT)

THESIS

Presented by:

Esam Ahmed Ahmed Ali Saleh

To obtain the degree of

DOCTOR in: Process Engineering

Specialization: Process Engineering

Thesis title

Modeling of Fluidization Using Artificial Intelligence

Defended on:

In front of the jury composed of:

Last and first name	Grade	Institution of affiliation	Designation
RAHAL Soufiane	Professor	Univ. of Medea	President
KHAOUANE Latifa	Professor	Univ. of Medea	Supervisor
AMMI Yamina	Professor	Univ. of Medea	Examiner 1
MOUSSAOUI Mohammed	Doctor	Univ. of Bouira	Examiner 2
HANINI Salah	Professor	Univ. of Medea	Invited

Academic year: 2025/2026

République Algérienne Démocratique et Populaire

Ministère de l'Enseignement Supérieur et de la Recherche Scientifique

Université Yahia Fares de Médéa

Faculté de la Technologie

Département de Génie des Procédés et de l'Environnement

Laboratoire des Biomatériaux et des Phénomènes de Transport (LBMPT)

THÈSE

FACULTE DE TECHNOLOGIE

Présentée par :

Esam Ahmed Ahmed Ali Saleh

Présentée en vue de l'obtention du diplôme de

Docteur en : Génie des Procédés

Spécialité : Génie des Procédés

Thème

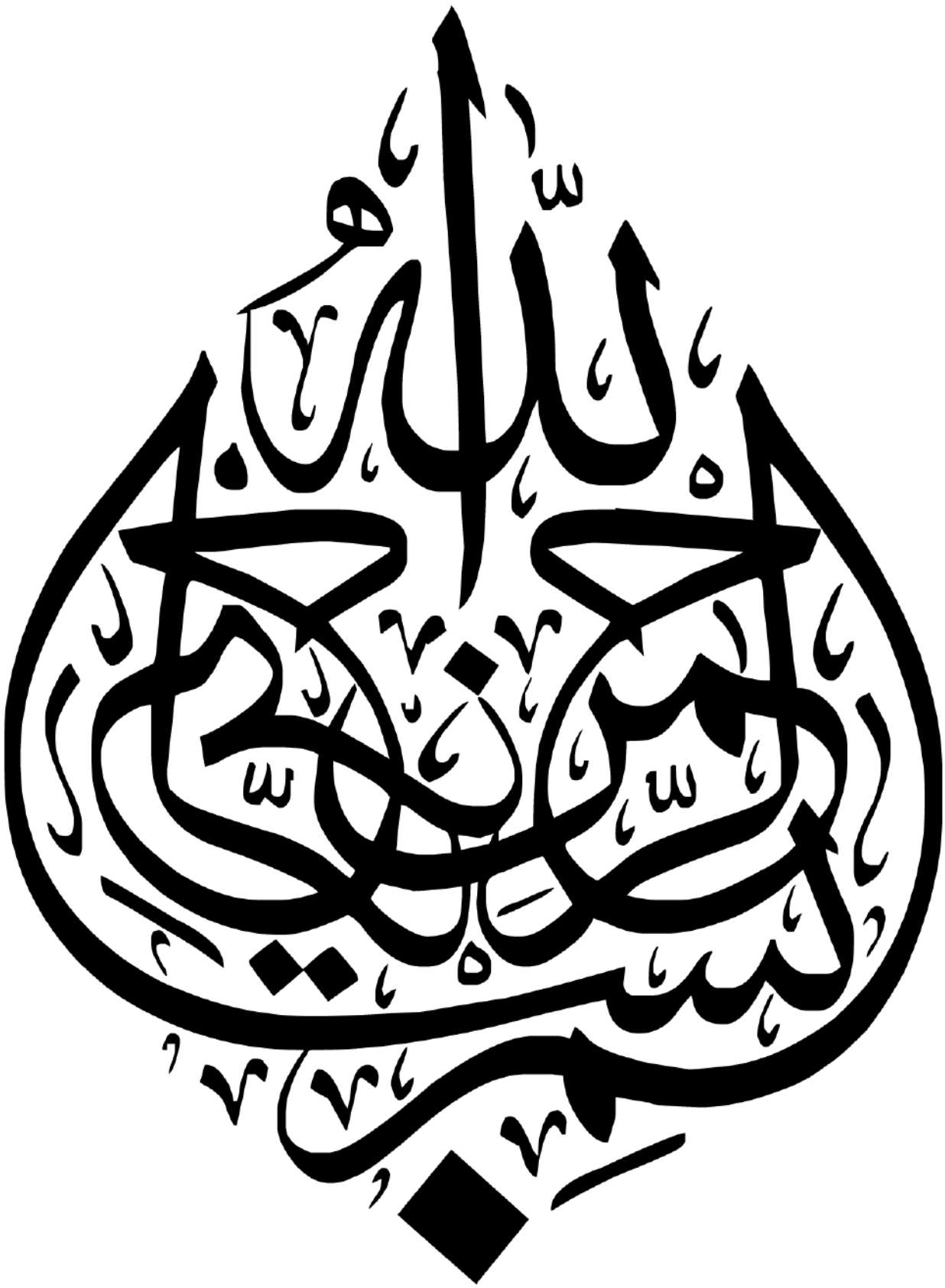
Modélisation de la fluidisation par intelligence artificielle

Soutenue le :

Soutenue publiquement devant le jury composé de :

Nom & Prénom	Grade	Institution d'affiliation	Designation
RAHAL Soufiane	Professeur	Univ. de Médéa	Président
KHAOUANE Latifa	Professeur	Univ. de Médéa	Directrice de thèse
AMMI Yamina	Professeur	Univ. de Médéa	Examinateur 1
MOUSSAOUI Mohammed	Docteur	Univ. de Bouira	Examinateur 2
HANINI Salah	Professeur	Univ. de Médéa	Invité

Année académique: 2025/2026



Dedication

To my dear parents, for their endless love and guidance,

To my beloved wife, for her constant support and understanding,

To all my brothers and sisters, for their encouragement and kindness,

To the entire Saleh Al-HatimY family, for their unwavering faith in me,

To all my friends, for their companionship and inspiration throughout this journey,

To all those whose support, whether near or distant, has contributed to the completion of this work.

ESAM

Thanks and gratitude

*First of all, I would like to thank Almighty **Allah** for all the wonders He does in my life and for giving me the courage, strength, and patience to complete this modest work.*

*I would like to express my deepest gratitude to my supervisor, Pr. **Latifa KHAOUANE**, for her valuable guidance, continuous support, and insightful advice throughout the course of this research. Her encouragement and expertise were essential to the successful completion of this work.*

*I would like to express my profound appreciation to Pr. **Hanini Salah** for his scholarly guidance, constructive feedback, and invaluable supervision throughout the development of this dissertation. His academic insight and professionalism have been instrumental in achieving the objectives of this research.*

*I would like to express my heartfelt appreciation to Pr. **RAHAL Soufiane** * for his valuable guidance, insightful comments, and continuous encouragement during the course of my research. His expertise and constructive advice have been of great importance to the completion of this work.*

*I would like to express my sincere gratitude to **Pr. **AMMI Yamina** ** for his valuable guidance, continuous support, and insightful advice throughout my research. His expertise and encouragement have been instrumental in the successful completion of this work.*

I would like to express my deepest gratitude to all those who have supported me both financially and morally throughout this work. Their encouragement, generosity, and unwavering belief in my abilities have been an invaluable source of strength and motivation. Without their assistance and understanding, the completion of this research would not have been possible.

ملخص

نمذجة التمييع بالذكاء الاصطناعي

الخصائص الهيدروديناميكية الأساسية في الأسرّة المميعة تتمثل في **أقصى انخفاض في الضغط**، ويرمز له بـ ** ΔP_{max} **، و**أدنى سرعة للتميع**، ويرمز لها بـ .** U_{mf} ** إنّ **التنبؤ الدقيق** بهذين المتغيرين ضروري لتعظيم **كفاءة الأداء** و**تصميم النظام. تُقدّم هذه الدراسة **منهجية جديدة** للنمذجة متعددة الطبقات وقد تم اشتقاق **عددين لابُعديين بالاعتماد على **معادلة إيرغن . يمثل **العدد الأول** (π_1) مقدار **فقدان الطاقة الناتج عن احتكاك المائع داخل السرير المميع**، ويُظهر علاقة واضحة مع **سرعة المائع** (U) في معادلة إيرغن، مما يجعله متوافقًا مع خصائص **العدد اللابعدي اللزج (أو عدد الاحتكاك).** أما **العدد الثاني** (π_2) فيعبّر عن **فقدان الطاقة الحركية داخل السرير**، ويُظهر **تناسبًا طرديًا مع مربع السرعة** (U^2) ، وهو ما يتوافق مع العدد اللابعدي العطالي. كما تم إدخال مفهوم **القطر الهيدروليكي لتمييز الاختلافات بين **الأسرّة المخروطية** و**الأسطوانية.** تم تحديد التكوين الأمثل لنموذج **الشبكة العصبية متعددة الطبقات) على أنه **هيكل تغذية أمامية مكوّن من طبقتين تحتوي على أربعة عشر عصبونًا مخفيًا وأظهرت الدراسة أن **دقة التنبؤ** لكل من Δp_{max} و U_{mf} بلغت **6.11%** و**9.77%** على التوالي، وفقًا لمؤشر **متوسط الفرق النسبي المطلق . كما أظهرت نتائج **متوسط مربع الخطأ قيمًا مقدارها **0.0146** و**2.9×10^{-4}** لكل من ΔP_{max} و U_{mf} على التوالي.

بينما بلغت قيم **الجذر التربيعي لمتوسط مربع الخطأ **0.120** و**0.0172** على التوالي وأظهرت قيم **معامل التحديد** (R^2) لكل من المتغيرين **0.935** و**0.989**، في حين بلغت **قيم معامل الارتباط** (R) **0.967** و**0.994** على التوالي وقد تمت **مقارنة نتائج المحاكاة** مع **البيانات التجريبية**، وأظهرت توافقًا عاليًا، مما يؤكد **صحة وموثوقية تقنية الشبكة العصبية متعددة الطبقات** (MLP) في التنبؤ بالخصائص الهيدروديناميكية للأنظمة المميعة.

الكلمات المفتاحية: فقدان الطاقة اللزجة والحركية، الشبكات العصبية الاصطناعية، سرعة التمييع الدنيا، القطر الهيدروليكي، أقصى انخفاض في الضغط، الأسرّة المميعة المخروطية والأسطوانية.

Summary

****Modeling of Fluidization Using Artificial Intelligence****

Fundamental hydrodynamic properties in the fluidized beds are the maximal pressure drop ΔP_{max} and the minimal fluidization velocity U_{mf}. Accurately forecasting these variables is necessary to maximize the functionality and architecture of this system. This study introduces a fresh technique for multilayer modeling. Two dimensionless numbers were generated by utilizing the Ergun equation. The initial numerical value, π_1, represents the energy dissipation from fluid friction within the fluidized bed. It demonstrates a clear relationship with the fluid velocity in the Ergun equation, denoted as "U." This characteristic is consistent with the properties of the dimensionless viscous (friction) number. In contrast, the second numerical value π_2 represents the dissipation of kinetic energy within the bed and exhibits a direct proportionality to U^2, akin to the dimensionless inertial number. Furthermore, the hydraulic diameter was created to differentiate between the conical and cylindrical beds. The ideal configuration for the multilayer perceptron (MLP) model was identified as a two-layer feedforward architecture comprising fourteen hidden neurons. The study determined that the precision of ΔP_{max} and U_{mf} was 6.11% and 9.77% using the Average Absolute Relative Difference (AARD) metric. Additionally, the Mean Squared Error (MSE) metric yielded values of 0.0146 and 2.9×10^{-4} for ΔP_{max} and U_{mf}, respectively. Furthermore, the Root Mean Squared Error (RMSE) metric resulted in values of 0.120 and 0.0172 for ΔP_{max} and U_{mf}, respectively. The R-squared values for the respective variables were 0.935 and 0.989. The correlation coefficients (R values) were also found to be 0.967 and 0.994, respectively. The findings obtained from the simulation were compared to the experimental data, indicating a significant level of agreement and confirming the correctness and dependability of the MLP technique.

KEYWORDS: dissipation of viscous and kinetic energy, artificial neural networks, minimum fluidization velocity, hydraulic diameter, maximum pressure drop, conical and cylindrical fluidized beds.

Résumé

Modélisation de la fluidisation par l'intelligence artificielle*

Les propriétés hydrodynamiques fondamentales dans les lits fluidisés sont la perte de pression maximale (ΔP_{max}) et la vitesse minimale de fluidisation (U_{mf}). La prévision précise de ces variables est essentielle pour optimiser les performances et la conception de ce système. Cette étude propose une nouvelle approche de modélisation multicouche. Deux nombres sans dimension ont été générés à partir de l'équation d'Ergun. Le premier nombre, π_1, représente la dissipation d'énergie due au frottement du fluide dans le lit fluidisé. Il montre une relation claire avec la vitesse du fluide dans l'équation d'Ergun, notée « U », ce qui est cohérent avec les caractéristiques du nombre visqueux (de frottement) sans dimension. En revanche, le second nombre π_2 représente la dissipation d'énergie cinétique dans le lit et est directement proportionnel à U^2, similaire au nombre inertiel sans dimension. De plus, le diamètre hydraulique a été introduit afin de distinguer les lits coniques des lits cylindriques.

La configuration optimale du modèle de perceptron multicouche (MLP) a été identifiée comme une architecture à deux couches à propagation avant comprenant quatorze neurones cachés. L'étude a montré que la précision des prédictions de ΔP_{max} et U_{mf} était respectivement de 6,11 % et 9,77 %, selon la métrique de la différence absolue moyenne relative (AARD). Par ailleurs, la métrique de l'erreur quadratique moyenne (MSE) a donné des valeurs de 0,0146 et $2,9 \times 10^{-4}$ pour ΔP_{max} et U_{mf}, respectivement. L'erreur quadratique moyenne racine (RMSE) a présenté des valeurs de 0,120 et 0,0172 pour ΔP_{max} et U_{mf}, respectivement. Les coefficients de détermination (R^2) obtenus pour ces variables étaient de 0,935 et 0,989, tandis que les coefficients de corrélation (R) étaient de 0,967 et 0,994.

Les résultats issus de la simulation ont été comparés aux données expérimentales, révélant un haut degré de concordance et confirmant ainsi la justesse et la fiabilité de la méthode MLP.

MOTS-CLÉS : dissipation de l'énergie visqueuse et cinétique, réseaux de neurones artificiels, vitesse minimale de fluidisation, diamètre hydraulique, perte de pression maximale, lits fluidisés coniques et cylindriques.

Table of Contents

Abbreviations and Greek letter i

General letters and Subscripts ii

List of tables iii

List of figures iv

General Introduction 1

Chapter I. An Overview of Fluidization Technology and Artificial Intelligence Applications

I.1. Introduction 4

I.2. Fluidized beds 7

I.2.1. Particle positions 8

I.3. Fluidization process 9

I.3.1. Key aspects of fluidization include 10

I.4. Chapter Objectives and Fundamental Principles 13

I.4.1. Classification of Fluidization Regimes 13

I.4.2. Comparison between cylindrical and conical fluidized beds 19

I.4.2.1. Geometry and Design: 19

I.4.2.2. Hydrodynamics: 19

I.4.2.3. Mixing and Segregation 20

I.4.2.4. Heat and Mass Transfer 21

I.4.2.5. Operational Behavior 22

I.5. Artificial neural Networks(ANNs) 22

I.5.1. Concept of Artificial Neural Networks (ANNs) 22

I.5.1.1. The Input Layer 23

I.5.1.2. Hidden Layer 23

I.5.1.3. The Output Layer 24

I.5.2. Rationale for Using Neural Networks 24

I.5.3. Machine Learning 25

I.5.3.1 Supervised Learning 26

I.5.3.2. Unsupervised Learning 27

I.5.4. Multilayer Perceptron (MLP) 27

I.6. The Role and Importance of MATLAB 2021 in this Study 28

I.7. The Role of STATISTICA 10 in this study 29

I.8. Conclusion 30

Chapitre II. Critical Evaluation of the Solution Utilized in This Dissertation

II.1. Introduction 31

II.2. Classification of Fluid Behavior 33

II**.2.1.** Overview of Newtonian Fluid Behavior 33

II.2.2. Key Properties of Newtonian Fluids 36

II.2.3. Applications 37

II**.**2.4. Non-Newtonian Fluids 37

II.2.4.1. Rheological Characteristics of Non-Newtonian Fluids 37

II.2.4.2. Time-Independent Rheological Behavior 38

II.2.4.3 Time-Dependent Rheological Behavior 39

II.2.4.4 Visco-elastic behavior 40

II.3. Conclusion 44

Chapter III. Materials and Methods

III.1. Introduction 45

III.2. Experimental Equations for Minimum Fluidization Velocity 47

III.3. Artificial neural Networks(ANNs) 48

III.3.1. Multilayer Perceptron (MLP) 50

III.4. Modelling procedure 50

III.4.1. Database collection 51

III.4.2. Training 51

III.5. conclusion 52

Chapter IV. Results and discussion

IV .1. Introduction 53

IV.2. Examination of the Correlation Matrix 53

IV.3. MLP Topology 55

IV.4. Model checking 64

IV.4.1. Estimating the Accuracy of the MLP Model employing data from experience 64

IV.4.2. Estimating the precision level of the MLP Model through Comparison with Previous *Research* 65

IV.5. Parametric study 67

IV.5.1. Influence of the Archimedes number on ΔP_{max} and U_{mf} 67

IV.5.2. The Impact of Viscous energy dissipation parameter on ΔP_{max} and U_{mf} 68

IV.5.3. The Impact of Kinetic Energy Dissipation parameter on ΔP_{max} and U_{mf} 70

IV.6. The mathematical expressions employed for the computation of error rates. 72

IV.7. Information necessary for the utilization of the developed MLP model... 72

IV.8. Conclusion 74

General conclusion and outlook 75

Appendix A. Part of the database used in this work. 89

Appendix B Additional results were obtained using the STATISTICA 10 software. 94

Abbreviations

AARD	Absolute average relative deviation
ANN	Artificial neural network
MLP	Multi-layer perceptron
MSE	Mean square error
R	Correlation coefficient
R^2	Coefficient of determination
RMSE	Root Mean square error

Greek letters

α	Angle with a gradual decrease, (^{o})
ε_0	Voidage of the Bed, (-)
μ_g	Viscosity of the Gas, (kg/m.s)
μ_e	Viscosity of the water in the ambient, (kg/m.s)
ρ_g	Density of the Gas, (kg/m^3)
ρ_e	Density of the water in the ambient, (kg/ m^3)
ρ_s	Density of the solide, (kg/ m^3)
ΔP_{max}	Maximum column pressure drop, (kpa)

General letters

A_r	Archimedes number $\frac{g\, d_p^3\ \rho_g (\rho_s - \rho_g)}{\mu_g^2}$ (−)
B_0	Bond number $(6(IPF)/\pi g\, \rho_s\, d_p^3)$ (-)
$D_{0,}\ D_1$	Inlet diameter, Upper diameter, (m)
d_p	Solid particle diameter, (m)
EU_{mf}	Euler number in minimum fluidization
F_r	Froude number $(U_{mf}/(g\, d_p)^{0.5})$ (-)
$H_{0,}\ H_L$	Incipient height, height of bed (m)
IPF	Inter particle forces, (nN)
$r_0;r_1$	Incipient radius, radius of bed $= (\frac{\mathbf{D_0}}{\mathbf{2}}, \frac{\mathbf{D_1}}{\mathbf{2}})$(m)
Re_{mf}	Reynolds number in minimum fluidization Velocity $\rho_g U_{mf}\ d_p/\mu_g$ (-)
U_{mf}	Minimum fluidization velocity, (m/s)

Subscripts

DB	Database
e, f, g, p, s	Water, fluid, gas, particle, solid
max	Maximum
mf	Minimum fluidization

List of tables

Chapitre II. Critical Evaluation of the Solution Utilized in This Dissertation

Table II.1. Values of viscosity for common fluids at room temperature 32

TableII.2. Examples of substances exhibiting non-Newtonian Fluid Behaviour. 32

TableII.3. Representative (approximate) values of Young's modulus (KIM, 2019) 41

Chapter III. Materials and Methods

Table III. 1. Obtainable correlations used for calculation of ΔP_{max} and U_{mf} in fluidized column. 46

Table III. 2. The structure of the model presented in the prediction process 51

Chapter IV. Results and discussion

Table IV. 1. The linear relationship's values. And the sensitivity analysis in Samples: Train, Test, Validation. 55

Table IV. 2. The statistically sound analysis. 62

TableIV. 3. The Predictive performance of several paradigms was evaluated in term of AARD. 66

TableIV. 4. The best MLP model's bias and Weight coefficients. 73

TableIV. 5. Statistical analysis of parameters 73

List of figures

Chapter I. An Overview of Fluidization Technology and Artificial Intelligence Applications

Figure.I.1. Artificial neural Networks(ANNs) 6

FigureI.2. Fixed bed composed of spherical particles with uniform diameter. 7

FigureI.3. A fluidized bed composed of uniformly sized spherical particles. On the left, the particles are displayed and color-coded according to their velocity. The fluid volume fraction is calculated at the center of the Y–Z plane. On the right, a visualization of the fluid velocity distribution across the Y–Z cross-section of the bed is presented. 8

FigureI.4. illustrates the variation in pressure (Δp) within the bed as a function of the fluidizing gas velocity." 14

FigureI.5. Fluidization regimes. 16

FigureI.6. Geldart classification. 18

FigureI.7. Schematic represents (a) conical, (b) cylindrical fluidized bed. 22

Figure I.8. Machine learning types. 26

Chapitre II. Critical Evaluation of the Solution Utilized in This Dissertation

Figure II.1. Schematic representation of a unidirectional shear flow. 34

Figure II.2. illustrates representative shear stress–shear rate relationships for two Newtonian fluids. 35

FigureII. 3 Stress components in three dimensional flow 36

FigureII .4. Qualitative flow curves of non-Newtonian fluids. 39

Figure II. 5. Typical first normal stress difference data for Polystyrene in toluene solutions 42

Figure II. 6. Typical second normal stress difference data for polystyrene in toluene solutions 43

Chapter III. Materials and Methods

Figure III. 1. The structure of the model presented in the prediction process. 50

Figure III.2. The architectural design of the model proposed. 52

Chapter IV. Results and discussion

Figure IV. 1.a. Related overall MSE of different MLP topologies in prediction experimental data of the U_{mf}. 56

Figure IV. 2.a. Related overall (a) MSE of different MLP topologies in prediction experimental data of the ΔP_{max}. 56

Figure IV. 3.b. Related overall RMSE of different MLP topologies in prediction experimental data of the U_{mf}. 57

Figure IV. 4.b. Related overall RMSE of different MLP topologies in prediction experimental data of the ΔP_{max}. 57

Figure IV. 5.c. Related overall AARD of different MLP topologies in prediction experimental data of the U_{mf}. 58

Figure IV. 6.c. Related overall AARD of different MLP topologies in prediction experimental data of the ΔP_{max}. 58

Figure IV. 7.d. Related overall R of different MLP topologies in prediction experimental data of the U_{mf}. 59

Figure IV. 8.d. Related overall R of different MLP topologies in prediction experimental data of the ΔP_{max}. 59

Figure IV. 9.e. Related overall R^2 of different MLP topologies in prediction experimental data of the U_{mf}. 60

Figure IV. 10.e: Related overall R^2 of different MLP topologies in prediction experimental data of the ΔP_{max}. 60

Figure IV. 11. Validation plot of MLP. 64

Figure IV. 12. The experimental data is contrasted with the data generated by the MLP for(a) U_{mf} and (b) ΔP_{max}. 65

Figure IV. 13. Impact of the Archimedes number on the (a) U_{mf} and (b) ΔP_{max} 68

Figure IV. 14. The impact of π_1 on the (a) U_{mf} and (b)ΔP_{max} 69

Figure IV. 15. The impact of π_2 on the (a) U_{mf} and (b) ΔP_{max} 71

General Introduction

Fluidization technology has become one of the most significant advances in modern process engineering, representing a cornerstone in numerous industrial applications such as chemical reactors, pharmaceutical production, food processing, energy conversion, and materials synthesis (J. Chen et al., 2015; X. Chen et al., 2019; Kato et al., 1989; Sutkar et al., 2013). The core theoretical concept of fluidization involves transforming the behavior of solid particles into that of a fluid by introducing a flowing gas or liquid medium (Chalermsinsuwan et al., 2012; Rajendra P. Chhabra et al., 2001). This transition creates a dynamic system with unique hydrodynamic characteristics that allow enhanced mixing, heat transfer, and mass transfer, which are essential for optimizing industrial performance (Atsamnia et al., 2017a, 2017b; Benimam et al., 2020). As a result, fluidized bed systems are widely employed for catalytic reactions, combustion, coating drying and gasification processes involved (Feng et al., 2017; Karimi et al., 2018; Maiti et al., 2018; Reina et al., 2000; Yates, 1988).

Despite their widespread use, fluidized bed reactors are inherently complex due to the simultaneous interaction of multiple phases—solid, liquid, and gas—combined with the influence of geometric, physical, and operational parameters. Understanding and predicting their hydrodynamic behavior remains a major scientific and a critical technical challenge (Mića et al., 2015)(Feng et al., 2017; Machac et al., 1993; Shahrbabaki et al., 2023). The accurate estimation of fundamental hydrodynamic variables, such as the minimum fluidization velocity (U_{mf}) and the maximum pressure drop (ΔP_{max}), is particularly crucial (Abd-Rabbo et al., 2020; Biswal, Bhowmik, et al., 1985; Fang et al., 2020; Jaiswal et al., 1992; Sutkar et al., 2013; Y. Zhou et al., 2020). These parameters determine the onset and stability of fluidization and directly affect the efficiency, energy consumption, and design of the equipment. However, because fluidization involves highly nonlinear phenomena such as particle–fluid interactions, turbulent flow, and energy dissipation, conventional empirical and theoretical correlations often fail to deliver satisfactory accuracy over a broad spectrum of operating conditions (Karimi et al., 2018; Olazar et al., 1994; Qiao et al., 2012).

In this context, the development of dimensionless parameters and advanced modeling techniques has emerged as an effective strategy for capturing the essential physics of fluidized beds. Dimensionless analysis enables the identification of scaling relationships among the governing variables—such as particle size, fluid properties, and geometric configurations—thereby facilitating the generalization of results across different systems (Delebarre, 2004; Reina

et al., 2000; *Minimum Fluidization Velocity and Expansion of Fluidisks Layers by UnGaZ V_ THONGLIMP, N. HIQUILY et C. LAGUERIE*, n.d.; Xu et al., 2009; D. Zhou et al., 2009). Classical models derived from the Ergun equation, among others, have been widely used to predict hydrodynamic behavior. Nevertheless, these models typically rely on simplifying assumptions that do not account for the inherent nonlinearities or the diverse geometries encountered in industrial-scale reactors, such as conical and cylindrical beds (D. Zhou et al., 2009).

To overcome these limitations, modern computational intelligence methods, particularly Artificial Neural Networks (ANNs), have gained increasing attention in recent decades (Rezrazi et al., 2016). ANNs offer a data-driven approach capable of modeling complex nonlinear relationships without the need for explicit analytical formulations. Among various architectures, the Multilayer Perceptron (MLP) has demonstrated superior performance in predicting nonlinear process behaviors due to its flexible structure and robust learning capability (Bar, Biswas, et al., 2010; Korkerd et al., 2021; Roubehie Fissa et al., 2019). By integrating experimental data with theoretical insights, neural network models can achieve high predictive accuracy for key parameters such as ΔP_{max} and U_{mf}, while reducing the dependency on empirical assumptions (Raza et al., 2021).

The integration of artificial intelligence with classical transport phenomena not only enhances prediction accuracy but also represents a paradigm shift in chemical and process engineering. Through intelligent modeling, researchers can now simulate the dynamic behavior of fluidized systems under a wide range of conditions, including those involving irregular particle shapes, diverse particle size distributions, and non-uniform bed geometries. Moreover, such hybrid approaches contribute to optimizing reactor design, minimizing energy losses, and improving operational safety and reliability (W. Bai et al., 2021; Chalermsinsuwan et al., 2012; KIM, 2019; Marahel et al., 2022; Raza et al., 2021).

In light of these advancements, the present study focuses on developing a novel modeling framework that combines dimensionless analysis with artificial neural networks to achieve precise estimation of fundamental hydrodynamic properties in gas–solid fluidized beds. Two new dimensionless parameters are formulated based on the Ergun equation to represent viscous and kinetic energy dissipation within the bed. By employing these parameters as independent variables in a multilayer perceptron (MLP) model, the study aims to predict the minimum

fluidization velocity (U_{mf}) and the maximum pressure drop (ΔP_{max}) for both conical and cylindrical configurations. This innovative approach not only enhances the predictive capability of existing models but also offers a generalized method adaptable to diverse system geometries and operating conditions (Rasteh et al., 2018).

Ultimately, the findings of this research contribute to a deeper understanding of fluidization hydrodynamics and provide a reliable computational tool for optimizing the design and operation of fluidized bed systems. The combination of dimensionless modeling and neural network techniques demonstrates the potential of artificial intelligence as a transformative element in modern process engineering, paving the way for more efficient, adaptable, and sustainable and energy-efficient industrial technologies (Aleksić et al., 2015; Bousselma et al., 2021)(Ammi et al., 2015; Hamadache et al., 2016; Roubehie Fissa et al., 2019; Saleh et al., 2023).

Chapter I

An Overview of Fluidization Technology and Artificial Intelligence Applications

I.1. Introduction

Fluidization is defined as the phenomenon in which a particulate solid system acquires fluid-like characteristics due to the upward flow of a gas or liquid medium. (Abd-Rabbo et al., 2020). It is extensively employed throughout various industrial sectors, including petrochemical manufacturing, food processing, chemicals, and pharmaceuticals (Bahramian, 2021; Korkerd et al., 2021; Mića et al., 2015).

Fluidization represents a transformative operation in particle–fluid systems in which a bed of granular solids behaves as a fluid when subjected to an upward-flowing gas or liquid stream (X. Chen et al., 2019). This transformation is achieved when The particles are suspended when the hydrodynamic forces imposed by the fluid exceed the combined effects of interparticle forces and the gravitational weight of the solid phase, circulate, and move freely in a quasi-fluid state. In this dynamic condition, the bed exhibits macroscopic properties similar to those of a liquid, such as the ability to flow, level out, and conform to the shape of its container (Shu et al., 2000)(Bahramian, 2021; Sutkar et al., 2013).

From a scientific standpoint, fluidization is governed by the balance between drag, buoyancy, and inertial forces, and its behavior can vary significantly depending on particle size, density, fluid viscosity, and operating velocity. As the flow increases beyond the minimum fluidization velocity, the bed undergoes several regimes—including bubbling, slugging, turbulent, and fast fluidization—each with distinct flow structures and stability attributes (J. Chen et al., 2015; Gernon et al., 2012; Han et al., 2020; Mathur et al., 1955). These regimes strongly influence gas–solid interactions, temperature distribution, reaction kinetics, and overall system performance (Yates, 1988).

The technological relevance of fluidization extends far beyond its basic hydrodynamic behavior (Fu et al., 2019; Gupta et al., 2009; Sau et al., 2007). Fluidized beds are valued for their exceptionally high rates of heat and mass transfer, uniform temperature distribution, and ability to handle large variations in feedstock composition (Machac et al., 1993; Machač et al., 1997; D. Wang et al., 2023). These attributes make them indispensable in energy production (e.g., combustion, gasification, pyrolysis of biomass and coal), environmental engineering (waste treatment, pollutant adsorption, catalytic oxidation), and advanced materials synthesis (nanoparticle production, coating processes, calcination).

In the pharmaceutical and food industries, fluidization enables precise control over drying, granulation, and encapsulation, which are essential for producing powders with consistent particle size, porosity, and mechanical strength (R. P. Chhabra, 1993). In the petrochemical sector, fluidized catalytic cracking (FCC) remains one of the most economically significant applications, converting heavy hydrocarbons into lighter and more valuable products through intensive gas–solid contact (Padhi et al., 2010).

Moreover, modern research continues to explore computational and data-driven approaches—including CFD modeling, discrete element methods (DEM), and artificial intelligence—to improve the prediction of fluidization behavior and optimize reactor design. These advancements highlight fluidization not merely as a classical engineering process, but as an evolving scientific field central to innovation across multiple industries (Abd-Rabbo et al., 2020; Davarpanah et al., 2021; El ajouri et al., 2022; Islam et al., 2021; Mehdizad et al., 2018).

Successful management and development of gas–solid fluidized beds necessitate an in-depth comprehension of the governing hydrodynamic mechanisms. (Abd-Rabbo et al., 2020). The hydrodynamic characteristics of a fluidized bed are controlled by an interplay of operational variables and governing factors (Bahramian, 2021; Korkerd et al., 2021). The interaction between geometric parameters and the mean particle size is critical in shaping the overall fluidization dynamics. Nevertheless, a complete understanding of fluidized bed behavior cannot be achieved through particle size analysis alone, as the bed configuration significantly influences the system's performance. Therefore, to improve fluid system design and optimize industrial operations, it is essential to thoroughly investigate the fluidization behavior exhibited by both conical and cylindrical beds (Mića et al., 2015).

The most critical parameters in fluidized bed applications are the maximum pressure drop (ΔP_{max}) and the minimum fluidization velocity (U_{mf}). Numerous studies have been conducted to investigate the fluidization characteristics and their underlying determinants. (El ajouri et al., 2022; Mića et al., 2015).

Neural networks represent a non-parametric computational framework that infers the intrinsic structure of datasets through a systematic learning procedure (Kamari et al., 2020; Marahel et al., 2022). Artificial neural networks leverage a structured interplay of weights and hidden neurons to model complex relationships, thereby demonstrating robustness in handling both

abundant and uncertain data. (Anbazhagan et al., 2020). Neural networks are well-suited for a wide range of applications, including regression, classification, time series analysis, and segmentation. Input data processed by neural networks is typically normalized to a standard range, often (0,1), to ensure proper scaling. Neural networks can be broadly categorized into multilayer perceptrons and radial basis function networks. Predictive capabilities may be realized through the use of a single network or an ensemble of networks, depending on the complexity of the task and the desired accuracy (Rama Sastry, 2022). The multi-layer perceptron (MLP), incorporating a non-linear feed-forward neural network (FFNN) topology, has emerged as a highly effective regression tool in diverse scientific and technical disciplines (Hamadache et al., 2016; Melzi et al., 2019; Rama Sastry, 2022).

Neural networks, also known as perceptrons, were first introduced in the early 1940s. Although they have existed for several decades, their significance in the field of artificial intelligence has only recently been fully realized. These networks are commonly regarded as nonlinear data representation systems that model the relationships among various data sources.

The canonical neural network architecture encompasses three primary components: an **input layer** for data entry, one or more **hidden layers** for intermediate processing, and an **output layer** for producing results. Data is initially received by the input layer and is then propagated sequentially through the hidden layers before reaching the output layer. This layer-by-layer transmission allows the network to extract complex features and patterns from the data.

The architecture of the neural network used in this work is detailed in the following sections (see Figure I.1).

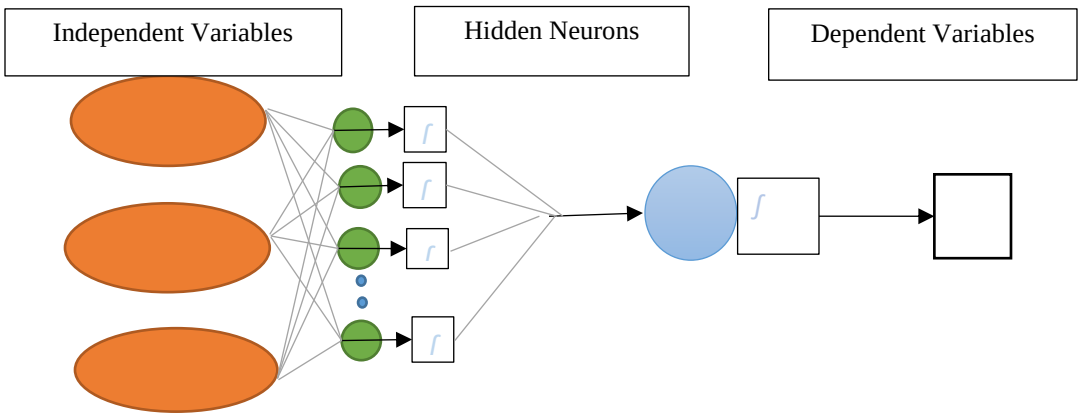
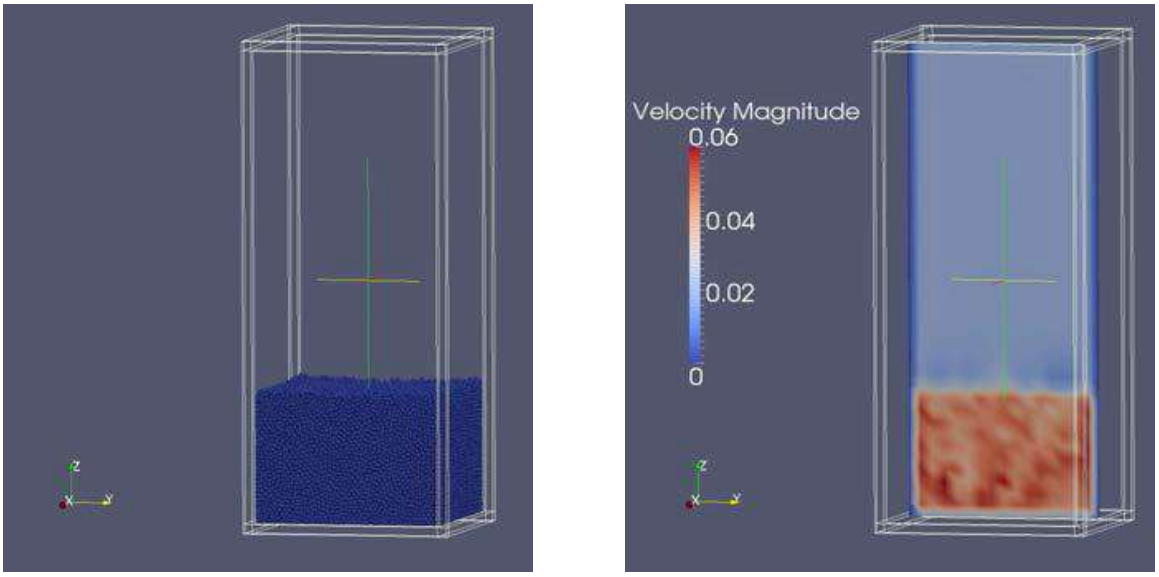


Figure.I.1. Artificial neural Networks(ANNs)

The prediction of minimum fluidization velocity (U_{mf}) has frequently been performed using feedforward neural networks (FFNN), as exemplified by the study of (Fu et al., 2019)' A feedforward neural network (FFNN) was employed to predict the minimum fluidization velocity (U_{mf}) in binary particle mixtures. The study demonstrated that the FFNN produced highly precise and accurate predictions. Overall, these results indicate that feedforward neural networks represent a promising tool for forecasting U_{mf} in fluidized bed reactors. However, the predictive accuracy of the network is strongly dependent on the quality and quantity of the training data used for model development.

I.2. Fluidized beds

Fluidized beds are systems in which one or more solid phases interact with a fluid phase—either a gas or a liquid—that is introduced from the bottom of the domain. The solid phase, often referred to as the dispersed phase, consists of numerous discrete particles that may differ in size. When these particles accumulate at the bottom of a container, they are collectively termed a "bed." The bed is described as "fixed" when the majority of the particles remain stationary at the base of the vessel (see FigureI.2.(a)) (KIM, 2019). In this state, the bed behaves similarly to a porous medium, allowing the continuous fluid phase to pass through it. As illustrated in FigureI.2.(b) (KIM, 2019), the fluid experiences an increase in flow velocity while moving through the bed due to a reduction in the cross-sectional area available for flow (Aguirre et al., 2024; KIM, 2019).



(a) Particle positions

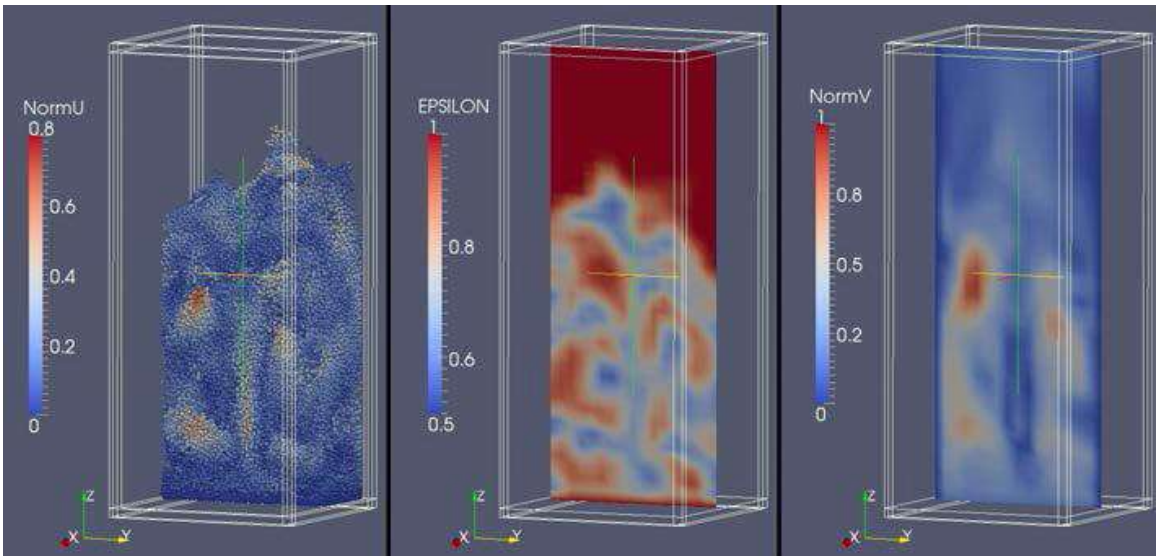
(b) Fluid velocity standard through the bed on a section YZ

FigureI.2. Fixed bed composed of spherical particles with uniform diameter. (Aguirre et al., 2024; KIM, 2019).

When the fluid velocity exceeds a certain critical value, the bed transitions into a dynamic state. This critical value is known as the **minimum fluidization velocity**, representing the threshold at which particle motion begins. As the fluid velocity surpasses this point, the particles within the dispersed phase become increasingly mobile. This leads to the formation of regions with lower particle concentration, allowing the continuous phase to pass through more easily. The resulting flow behavior resembles the formation of gas or liquid bubbles at the bottom of the bed, which rise slowly to the surface. As particles ascend and subsequently descend, the bed enters a fluidized state (see FigureI.3c.)

I.2.1. Particle positions

The spatial distribution of particles within a fluidized bed depends on several factors, including



FigureI.3. A fluidized bed composed of uniformly sized spherical particles. On the left, the particles are displayed and color-coded according to their velocity. The fluid volume fraction is calculated at the center of the Y–Z plane. On the right, a visualization of the fluid velocity distribution across the Y–Z cross-section of the bed is presented. (Aguirre et al., 2024; KIM, 2019).

fluid velocity, particle size, particle density, and the forces acting on the system. Typically, the arrangement of particles within the bed gives rise to three distinct zones (Aguirre et al., 2024; Dilmi et al., 2023).

- ✓ **Fixed Zone (Fixed Particle Zone):**

This is the region located at the bottom of the bed, where particles exhibit minimal movement. In this zone, particles tend to accumulate and form a densely packed layer, maintaining a relatively stable structure due to insufficient fluid velocity to initiate significant motion (Bouarra et al., 2024; KIM, 2019).

- ✓ **Expansion Zone (Fluidization Zone):**

Situated above the fixed zone, this region is characterized by a fluid velocity high enough to counteract the gravitational force acting on the particles. As a result, the particles become suspended within the fluid, exhibiting buoyant behavior similar to that observed in liquids. This region is commonly referred to as the expansion or fluidization zone (Irfan et al., 2012; KIM, 2019).

- ✓ **Pneumatic Transport Zone:**

Located at the upper section of the bed, this zone is defined by a high fluid velocity that enables the entrainment of particles into the fluid stream. In this region, particles are carried along by the flow, resulting in a pneumatic transport regime where particles remain suspended within the fluid (Irfan et al., 2012; KIM, 2019).

The distribution of particles across these regions is influenced by the specific characteristics of the fluidized bed, such as fluid velocity, particle size, particle density, and other related parameters. These factors play a critical role in the design, operation, and performance of fluidized beds, which are widely utilized in various process engineering applications (El-Moumen et al., 2024; KIM, 2019).

I.3. Fluidization process

Fluidization refers to the process by which a bed of solid particles is transformed into a fluid-like state through the upward flow of a fluid—typically a gas or liquid. This fluidization phenomenon is observed when the upward drag force imposed by the fluid matches the gravitational force on the particles, thereby maintaining them in a suspended state. Due to its unique characteristics, fluidization is extensively employed in a variety of industrial processes and has numerous practical applications (Biswal & Roy, 1985; El-Moumen et al., 2024; Zhang et al., 2022).

Fluidization refers to the hydrodynamic process in which a static bed of granular solid particles is transformed into a dynamic, fluid-like state by means of an upward-flowing fluid—typically a gas or a liquid (Chalermsinsuwan et al., 2012). This transition occurs when the drag force generated by the rising fluid becomes sufficient to counteract the gravitational force acting on the particles (J. Chen et al., 2015). At this critical point, the effective weight of the particles is reduced and they are lifted, loosened, and eventually suspended within the fluid stream (X. Chen et al., 2019). As the fluid velocity continues to increase beyond the minimum fluidization

velocity, the particles exhibit vigorous mixing, enhanced mobility, and collective behavior that closely resembles that of a boiling liquid (Leturia et al., 2014).

The unique characteristics of fluidization—such as excellent mixing, high surface-area contact, rapid heat and mass transfer, and uniform temperature distribution—make it highly advantageous for a wide range of industrial applications The work reinforces the need for context-specific selection of correlations, particularly for small particles where interparticle forces and cohesive effects may become significant (Liu et al., 2023). Fluidized beds are widely utilized in catalytic cracking, combustion, drying, gasification, granulation, coating, polymerization, and many other operations where efficient gas–solid interactions are essential (D. Bai et al., 1999). Their ability to handle large throughput, maintain stable operating conditions, and adapt to different particle sizes and material properties has contributed to the widespread adoption of fluidization technology across chemical, petrochemical, environmental, pharmaceutical, and energy-related industries (Felipe et al., 2007).

I.3.1. Key aspects of fluidization include:

- **Minimum Fluidization Velocity:** This refers to the critical fluid velocity at which a bed of solid particles begins to exhibit fluid-like behavior. Below this threshold, the particles remain stationary or form a compact, densely packed structure (KIM, 2019; Shahrbabaki et al., 2023). This parameter denotes the critical superficial fluid velocity at which a packed bed of solid particles transitions from a fixed state to a fluidized state, thereby beginning to exhibit fluid-like behavior (Khani, 2011; Mathur et al., 1955). Below this threshold velocity, the drag force exerted by the fluid is insufficient to counterbalance the weight of the particles, causing them to remain essentially immobile or arranged in a compact, densely packed configuration (Karimi et al., 2018; Rasteh et al., 2015; Shaul et al., 2012). In this regime, the bed behaves similarly to a static porous medium, with limited particle mobility, minimal mixing, and restricted gas–solid contact. Only when the fluid velocity reaches the minimum fluidization point do the hydrodynamic forces overcome interparticle friction and gravitational forces, enabling the onset of particle suspension, enhanced mixing, and the characteristic dynamics of a fluidized state (Abd-Rabbo et al., 2020; Feng et al., 2017; Gernon et al., 2012).

- **Uniform Particle Suspension:** In a fluidized bed, the particles are uniformly dispersed within the fluid, resulting in a homogeneous suspension (W. Bai et al., 2021). This uniform distribution enhances the efficiency of processes such as chemical reactions, drying, and heat transfer, as it provides a large surface area for interaction between the particles and the fluid (Liu et al., 2023). In a fluidized bed, the solid particles become uniformly dispersed and (Heddam, 2016)within the upward-flowing fluid, creating a (Y. Zhou et al., 2019)and homogeneous mixture that resembles the behavior of a fluid (Gao et al., 2022). This uniform distribution significantly enhances process efficiency by maximizing the interfacial surface area available for gas–solid interaction. As a result, operations such as chemical reactions, drying, combustion, and heat transfer occur more rapidly and uniformly compared to fixed or packed beds (Davarpanah et al., 2021). The intimate contact between particles and the fluid promotes superior mixing, reduces concentration and temperature gradients, and facilitates highly efficient mass and energy transport (Anbazhagan et al., 2020). These characteristics make fluidized beds particularly advantageous in industrial applications where high reaction rates, thermal uniformity, and continuous operation are essential.

- **Heat and Mass Transfer:** Fluidized beds are widely acknowledged for their superior heat and mass transfer characteristics, which arise from the unique fluid-like behavior of the particle bed (Rajendra P. Chhabra et al., 2001; Laidi et al., 2013). The continuous suspension and vigorous mixing of solid particles within the upward-flowing fluid create highly dynamic conditions that minimize concentration and temperature gradients throughout the bed. Additionally, the extensive interfacial surface area generated by the dispersed particles significantly enhances the rates of convective and diffusive transport between the solid and fluid phases (Aghajani et al., 2004; Sutkar et al., 2013). These attributes enable rapid and uniform distribution of heat and mass, improving process efficiency in applications such as drying, catalytic reactions, combustion, and chemical synthesis (Aghajani et al., 2004). The combination of high turbulence, uniform particle suspension, and extensive gas–solid contact makes fluidized beds particularly effective for processes that demand precise control of temperature, reactant distribution, and overall transfer rates (Shahrbabaki et al., 2023).

- **Applications:** Fluidized beds are employed across a wide range of industries, including chemical engineering, petrochemicals, pharmaceuticals, food processing, and environmental engineering (Reina et al., 2000). Common applications include catalytic cracking, combustion, drying, and gas-solid interactions (Turki et al., 2008). Fluidized beds are utilized extensively across numerous industrial sectors due to their superior gas–solid contact efficiency, excellent mixing characteristics, and ability to operate under a wide range of thermal and chemical conditions (Biswal, Bhowmik, et al., 1985). In chemical engineering and petrochemical industries, fluidized beds play a central role in catalytic cracking, polymerization, gasification, and sorption processes, where high reaction rates and uniform temperature distribution are essential (Tannous et al., 1994). In the pharmaceutical and food processing sectors, fluidized beds are employed for drying, coating, granulation, and agglomeration of particulate materials, ensuring consistent product quality and controlled processing conditions. Environmental engineering also benefits significantly from fluidized bed technology, particularly in wastewater treatment, flue gas desulfurization, incineration, and biomass combustion, where efficient mass transfer and stable operation are required (Khan et al., 1990). Overall, the versatility and scalability of fluidized beds make them a critical unit operation in modern industry, supporting a broad spectrum of applications involving complex gas–solid interactions (Felipe et al., 2007).
- **Types of Fluidized Beds:** Fluidized beds can be classified into several distinct types, including bubbling fluidized beds (BFBs) and circulating fluidized beds (CFBs), among others (Weber et al., 2013). Each configuration exhibits unique hydrodynamic characteristics, particle behavior, and operational regimes, which make them particularly suitable for specific industrial applications. Bubbling fluidized beds are characterized by relatively low gas velocities, which result in the formation of gas bubbles within the particle bed (Padhi et al., 2010; Shaul et al., 2012; Yates et al., 1994). This regime promotes good solids mixing and uniform temperature distribution, making BFBs ideal for processes such as drying, coating, and moderate-scale catalytic reactions. In contrast, circulating fluidized beds operate at higher gas velocities, causing particles to be continuously entrained and recirculated between the reactor and a particle separator (D. Bai et al., 1999; Gernon et al., 2012). This dynamic regime enables enhanced gas–solid

contact, higher mass and heat transfer rates, and improved scalability, which is advantageous for applications such as large-scale combustion, gasification, and catalytic cracking. The selection of a particular fluidized bed type is therefore determined by the desired balance between residence time, mixing intensity, heat and mass transfer efficiency, and the physical characteristics of the solid particles involved (El-Moumen et al., 2024; Liu et al., 2023).

- **Fluidization Regimes:** The behavior of a fluidized bed is influenced by the fluid velocity, which determines the fluidization regime. These regimes include fixed bed, minimum fluidization, intermediate fluidization, complete fluidization, and pneumatic transport (entrainment), each occurring at different fluid velocities.

In summary, fluidization is a versatile and widely utilized technique, offering significant advantages in mixing, heat transfer, and mass transfer, making it ideal for numerous industrial applications.

I.4. Chapter Objectives and Fundamental Principles

In this section, we provide a general overview of the principal characteristics associated with fluidized beds, while also identifying the key challenges that persist despite decades of extensive research. These ongoing challenges underscore the continued relevance of academic research in this area, particularly efforts aimed at deepening our fundamental understanding and enhancing the modeling of fluidized bed behavior, ultimately with the goal of improving their industrial performance. For readers seeking more detailed information, we recommend consulting both comprehensive review texts and the extensive specialized literature available in this domain.

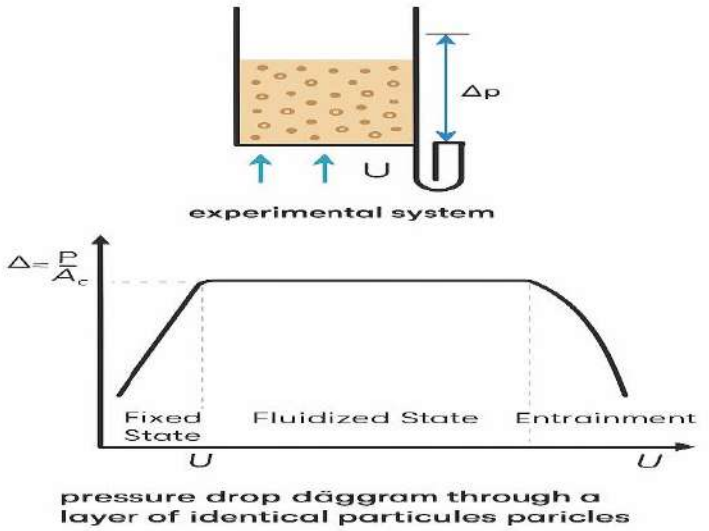
I.4.1. Classification of Fluidization Regimes

In general terms, when considering a particle bed supported by a porous distributor through which a gas—referred to as the fluidizing gas—is injected. The initiation of fluidization can be identified through the variation of pressure drop (ΔP) across the bed with respect to the superficial gas velocity. (see FigureI.4). At relatively low gas velocities, the pressure drop increases approximately linearly with velocity U, and the bed behaves similarly to a fixed porous medium. As U continues to increase, a critical threshold is reached, beyond which particle vibrations and bed expansion become evident (Dilmi et al., 2023). The pressure drop then reaches

a maximum before decreasing, stabilizing at a value roughly corresponding to the weight of the solid particles per unit cross-sectional area of the bed, P/A_C (Liu et al., 2023).

Beyond a critical velocity, denoted as U_{mf} , the particles no longer interact with one another and become fully suspended, at which point the bed exhibits fluid-like behavior. This condition is referred to as the fluidization of the bed. Subsequent to this transition, various fluidization regimes can be defined based on the velocity of the fluidizing gas, U_{mf}. "Refer to FigureI.5. where it is assumed that the gas is introduced into the lower section of the cell via a grid-like apparatus (Zhang et al., 2022)."

"First regime ($U_{mf} < U < U_{mb}$): Once the minimum fluidization velocity is exceeded, the



FigureI.4. illustrates the variation in pressure (Δp) within the bed as a function of the fluidizing gas velocity. (Marseille, n.d.)

fluidized bed experiences a homogeneous expansion with increasing gas velocity. This stage is referred to as the particulate fluidization regime. The upper surface of the bed remains well-defined, and the particles exhibit only low-amplitude movements (Vandeputte et al., 2023)(Marseille, n.d.)." "Second regime ($U_{mb} < U < U_{mp}$): In this regime, gas bubbles originate near the gas distribution grid at the bottom of the cell, ascend through the bed, and grow primarily through coalescence before bursting at the upper surface. The bed surface remains relatively well-defined between successive bubble bursts. This stage is identified as the bubbling

fluidization regime, during which sensitive pressure sensors are capable of detecting pressure fluctuations of significant amplitude (D. Wang et al., 2023)."

"Third regime ($U_{mp} < U < U_{ft}$): In this regime, the bubble diameter becomes comparable to the dimensions of the cell, leading to an alternation between large gas bubbles and a dense bed phase. This stage is referred to as the pistoning regime. The bed surface oscillates with a very regular frequency, and the pressure fluctuations are highly pronounced. For these first three regimes, it is generally accepted that the medium should be treated as a truly two-phase system, both in the interpretation of experimental results and in numerical modeling, regardless of the level of model sophistication (Shahrbabaki et al., 2023)."

"Fourth regime ($U_{ft} < U < U_{fr}$): In this regime, the bed consists of small gas and solid phase elements that move rapidly back and forth, making it difficult to clearly distinguish the bed surface. Pressure fluctuations are of low amplitude. This stage is known as the turbulent fluidization regime (Shahrbabaki et al., 2023)."

"Fifth regime ($U_{fr} < U.$): In this regime, particles are entrained by the gas flow in a highly dilute form and are carried out of the cell, requiring continuous replacement. Small clusters of descending particles can still be observed near the walls (El-Moumen et al., 2024). The concept of a distinct bed surface completely disappears, and the pressure drop experienced by the gas becomes very low. This stage is referred to as the rapid fluidization regime. For these last two regimes, in contrast to the previous ones, it is generally accepted that the system behaves as a single-phase medium, given that the residual gas bubbles are either highly deformed and irregular (in turbulent fluidization) or very small and difficult to distinguish from solid clusters (in rapid fluidization) (Kelfoun et al., 2023)."

It should be emphasized, however, that not all of the fluidization regimes described above are systematically observed as the gas velocity through the cell increases. The transitions between these regimes depend not only on the characteristics and properties of the gas and solid particles, but also on various other factors, including the bed diameter, bed height, the type of gas distributor employed, and the presence of internal structures such as baffles or transfer surfaces (J. Wang et al., 2023)."

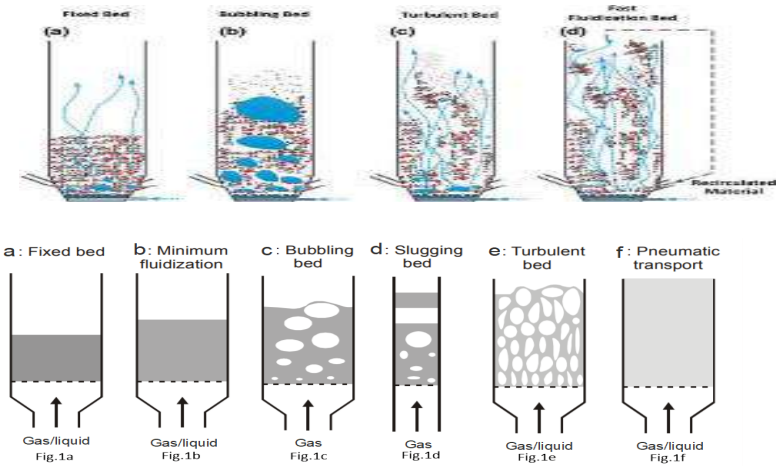


Figure I.5. Fluidization regimes. (Marseille, n.d.)

In many systems, it is particularly difficult to distinguish between U_{mf} and U_{mb}, resulting in the absence of a clearly defined particulate fluidization regime. Similarly, when the cell diameter is large or the bed height is low, the swabbing threshold, U_{mp}, may not be identifiable, and the same holds true for the turbulent fluidization threshold, U_{mt}. Additionally, the minimum velocity required to achieve rapid fluidization depends on the particle feed rate into the cell. Apart from U_{mb} and U_{ft}, which are generally well-defined, the other transitions between fluidization regimes tend to occur progressively rather than abruptly (Frikha, 2023)."

Moreover, since fluidization depends directly on the balance between the particles' own weight and the opposing forces within the fluid, and given that the forces acting on a particle—typically assumed to be spherical for simplicity—are influenced by the associated Reynolds number, the fundamental principles of fluidization outlined above cannot be universally applied to all types of particles. To address these variations, Geldart proposed in 1986 a classification system for powders based on their size and density, which is now widely known as the Geldart classification (Salehi et al., 2023). This system categorizes powders according to their behavior in a fluidized bed (see FigureI.6), distinguishing four groups based on particle density and average size, with additional dependence on the fluid's density according to the concept of apparent weight (Amiri et al., 2023)."

Class A particles have diameters ranging from 20 to 100 μm and densities not exceeding 1500 $kg \cdot m^{-3}$. In this class, fluidization is relatively easy and predominantly of the particulate type

(between U_{mf} and U_{mb}), characterized by significant bed expansion compared to the fixed state, with a possible tendency for the formation of preferential channels (known as 'foxing'). Beyond U_{mb}, small gas bubbles begin to form. Upon cessation of the gas flow, defluidization occurs slowly, a phenomenon referred to as deaeration. Typical examples of Class A particles include hydrocarbon cracking catalysts (Feng et al., 2017)."

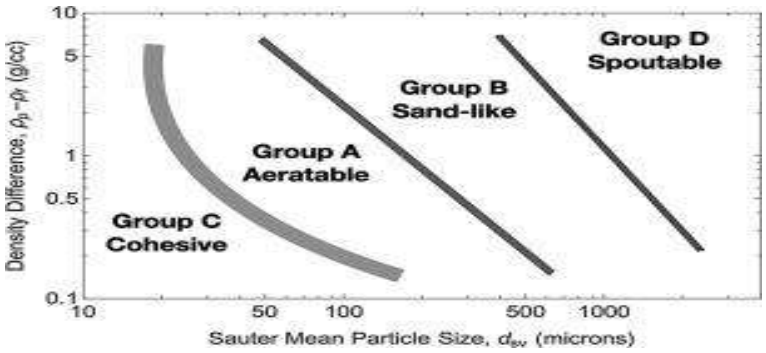
"Class B particles have diameters between 80 and 800 μm, with densities ranging from 1500 to 4000 kg·m^{-3}. Fluidization is also relatively easy for this class; however, bubbling occurs immediately upon the onset of fluidization, and the risk of channeling is low. Defluidization for Class B particles is rapid. Sand is a typical example of materials belonging to this category (Abd-Rabbo et al., 2020)." "The boundary between Classes A and B is defined by the following equation:" (I.1)

$$\rho_p - \rho_g = 44000 \frac{\rho_g^{0.1} \mu_g^{0.9}}{g d_p} \qquad \text{(I.1)}$$

"Class C particles have diameters smaller than 30 μm and include highly cohesive powders, such as flour or talc, for which fluidization is extremely difficult. To prevent the formation of preferential channels (foxing), fluidization must be assisted by mechanical agitation or vibration of the bed. The bed expansion in this class is minimal. The boundary between Classes A and C is not sharply defined, as it depends particularly on factors such as the gas humidity and the resistivity and relative permittivity of the particles."

"Class D particles have diameters greater than 800 μm and/or exhibit high densities. Although fluidization is possible for this type of particle, it is generally preferable to employ specialized techniques, such as jet beds. Typical examples of Class D materials include cereals and shot. The boundary between Classes B and D is determined by the following relationship:"

$$\rho_p - \rho_g = d_p^{-2} 10^{-3} \qquad \text{(I.2)}$$



FigureI.6. Geldart classification. (Marseille, n.d.)

Finally, the following table summarizes the key characteristics distinguishing the various fluidization regimes and their principal properties. In this table, the slip velocity is defined as $(U/\varepsilon) - G_S/(\rho_p(1-\varepsilon))$ where β represents the mean void fraction and Gs the net solid flow rate, while the slip rate is given by $U\rho_p (1-\varepsilon)/(G_S\varepsilon)$. A so-called high-density rapid fluidization regime has recently been identified, exhibiting properties that differ slightly from those of the conventional rapid fluidization regime. However, due to the limited amount of available data and the ongoing debate regarding its specific characteristics, no distinction between these two regimes will be made in the following discussion (D. Bai et al., 1999; Davarpanah et al., 2021).

The fluidization criteria and classifications previously introduced from a phenomenological perspective—grounded in experimental observations—will now be revisited through a more rigorous analysis based on the fundamental principles governing two-phase flow systems. Subsequently, we will present the principal modeling approaches, which have been primarily developed for the regimes of bubbling fluidization, piston flow, rapid fluidization, and turbulent fluidization, as these constitute the most prevalent configurations encountered in industrial applications. The chapter will conclude with an exploration of the potential of direct numerical simulations (DNS) and large-eddy simulations (LES) to investigate the underlying physical mechanisms in simplified configurations (Islam et al., 2021). These advanced computational methods aim to enhance our understanding of the more complex and insufficiently characterized physical terms—particularly those associated with interphase friction and related phenomena particularly those associated with interphase friction, energy exchanges between solid particles

and the carrier fluid, the effects of particle size distributions, and the mechanisms and conditions that promote particle aggregation, among other related phenomena (El ajouri et al., 2022).

I.4.2. Comparison between cylindrical and conical fluidized beds

I.4.2.1. Geometry and Design:

A cylindrical fluidized bed features a straight, vertical column characterized by a constant cross-sectional area along its height (Wong, 2002). This uniform geometry simplifies both the construction and the hydrodynamic modeling of the system, as the flow behavior remains relatively predictable across the bed. Moreover, the constant diameter facilitates straightforward scale-up for industrial applications, since geometric similarity and flow conditions can be maintained more easily when transitioning from laboratory to pilot or full-scale units (Tangier et al., 2012). As a result, cylindrical beds are commonly employed in various chemical, petrochemical, and environmental processes where operational stability and design simplicity are essential (Khani, 2011).

In contrast, a conical fluidized bed is designed with a gradually tapered shape, where the diameter decreases from the bottom toward the top (D. Zhou et al., 2009). This non-uniform cross-section introduces a continuously varying flow area that significantly affects the internal hydrodynamics (Mehdizad et al., 2018). The expanding or contracting pathways for gas–solid flow lead to spatial changes in velocity distribution, pressure gradients, and particle–fluid interaction forces. Consequently, conical beds often exhibit enhanced gas–solid mixing, more uniform fluidization at lower gas velocities, and reduced tendencies for channeling or slugging compared to their cylindrical counterparts (X. Chen et al., 2019). Additionally, the geometric divergence promotes smoother transitions between flow regimes and can improve operational efficiency in processes requiring stable fluidization over a broad range of operating conditions. For these reasons, conical fluidized beds have gained increasing attention in research and industrial applications seeking improved performance, energy efficiency, and flexibility in handling particles of varying sizes and densities (Esam Saleh et al., 2021)(X. Chen et al., 2019; Padhi et al., 2010).

I.4.2.2. Hydrodynamics:

In cylindrical fluidized beds, the superficial gas velocity generally remains constant along the entire height of the bed due to the uniform cross-sectional area (Khani, 2011). While this

geometric simplicity aids in design, it can also introduce operational challenges, particularly as the system is scaled up. The constant velocity profile may result in non-uniform gas–solid interactions, which increases the likelihood of undesirable hydrodynamic phenomena such as channeling, slugging, and dead zones (Biswal, Bhowmik, et al., 1985; Peng et al., 1997; D. Zhou et al., 2009). These instabilities are especially pronounced in large-diameter beds, where radial maldistribution of gas flow can become significant. As a result, maintaining homogeneous fluidization in cylindrical configurations often requires higher gas velocities or additional mechanical aids, which in turn may increase energy consumption and operational complexity (Ali Reza et al., 2010).

Conversely, conical fluidized beds display a gradually decreasing superficial gas velocity along the bed height, owing to the continuously narrowing cross-sectional area from the base toward the top (Jing et al., 2000). This geometric design induces a natural redistribution of gas flow, which enhances gas–solid contact and mitigates many of the instabilities commonly encountered in cylindrical beds. The reduction in gas velocity promotes a smoother transition between fluidization regimes and contributes to a more uniform suspension of particles across the bed (Jing et al., 2000). Additionally, the improved hydrodynamic stability reduces the potential for channeling and slugging, thereby ensuring more consistent bed behavior over a wider range of operating conditions. This inherent stability makes conical fluidized beds particularly advantageous for processes requiring precise control of particle residence time, heat transfer, and reaction kinetics (El ajouri et al., 2022).

I.4.2.3. Mixing and Segregation:

Cylindrical fluidized beds frequently exhibit limited solids mixing, particularly when operating with particle systems that have broad size or density distributions (Khani, 2011). The uniform cross-sectional geometry leads to a relatively constant gas velocity, which may be insufficient to fully suspend heavier or larger particles (D. Zhou et al., 2009). As a consequence, particle segregation becomes more pronounced, with coarse or dense particles tending to accumulate near the bottom of the bed while finer particles are preferentially transported upward (Padhi et al., 2010). This segregation not only reduces mixing efficiency but can also negatively impact heat and mass transfer rates, chemical reaction uniformity, and overall process stability. In industrial applications, such mixing deficiencies may necessitate additional energy input or mechanical intervention to achieve acceptable performance (D. Zhou et al., 2009).

In contrast, conical fluidized beds provide inherently superior gas–solid contact and enhanced particle mixing due to their continuously varying cross-sectional area and the associated changes in flow dynamics along the bed height(D. Zhou et al., 2009). The gradual reduction in diameter creates a spatially varying gas velocity profile, which improves particle circulation patterns and promotes more uniform suspension of both fine and coarse particles(Biswal, Bhowmik, et al., 1985). This geometric effect reduces the likelihood of particle stratification and encourages more vigorous lateral and axial mixing(Peng et al., 1997). As a result, conical beds tend to maintain more homogeneous solids distribution and improved hydrodynamic stability, even when handling materials with substantial size or density differences(Ali Reza et al., 2010). These advantages make conical configurations particularly suitable for applications that demand high mixing efficiency, such as catalytic reactions, drying, coating, and thermochemical processes.(Davarpanah et al., 2021).

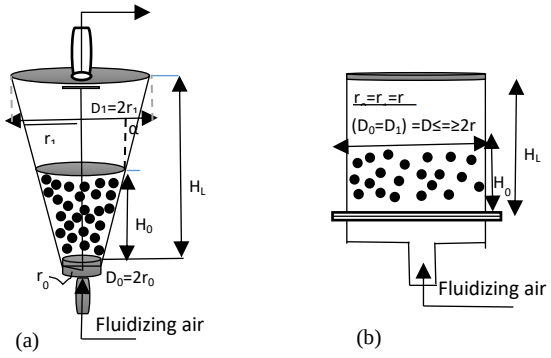
I.4.2.4. Heat and Mass Transfer:

From a heat and mass transfer perspective, conical fluidized beds generally provide more uniform operating conditions and improved contact efficiency between the gas phase and solid particles (Rajendra P. Chhabra et al., 2001). The gradual decrease in cross-sectional area along the bed height induces a continuously varying gas velocity, which minimizes the formation of stagnant regions and enhances overall mixing intensity (Geldart, 2004). This dynamic flow environment facilitates more homogeneous temperature distribution, reduces thermal gradients, and supports efficient diffusion and convective transport mechanisms (R. P. Chhabra, 1993). Consequently, conical beds are less prone to the development of dead zones, localized deficiencies in gas–solid interaction, or areas where heat transfer may be hindered (Aghajani et al., 2004; Laidi et al., 2013; Sutkar et al., 2013). These characteristics make them highly suitable for thermally sensitive processes, catalytic systems, and operations requiring consistent process conditions (Abd-Rabbo et al., 2020).

Although cylindrical fluidized beds are capable of achieving high heat and mass transfer rates under ideal conditions, they are more vulnerable to hydrodynamic irregularities due to their constant cross-sectional geometry (R. P. Chhabra, 1993; Marahel et al., 2022). The uniform gas velocity often leads to non-uniform mixing patterns, increasing the likelihood of localized issues such as hot spots, channeling, or bypassing of the fluidizing medium. These effects can cause

uneven temperature profiles, reduced reactor efficiency, and, in extreme cases, lead to degradation of catalysts or thermal runaway in reactive systems (Aghajani et al., 2004; Khani, 2011; Padhi et al., 2010; Sutkar et al., 2013; D. Zhou et al., 2009) Therefore, while cylindrical beds remain widely used in industry, their performance in heat and mass transfer is more sensitive to operating parameters and may require stricter control measures compared to their conical counterparts (Islam et al., 2021; M Mandour et al., 2020).

I.4.2.5. Operational Behavior:



FigureI.7. Schematic represents (a) conical, (b) cylindrical fluidized bed.

Cylindrical fluidized beds are well-established in industries like petrochemicals, pharmaceuticals, and catalysis due to their straightforward design and extensive research base. However, they tend to entrain more particles due to uniform velocity, which can cause losses and require additional separation systems. Conical beds, with their velocity gradient, reduce particle entrainment and are especially useful in applications like biomass gasification and fine powder processing where stability and reduced carryover are important (An et al., 2022).

I.5. Artificial neural Networks(ANNs)

I.5.1. Concept of Artificial Neural Networks (ANNs)

ANNs are computational systems that emulate the structure and operational principles of biological neural networks. ANNs adapt their internal structure based on the relationship between input and output data—essentially "learning" from the data they process. This adaptability allows the network to modify its configuration in response to the flow of information (Melzi et al., 2019).

Functioning as nonlinear statistical modeling tools, ANNs are employed to characterize complex relationships between inputs and outputs or to identify underlying patterns within data. The term "neural network architecture" is also commonly used to refer to ANN configurations (Roubehie Fissa et al., 2019).

Due to their remarkable ability to derive meaning from complex, ambiguous, or noisy data, neural networks are well-suited for pattern recognition and trend analysis tasks that may exceed the capabilities of human analysts or conventional computational systems. Once trained, an ANN can act as a specialized "expert" within the domain of data on which it has been trained (Hamadache et al., 2016).

I.5.1.1. The Input Layer

In a neural network, the input layer comprises a collection of artificial neurons specifically designed to receive, encode, and transmit data from the external environment into the internal computational structure of the network (Petrović et al., 2011). This layer functions as the primary interface between raw input variables and the deeper processing units, ensuring that each feature of the input data is appropriately represented and scaled for subsequent computation. By transforming external signals into a format compatible with the network's internal architecture, the input layer initiates the overall computational workflow, setting the foundation for effective feature extraction, pattern recognition, and predictive modeling (Ammi et al., 2015). The dimensionality and structure of the input layer are directly determined by the number and type of input features, making it a critical component that influences both the efficiency and accuracy of the neural network's performance (Abdallah el hadj et al., 2017; Irfan et al., 2012; Lashkarbolooki et al., 2012; Petrović et al., 2011).

The input layer of a neural network comprises a set of artificial neurons responsible for receiving and transmitting data from the initial stages to the processing units of the system. This layer serves as the entry point and initiates the overall computational workflow of the neural network (Ammi et al., 2015).

*I.5.1.*2 Hidden Layer

The hidden layer of an artificial neural network functions as an intermediate processing stage situated between the input and output layers (Ammi et al., 2015). Each neuron within this layer receives input signals from the preceding layer, which are multiplied by adjustable weights that quantify the strength of the corresponding connections (Ammi et al., 2015; Si-Moussa et al.,

2008). These weighted inputs are then aggregated, and a nonlinear activation function is applied to determine the neuron's output (Abdallah el hadj et al., 2017; Korkerd et al., 2021; Laidi et al., 2013). This process enables the hidden layer to capture complex, nonlinear relationships within the input data, facilitating the extraction of meaningful patterns and feature representations that are not readily apparent from the raw inputs (Abdallah el hadj et al., 2017; Korkerd et al., 2021). The number of hidden layers, as well as the number of neurons within each layer, directly influences the network's capacity to model intricate dependencies, making the hidden layers a critical determinant of the overall learning ability and predictive accuracy of the artificial neural network.

The hidden layer of an artificial neural network operates between the input and output layers, with each artificial neuron's output determined by applying weighted connections to its respective inputs (Khaouane et al., 2012).

*I.5.1.*3 The Output Layer

The output layer represents the terminal layer of an artificial neural network, responsible for producing the network's specific outputs. Neurons in this layer, functioning as the network's final computational units, can be structured and treated distinctly from neurons in the preceding hidden layers (Khaouane et al., 2012).

I.5.2. Rationale for Using Neural Networks

Artificial neural networks (ANNs) possess a significant capacity to interpret complex, ambiguous, or incomplete data, enabling them to identify patterns and detect trends that may elude conventional computational methods or human observation. Once trained, a neural network can function as a domain-specific "expert," capable of making predictions based on novel inputs and addressing hypothetical scenarios. The advantages of neural networks include the following (Ammi et al., 2015, 2015; Hamadache et al., 2016; Khaouane et al., 2012; Melzi et al., 2019; Roubehie Fissa et al., 2019):

- ✓ **Adaptive Learning**: Artificial Neural Networks (ANNs) possess the capability to learn and adapt by analyzing training data or past experiences, enabling them to progressively improve their performance in executing specific tasks (Rezrazi et al., 2016). The training process involves adjusting connection weights and biases to minimize the error between predicted and actual values allowing it to capture underlying patterns, correlations, and nonlinear relationships within the data (Atsamnia et al., 2017b; Laxmi et al., 2011;

Rezrazi et al., 2016). This iterative learning mechanism endows ANNs with a form of adaptive intelligence, whereby their predictive accuracy and generalization ability increase over time as they are exposed to more representative datasets (Melzi et al., 2019; Si-Moussa et al., 2008). Consequently, ANNs are particularly well-suited for modeling complex, dynamic systems—such as fluidized beds—where traditional analytical or empirical methods may struggle to accurately represent the intricate interactions between multiple variables.

- ✓ **Self-Organization**: During the training phase, an ANN can autonomously structure and internalize the information it receives, facilitating efficient data representation.
- ✓ **Real-Time Processing**: Neural networks support parallel computation, allowing for rapid data processing. Dedicated hardware is being developed to exploit this parallelism effectively.
- ✓ **Fault Tolerance via Redundant Information Coding**: ANNs exhibit a degree of resilience to partial system failures. Even when components of the network are compromised, it can often continue to function, albeit with reduced performance.

I.5.3. Machine Learning

A neural network functions as a type of algorithm within the broader domain of machine learning. Prior to exploring neural networks in depth, it is essential to understand the foundational principles of machine learning itself. Machine learning is a sub-discipline of artificial intelligence that focuses on pattern recognition and data-driven modeling (Aleksić et al., 2015; Melzi et al., 2019). These algorithms are designed to process large volumes of data, and their performance is significantly influenced by the quality and nature of the training data provided. Once trained, a machine learning model is capable of generating predictions when exposed to new, similar input data (Khaouane et al., 2012). A neural network represents a specialized class of algorithms within the broader field of machine learning, and its effective application requires a clear understanding of the fundamental principles that underpin machine learning as a whole. Machine learning is a core sub-discipline of artificial intelligence concerned with the development of computational models capable of identifying patterns, extracting relationships, and generating insights directly from data. Rather than relying on explicit programming rules, machine learning techniques learn

from examples, enabling them to generalize from historical datasets to new and unseen scenarios (Karimi et al., 2018; Krzywanski et al., 2014).

Central to the success of any machine learning approach is the quality, diversity, and representativeness of the training data (Ammi et al., 2015). The performance, robustness, and predictive accuracy of a model are directly influenced by the statistical characteristics and variability of the data used during the learning phase. When appropriately trained, a machine learning model is capable of mapping complex input–output relationships and producing reliable predictions when presented with new, similar input data (Abdallah el hadj et al., 2017; Al-Eshmawy et al., 2024; Lashkarbolooki et al., 2012). This ability to infer underlying patterns and adapt to diverse operational conditions makes machine learning, and particularly neural networks, an invaluable tool in modeling nonlinear systems such as fluidized beds, where traditional analytical methods often fall short due to the highly complex and dynamic nature of gas–solid interactions (Ayoubi et al., 2011).

Machine learning tasks generally fall into two primary categories:

- ✓ **Regression**: This involves predicting continuous numerical values based on input variables.
- ✓ **Classification**: This refers to the assignment of input data to one of several predefined categories based on computational analysis (Ayoubi et al., 2011).

Figure I.8 depicts the two primary categories of machine learning.

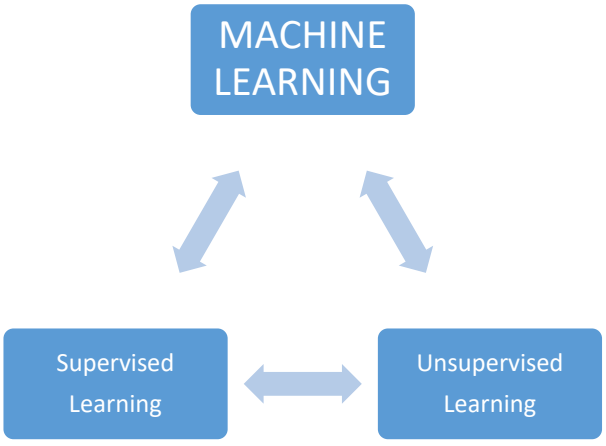


Figure I.8. Machine learning types (Ayoubi et al., 2011).

I.5.3.1. Supervised Learning

Supervised learning involves the use of labeled datasets, where the correct output is already known. The underlying assumption is that there exists a functional relationship between the input variables and the corresponding output. Supervised learning tasks can be broadly categorized into two types: *regression* and *classification*. In regression tasks, the objective is to predict outcomes with continuous values, effectively mapping input variables to a continuous function. In contrast, classification tasks involve predicting outcomes with discrete values, where the goal is to assign input data to predefined categories or classes (Lashkarbolooki et al., 2012).

I.5.3.2. Unsupervised Learning

Unsupervised learning, unlike its supervised counterpart, operates without labeled output data or corrective feedback. It seeks to uncover hidden patterns or structures within the data by analyzing the relationships between input variables. A common method within unsupervised learning is *clustering*, which involves grouping data based on similarity. However, the scope of unsupervised learning extends beyond clustering—for instance, it also encompasses models of *associative memory*, which relate to the system's ability to store and retrieve information without explicit supervision (Pezhhanfar et al., 2021).

I.5.4. Multilayer Perceptron (MLP)

Comprising three layers, the Multilayer Perceptron (MLP) network efficiently captures correlations between numerous input variables and corresponding output parameters. In this context, the inputs are designated as independent variables, and the outputs as dependent parameters (Pezhhanfar et al., 2021). The quantity of nodes in the input and output layers reflects the number of independent and dependent parameters, respectively. Situated between these layers, the hidden layer is fundamental to the network's architecture, with its size being specified by the user to optimize learning performance (Ammi et al., 2015; Atsamnia et al., 2017b). Within the network architecture, neurons in a given layer establish weighted connections and biases with neurons in the next layer, enabling the propagation and transformation of signals throughout the network (Pezhhanfar et al., 2021). Layers within the neural network facilitate information transfer both internally and externally, as in the case of the input layer. The neuron outputs can be expressed quantitatively through Equation (I.3).

$$z_t = f\left(\sum_{h=1}^{N} W_{th} X_h + b_t\right) \qquad (I.3)$$

X_h represents the input information, W_{th} is the weight coefficient emphasizing the input, and b_t is the bias term contributing to the output. The value of Z_t represents the output of the neurons after passing via the transfer function *f*.

Several types of transfer functions are available, including the hyperbolic tangent sigmoid, radial basis, and logarithmic sigmoid functions. In this study, the hyperbolic tangent sigmoid (TANSIG) activation function was employed due to its widespread use in neural networks. The TANSIG function is particularly advantageous because it maintains a non-zero derivative across its entire range, ensuring a smooth and balanced response. Moreover, it enables the modeling of nonlinear relationships, allowing the network to effectively learn complex interactions between input and output variables. These properties are mathematically described in Equation (I.4).

$$\mathrm{Tansig}(Z) = 2/(1 + \exp(-2Z)) - 1 \qquad \text{(I.4)}$$

In this equation, Z represents the input to the TANSIG function, producing the corresponding output value. By employing the TANSIG activation function, the MLP network introduces nonlinearity, enabling it to capture complex relationships between inputs and outputs and thereby enhancing its capability to model and predict the hydrodynamic parameters of interest.

I.6. The Role and Importance of MATLAB 2021 in this Study

In this study, MATLAB 2021 played a central and indispensable role in developing, training, and evaluating the artificial neural network model used for predicting the fundamental hydrodynamic parameters of fluidized beds. MATLAB is widely recognized as one of the most powerful computational environments for numerical analysis, data modeling, and machine-learning applications. Its integrated Neural Network Toolbox provides highly efficient algorithms for nonlinear regression, optimization, and performance assessment, making it particularly suitable for complex engineering systems such as fluidization processes (Atsamnia et al., 2017b; Khaouane et al., 2012; Ounnar et al., 2009; San José et al., 1998; Shaul et al., 2012). The ability of MATLAB to handle large datasets, automate training procedures, and generate comprehensive statistical indicators significantly enhanced the reliability and scientific rigor of the present work (Krzywanski et al., 2014; Lin et al., 2002; Matsusaka et al., 2013).

Through MATLAB 2021, an optimal multilayer perceptron (MLP) architecture was identified as a two-layer feedforward network consisting of fourteen hidden neurons. The software enabled the incorporation of physically meaningful input parameters—specifically, the dimensionless

numbers π_1 and π_2 derived from the Ergun equation, along with the hydraulic diameter used to distinguish between conical and cylindrical bed geometries. MATLAB then evaluated the predictive accuracy of the model using multiple performance metrics. The Average Absolute Relative Deviation (AARD) values of 6.11% for ΔP_{max} and 9.77% for U_{mf} demonstrated strong agreement between predicted and experimental measurements. Furthermore, MATLAB reported low Mean Squared Error (MSE) values (0.0146 for ΔP_{max} and 2.9×10^{-4} for U_{mf}) and correspondingly low RMSE values (0.120 and 0.0172), confirming the high precision of the model. The coefficient of determination (R^2) values of 0.935 and 0.989, together with correlation coefficients of 0.967 and 0.994 for ΔP_{max} and U_{mf} respectively, provided additional evidence of the robustness and predictive capability of the neural network (Fu et al., 2019; Tangier et al., 2012).

Overall, MATLAB 2021 not only facilitated the development of an accurate and stable prediction model but also ensured a rigorous quantitative assessment of its performance. Its advanced computational tools were essential in validating the proposed AI-based modeling approach and in demonstrating that the multilayer perceptron technique is both reliable and effective for forecasting key hydrodynamic behaviors in fluidized bed systems (Zardari, 2023).

I.7. The Role of STATISTICA 10 in this study

In addition to MATLAB 2021, the STATISTICA 10 software package was also employed in this study in an attempt to model and predict the hydrodynamic parameters of the fluidized bed system. STATISTICA 10 is a general-purpose statistical analysis platform widely used for data mining, multivariate analysis, regression studies, and classical statistical modeling (Ammi et al., 2015; Hamadache et al., 2016; Khaouane et al., 2012; Roubehie Fissa et al., 2019). It provides a user-friendly interface and a broad collection of analytical tools that make it suitable for exploratory data analysis and basic predictive modeling. Its neural network module, although functional, is primarily designed for standard regression and classification tasks and does not offer the same level of algorithmic flexibility, optimization capability, or customization as MATLAB's advanced machine-learning environment (Mića et al., 2015; Philippsen et al., 2015; Y. Zhou et al., 2020).

Despite its usefulness in statistical applications, the results obtained from STATISTICA 10 in this study were less accurate and less consistent than those generated by MATLAB

2021(Bousselma et al., 2021; Hamadache et al., 2016; Krzywanski et al., 2014; Lashkarbolooki et al., 2012; Maiti et al., 2018; Rezrazi et al., 2016). The software was unable to achieve the same level of prediction precision for ΔP_{max} and U_{mf}, and its performance indicators—such as error metrics and correlation values—were noticeably inferior. Moreover, STATISTICA 10 lacks the advanced training algorithms, parameter-tuning options, and optimization routines found in MATLAB's Neural Network Toolbox, which limited its ability to capture the nonlinear and highly coupled behavior characteristic of fluidization processes. For these reasons, and due to its comparatively weaker predictive performance, the results from STATISTICA 10 were not adopted in the final analysis, and MATLAB 2021 was selected as the primary and more reliable modeling tool for this research, for more information look APPENDIX B.

I.8. Conclusion

Fluidization finds widespread application in diverse industries and fields, ranging from chemical and petrochemical processes to pharmaceutical manufacturing, food processing, and environmental engineering. This process offers numerous benefits, including adequate mixing, enhanced heat and mass transfer, accelerated reaction rates, and the capability to handle challenging-to-fluidize materials. Moreover, *fluidized beds* play a crucial role in combustion processes like *fluidized bed boilers*

Artificial Neural Networks (ANNs), which form the foundation of deep learning methodologies, are computational models inspired by the structure and functioning of the human brain. Their architecture reflects the interconnectivity of biological neurons, enabling the simulation of complex information processing. ANNs consist of numerous interconnected simple processing units operating in parallel, allowing for efficient handling of complex tasks. This memoir has reviewed the fundamental principles of artificial neural networks, including the structure of a basic neuron and its computational counterpart. It has also explored the rationale for designing ANNs and presented an overview of the most commonly used network architectures. Furthermore, the review highlights notable developments in the classification of neural networks, emphasizing their relevance and growing importance in contemporary machine learning research.

Chapitre II. Critical Evaluation of the Solution Utilized in This Dissertation

Chapitre II. Critical Evaluation of the Solution Utilized in This Dissertation

II.1. Introduction

In this section, we present an overview of the working fluid utilized in this study, which consists primarily of a Newtonian liquid and suspended solid particles. The behavior and characteristics of this mixture play a crucial role in the performance and accuracy of the system under investigation. Newtonian fluids are characterized by a constant viscosity independent of the shear rate, making them predictable and well-suited for modeling and experimental validation. When solid particles are introduced into such fluids, the resulting suspension exhibits complex rheological properties that depend on particle concentration, size distribution, and fluid-particle interactions. Understanding these fundamental aspects is essential for analyzing flow dynamics, particle dispersion, and the overall effectiveness of the experimental setup (Liu et al., 2023).

Most substances with low molecular weight—including organic and inorganic liquids, aqueous solutions of inorganic salts, molten metals, and gases—generally exhibit Newtonian flow behavior. Under conditions of constant temperature and pressure, during simple shear, the shear stress (σ) is directly proportional to the shear rate ($\dot{\gamma}$), with the proportionality constant defined as the dynamic viscosity (η). Fluids exhibiting this behavior are traditionally referred to as Newtonian fluids, although the concepts of viscosity and fluid flow were recognized prior to Newton's formalization of the theory (Tanner et al., 1998). Typically, for liquids, viscosity decreases as temperature rises and increases under higher pressure, whereas for gases, viscosity tends to increase with both temperature and pressure. In general, the viscosity of a substance is directly related to its resistance to flow; thus, fluids with higher viscosity are more difficult to transport or pump (Reed et al., 1977). Representative viscosity values for a wide range of common fluids are provided in TableII.1 (Jaiswal et al., 1992). Moving down the table, viscosity increases by several orders of magnitude, leading to the perspective that a solid may be regarded as a limiting case of a fluid in which viscosity approaches infinity ($\eta \rightarrow \infty$). Consequently, the boundary between fluids and solids is less distinct than conventionally perceived. Since the establishment of the continuity and momentum equations by Cauchy and later formalized in the Navier–Stokes framework, the study of Newtonian fluid dynamics has advanced considerably over the past three centuries. Nevertheless, substantial challenges remain, particularly in the areas of turbulence and multiphase flow.

Table II.1. Values of viscosity for common fluids at room temperature (Jaiswal et al., 1992).

Substance	**η (Pa.s)**
Air	10^{-5}
Water	10^{-3}
Ethyl alcohol	1.2 10^{-3}
Mercury	1.5 10^{-3}
Ethylene glycol	20 10^{-3}
Olive oil	0.1
100% Glycerol	1.5
Honey	10
Corn syrup	100
Bitumen	10^{8}
Molten glass	10^{12}

Over the past five to six decades, it has become increasingly evident that numerous substances of industrial relevance—particularly multiphase systems such as foams, emulsions, dispersions, suspensions, and slurries, as well as polymeric melts and solutions of both natural and synthetic origin—deviate from the Newtonian assumption of a linear relationship between shear stress (σ) and shear rate ($\dot{\gamma}$) under simple shear conditions. Such materials are therefore classified as non-Newtonian, non-linear, complex, or rheologically complex fluids. TableII.2 presents representative examples of fluids exhibiting diverse types and varying degrees of non-Newtonian flow behavior (Rajendra P. Chhabra et al., 2001). The ubiquity of non-Newtonian characteristics in both natural and technological contexts suggests that Newtonian behavior is, in fact, the exception rather than the norm. This chapter provides a concise overview of the principal types of non-Newtonian flow behavior, methods of characterization, and their implications in engineering practice. The discussion draws primarily upon the authors' recent works (Raj P Chhabra et al., 2023), with the assumptions of material isotropy and incompressibility taken as implicit throughout.

TableII. 2. Examples of substances exhibiting non-Newtonian Fluid Behaviour (Rajendra P. Chhabra et al., 2001).

• Adhesives, such as wallpaper paste or carpet adhesive, are commonly used in various industrial and household applications.	• Food products, including fruit and vegetable purees and concentrates, sauces, salad dressings, mayonnaise, jams and marmalades, ice cream, soups, cake mixes and toppings, egg whites, bread mixes, and snack items, represent a diverse range of materials commonly studied in food processing and formulation research.
•Alcoholic beverages, including ales, beers, and liqueurs.	• Industrial greases and lubricating oils

• Liquid manure derived from cattle farms.	• Industrial mineral suspensions, including mine tailings
• Physiological fluids such as blood, synovial fluid, and saliva	• Lava and magma in their molten state
•Bitumen	• Finishing materials, such as paints, polishes, and varnishes
• Cementitious pastes and slurries	• Paper pulp suspensions
•Chalk slurries	• Polymer melts and solutions, reinforced plastics, rubber.
•Coal slurries	•Printing colors and inks
• Personal care and cosmetic products, such as nail polish, lotions, creams, lipsticks, shampoos, shaving products, and toothpaste.	• Pharmaceutical formulations, such as creams, foams, and liquid suspensions..
• Dairy materials and associated by-products, such as cheese, butter, yogurt, fresh cream, and whey.	•Sewage sludge
•Drilling muds	•Wet beach sand
•Fire fighting foams	•Waxy crude oils

II.2. Classification of Fluid Behavior

II.2.1. Overview of Newtonian Fluid Behavior

In a Newtonian fluid, shear stress varies linearly with shear rate, demonstrating that the fluid's viscosity is independent of the magnitude of applied shear. This foundational concept was originally formulated by Sir Isaac Newton in his seminal work *Philosophiae Naturalis Principia Mathematica* (1687), where he established the proportional dependency of shear stress on shear rate (Broniarz-Press et al., 2007; Liu et al., 2023). Newtonian fluids, due to their constant viscosity and linear relationship between shear stress and shear rate, are commonly encountered in both natural and industrial contexts. Typical examples include water, air, alcohols such as ethanol, gasoline, and light mineral oils. In addition, many dilute aqueous solutions—such as those containing dissolved sugars or salts—also exhibit Newtonian behavior under standard conditions. These fluids are widely employed in engineering applications because their flow characteristics are straightforward to model and predict, making them ideal for use in systems where accurate control and simulation of fluid motion are essential (Broniarz-Press et al., 2007; Kawase et al., 1985; Machač et al., 1997; Vaferi, Rahnama, et al., 2013).

It is instructive to commence with a formal definition of a Newtonian fluid. Under conditions of simple shear (Figure II. 1), The rheological behavior of a Newtonian fluid is defined by a linear proportionality between applied shear stress and the resulting shear rate, which is mathematically expressed as:

$$\sigma_{yx} = \frac{F}{A} = \dot{\eta}\gamma_{yx} \qquad \text{(II.1)}$$

FigureII.2 presents experimental data for corn syrup and cooking oil, both of which demonstrate Newtonian fluid behavior. The corresponding flow curves intersect the origin, with viscosity values of η = 11.6 Pa·s for corn syrup and η = 64 mPa·s for cooking oil. FigureII.1 and equation (1) illustrate the simplest case, in which only one velocity component, V_x, varies as a function of (y). In contrast, for the general case of three-dimensional flow (FigureII.3), the stress tensor (**S**) comprises six shear components and three normal components. Conventionally, the total stress is decomposed into an isotropic component (pressure) and a deviatoric component, expressed as (Jaiswal et al., 1992):

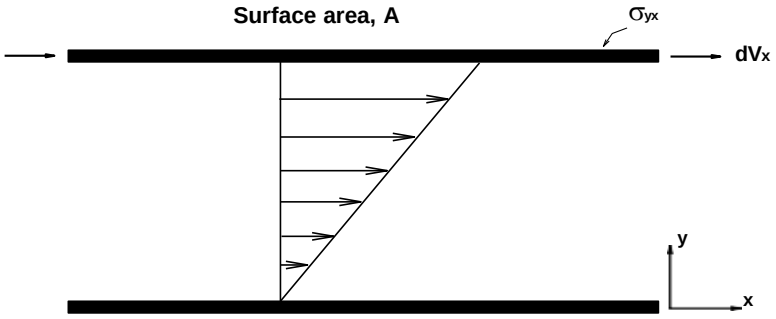


Figure II.1. Schematic representation of a unidirectional shear flow (Jaiswal et al., 1992).

$$s = -p\mathrm{I} + \sigma \qquad \text{(II.2)}$$

Where σ is traceless, i.e., $tr \cdot \sigma = 0$, and pressure is consistent with the continuity equation. The tracefree requirement together with the physical requirement of symmetry $\sigma = \sigma^{T}$ imply that there are only three independent shear components (off-diagonal elements) and two normal stress differences (diagonal elements) of the deviatoric stress. Thus, in Cartesian coordinates, these are $\sigma_{xy}(= \sigma_{yx})$, $\sigma_{xz}(= \sigma_{zx})$, $\sigma_{yz}(= \sigma_{zy})$and the two normal stress differences defined as;

Primary normal stress difference, $N_{1=\sigma_{xx}-\sigma_{yy}}$ (II.3)

Secondary normal stress difference, $N_{2=\sigma_{zz}-\sigma_{yy}}$ (II.4)

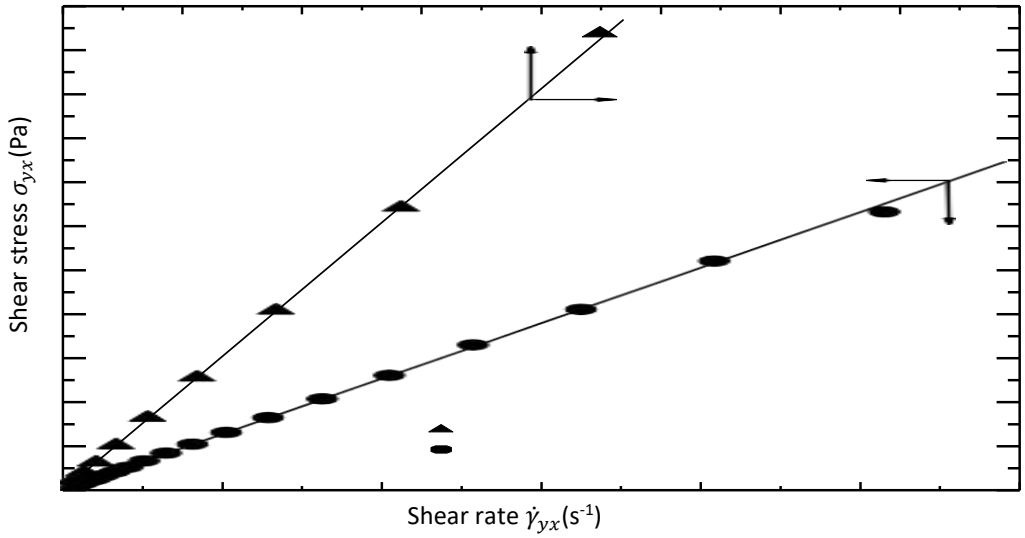


Figure.II.2. illustrates representative shear stress–shear rate relationships for two Newtonian fluids (Jaiswal et al., 1992).

In the case of Newtonian fluids, the stress components exhibit a linear relationship with the components of the rate-of-deformation tensor, governed by the scalar viscosity. As an illustration, the three stress components acting on the x-plane (with its normal oriented along the x-axis) in FigureII.3 can be expressed as follows.

$$\sigma_{xx} = -2\eta \frac{\partial V_x}{\partial_x} \qquad \text{(II.5)}$$

$$\sigma_{xy} = -\eta \left(\frac{\partial V_x}{\partial_y} + \frac{\partial V_y}{\partial_x}\right) \qquad \text{(II.6)}$$

$$\sigma_{xz} = -\eta \left(\frac{\partial V_x}{\partial_z} + \frac{\partial V_z}{\partial_x}\right) \qquad \text{(II.7)}$$

Analogous equations can be formulated for the stress components associated with the y- and z-planes. In the case of a Newtonian fluid subjected to simple shear, the normal stresses vanish ($\sigma_{xx} = \sigma_{yy} = \sigma_{zz} = 0$), as the velocity component V_x varies solely in the y-direction. Consequently, a comprehensive definition of a Newtonian fluid necessitates conformity with the full Navier–Stokes equations, rather than being limited to the assumption of a constant shear viscosity.

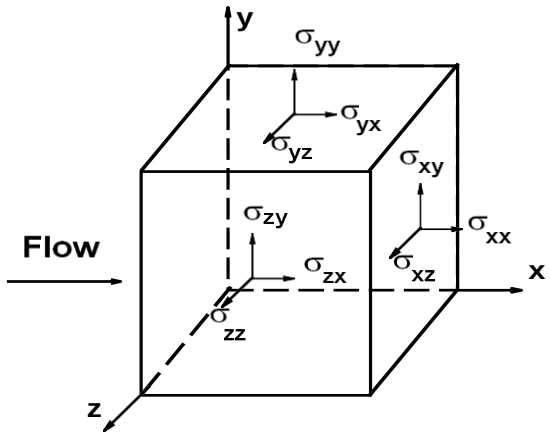


Figure II. 3. Stress components in three dimensional flow (KIM, 2019).

II.2.2. Key Properties of Newtonian Fluids

Newtonian fluids exhibit a set of well-defined rheological characteristics that distinguish them from non-Newtonian counterparts. The most significant properties are outlined below:

- **Constant Viscosity**: The dynamic viscosity remains constant regardless of the applied shear rate or duration of shear. This implies that the fluid's resistance to deformation does not vary with flow conditions (KIM, 2019).
- **Linear Stress–Strain Relationship**: Newtonian fluids strictly follow **Newton's law of viscosity**, where shear stress is directly proportional to the shear rate(Vaferi, Karimi, et al., 2013).
- **Absence of Yield Stress**: Newtonian fluids begin to flow under the slightest applied stress. There is no threshold stress value (yield stress) required to initiate flow(Rajendra P. Chhabra et al., 2001).
- **Time-Independent Behavior**: These fluids do not exhibit **time-dependent viscosity effects** such as *thixotropy* (decrease in viscosity over time under shear) or *rheopexy* (increase in viscosity over time under shear) (Dilmi et al., 2023).

II.2.3. Applications

Newtonian fluids play a fundamental role across a wide range of scientific and engineering disciplines due to their predictable flow characteristics. In **chemical engineering**, they are crucial in the design of pipeline systems and chemical reactors, where accurate flow modeling is essential for efficiency and safety (Ali Reza et al., 2010). **Mechanical engineering** applications

include lubrication systems and hydraulic circuits, where the stability of viscosity simplifies performance calculations. In the **biomedical field**, blood is often approximated as a Newtonian fluid under high shear rate conditions, such as in large arteries, to facilitate simplified hemodynamic modeling. **Computational Fluid Dynamics (CFD)** simulations frequently assume Newtonian behavior as a baseline condition to reduce computational complexity while maintaining acceptable accuracy in many scenarios. Additionally, in the **pharmaceutical industry**, Newtonian fluids such as aqueous solutions are used as carriers in drug delivery systems, benefiting from their consistent rheological properties for controlled administration (Abd-Rabbo et al., 2020; Ali Reza et al., 2010; Davarpanah et al., 2021; Islam et al., 2021; Mehdizad et al., 2018).

II.2.4. Non-Newtonian Fluids

II.2.4.1. Rheological Characteristics of Non-Newtonian Fluids

The most fundamental departure from Newtonian fluid behavior arises when the simple shear stress–shear rate (σ–$\dot{\gamma}$) relationship neither passes through the origin nor remains linear. In such cases, the apparent viscosity, defined as $\sigma/\dot{\gamma}$, is not constant but varies as a function of either σ or $\dot{\gamma}$. Moreover, under certain conditions, the apparent viscosity of specific materials depends not only on the prevailing flow parameters (e.g., geometry, shear rate) but also on the kinematic history of the fluid element. For practical purposes, albeit through a somewhat arbitrary classification, non-Newtonian fluids are commonly grouped into three categories:

1. Purely viscous or generalized Newtonian fluids (GNFs): In these systems, the shear rate at a point within the fluid is determined solely by the instantaneous value of shear stress at that point. These fluids are also referred to as inelastic or time-independent fluids.

2. Time-dependent fluids: In this case, the σ–$\dot{\gamma}$ relationship additionally depends on the duration of shearing and the prior deformation history. Such fluids exhibit phenomena such as thixotropy or rheopexy (Depypere et al., 2005).

3. Viscoelastic fluids: These materials combine viscous flow behavior with elastic, solid-like characteristics, displaying effects such as partial elastic recovery, recoil, and creep.

Although this classification is convenient, it remains somewhat simplistic, as many real materials simultaneously exhibit characteristics from multiple categories. For example, polymer

melts may display both time-independent shear-thinning behavior and viscoelasticity, whereas china clay suspensions can demonstrate a combination of shear-thinning or shear-thickening with time-dependent (thixotropic) responses at certain concentrations or shear rates. Nevertheless, it is generally feasible to identify the dominant non-Newtonian characteristic in a given system and employ it as the basis for process modeling and analysis. The following sections will examine each category of non-Newtonian behavior in greater detail (Mehdizad et al., 2018).

II.2.4.2. Time-Independent Rheological Behavior

As previously noted, within the context of simple unidirectional shear, this subclass of fluids is distinguished by the characteristic that the instantaneous shear rate at a given point is determined exclusively by the corresponding instantaneous shear stress, and vice versa (KIM, 2019; Mathur et al., 1955). In other words, such fluids exhibit no dependence on their deformation history and therefore possess no memory of past flow conditions. Consequently, their steady-shear behavior can be represented by a constitutive relation of the general form :

$$\dot{\gamma}_{yx} = f(\sigma_{yx}) \qquad \text{(II.8)}$$

Or, its inverse form

$$\dot{\gamma}_{yx} = f^{-1}(\dot{\gamma}_{yx}) \qquad \text{(II.9)}$$

Depending upon the form of equation (II.8) or (II.9), three possibilities exist:

1. Shear-thinning (pseudoplastic) behavior
2. Viscoplastic behavior, with or without shear-thinning characteristics
3. Shear-thickening (dilatant) behavior

FigureII.4 provides a qualitative representation of the flow curves (rheograms) for these three categories of fluid behavior, plotted on linear coordinates. For comparison, the linear relationship characteristic of Newtonian fluids is also included in the figure.

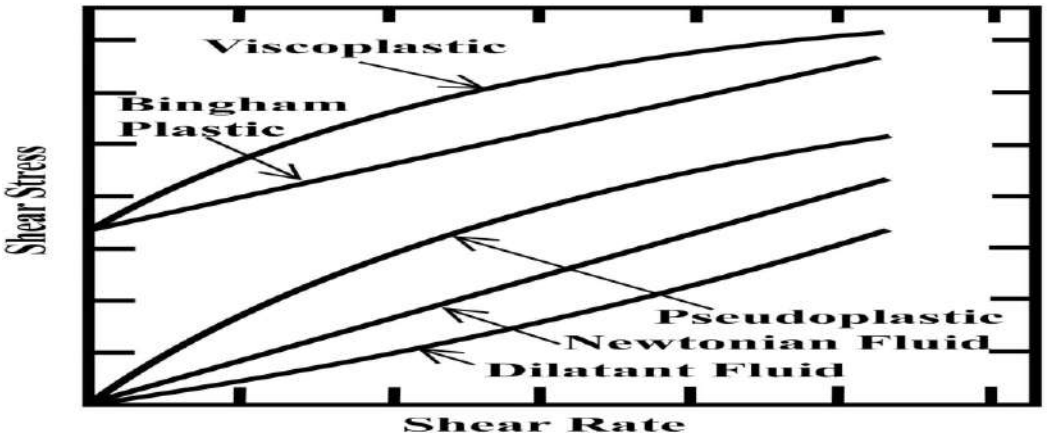


Figure II .4 Qualitative flow curves of non-Newtonian fluids (KIM, 2019; Mathur et al., 1955).

II.2.4.3 Time-Dependent Rheological Behavior

A wide range of materials, particularly those encountered in the food, pharmaceutical, and personal care product industries, exhibit flow characteristics that cannot be adequately represented by simple mathematical models such as equations (8) or (9). This limitation arises because their apparent viscosities depend not only on Material response is a function of applied shear stress (σ), shear rate ($\dot{\gamma}$), shear duration, and prior kinematic history. For example, the manner in which a sample is introduced into the testing device can significantly influence its measured rheological response (Rajendra P. Chhabra et al., 2001).

The method used to introduce a sample into a viscometer—whether by pouring, syringe injection, or alternative approaches—can substantially affect the measured shear stress (σ) and shear rate ($\dot{\gamma}$). Likewise, when materials such as bentonite-in-water suspensions, coal slurries, red mud slurries (a byproduct of the alumina industry), cement pastes, waxy crude oils, and cosmetic formulations (e.g., lotions and creams) are subjected to a constant shear rate following an extended rest period, their apparent viscosities generally decrease. This decrease results from the gradual disruption of internal structural networks within the material (Roubehie Fissa et al., 2019). As the number of breakable linkages diminishes, the rate of viscosity change approaches zero. Conversely, while structures break down, the potential for reformation of linkages increases, eventually leading to a dynamic equilibrium where the rates of breakdown and rebuilding are balanced. In contrast, certain systems reported in the literature exhibit the opposite trend: external shear promotes the formation of internal structures, leading to an increase in apparent viscosity with continued shearing. On this basis, time-dependent fluid behavior is

conventionally classified into two categories: **thixotropy**, in which viscosity decreases with shear duration, and **rheopexy** (or negative thixotropy), in which viscosity increases with shear duration (Bar, Biswas, et al., 2010; R P Chhabra, n.d.).

II.2.4.4 Visco-elastic behavior

For an ideal elastic solid, the stress developed under shear is directly proportional to the strain. In the case of uniaxial tension, this relationship is expressed by Hooke's law, where the proportionality constant is the elastic modulus, commonly denoted as the Young's modulus,(G) (Lin et al., 2002):

$$\sigma_{yx} = -G\frac{\partial x}{\partial y} = G(\gamma_{yx}) \qquad \text{(II.10)}$$

An ideal elastic solid subjected to elastic deformation completely recovers its original shape upon removal of the applied stress. However, if the applied stress exceeds the material's characteristic yield stress, full recovery does not occur, and creep is observed, indicating that the solid experiences irreversible deformation (Machač et al., 1997). Table II.3 presents representative values of the Young's modulus (G) for various classes of materials, including metals, plastics, polymers, colloidal solutions, and food products. These values serve as a useful reference for classifying certain materials as "soft solids." At the opposite end of the spectrum, a Newtonian fluid exhibits a linear relationship between shear stress and shear rate, as described by the following equation (II.1). Many engineering materials, however, exhibit both elastic and viscous responses under suitable conditions. In the absence of thixotropic or rheopectic effects, materials are described as viscoelastic. Perfectly viscous flow and perfectly elastic deformation therefore represent the two limiting cases of viscoelastic behavior. In some substances, only these extremes are observed in practice; for example, the viscosity of ice or the elasticity of water is generally negligible under ordinary conditions (Maiti et al., 2018).

It should be emphasized that the mechanical behavior of a material is governed not only by its intrinsic structure but also by the specific kinematic conditions to which it is subjected. As a result, the distinction between solids and fluids, as well as between elastic and viscous responses, is often somewhat arbitrary and not always clearly defined. Indeed, a single material may exhibit characteristics of both states depending on the prevailing conditions (Petrović et al., 2011).

Here's your sentence polished into a more academic style:

exhibit fluid-like viscous behavior under certain conditions and solid-like elastic behavior under

others

TableII.3. Representative (approximate) values of Young's modulus (Malkin et al., 2022; Steffe, 1996)

Material	Value of *G*
Glass	70 GPa
Aluminium, Copper and alloys	100 GPa
Steel	200 GPa
High modulus oriented fibers	>300 GPa
Concrete	10-20 GPa
Stones	40-60 GPa
Wood	1-10 GPa
Ice	10 GPa
Engineering Plastics	5-20 GPa
Leather	1-100 MPa
Rubber	0.1-5 MPa
Polymer and colloidal solutions	1-100 MPa
Dry spaghetti	3 GPa
Carrots	20-40 MPa
Pears	10-30 MPa
Potatoes	6-14 MPa
Peach	2-20 MPa
Raw apples	6-14 MPa
Gelatin Gel	0.2 MPa
Banana	0.8-3 MPa

A wide range of practically significant materials—including polymer melts and solutions, soap solutions, gels, synovial fluids, emulsions, and foams—exhibit viscoelastic behavior. Such substances possess the capacity to both store and recover shear energy (W. Bai et al., 2021; Raza et al., 2021). An important consequence of this rheological characteristic is the development of stresses, known as *normal stresses*, in the direction perpendicular to the applied shear. In simple shear flow, these normal stresses manifest as the first and second normal stress differences ((N_1) and (N_2)), as defined in equations II.3a and II.3b, and are typically proportional to the shear rate (Raza et al., 2021).

FiguresII.5 and FiguresII.6 present representative experimental data for the first and second normal stress differences in polystyrene–toluene solutions at 298 K. It is also customary to define the first (primary) and second (secondary) normal stress difference coefficients, denoted as Ψ_1 and Ψ_2, respectively, as follows (Brea et al., 1976; Warren Lee McCabe et al., 1993; Yates,

1988):

$$\Psi_1 = \frac{N_1}{(\dot{\gamma})^2} \qquad \text{(II.11a)}$$

$$\Psi_2 = \frac{N_2}{(\dot{\gamma})^2} \qquad \text{(II.11b)}$$

Although the specific rates of variation of N_1 and N_2 with shear rate differ from one system to another, several general trends can be identified. In most cases, the rate of decrease of Ψ_1 with increasing shear rate is greater than that observed for the apparent viscosity (Kulicke et al., 1985).

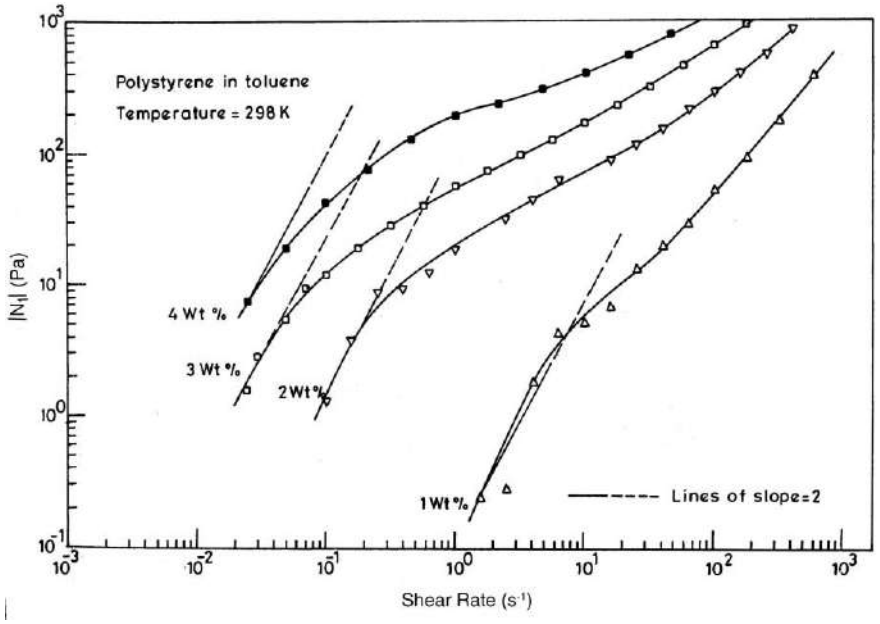


Figure II. 5. Typical first normal stress difference data for Polystyrene in toluene solutions (Kulicke et al., 1985).

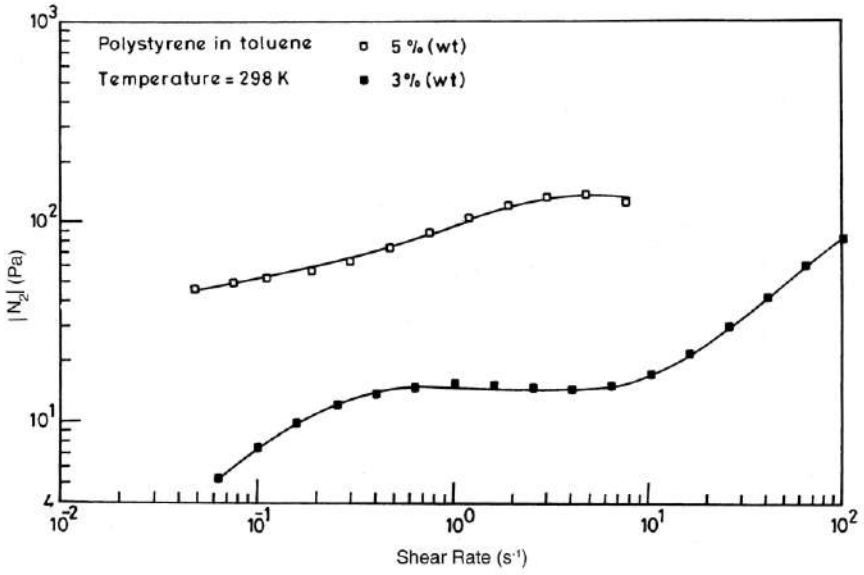


Figure II. 6. Typical second normal stress difference data for polystyrene in toluene solutions(Kulicke et al., 1985).

At very low shear rates, (N_1) is expected to vary proportionally to $((\dot{\gamma})^2)$, such that (Ψ_1) approaches a constant value in this limit, as confirmed by some of the experimental data presented in FigureII. 14. The ratio (N_1/σ) is frequently used as an indicator of the degree of viscoelasticity (Kulicke et al., 1985). More specifically, (N_2/σ), referred to as the recoverable shear, is a widely employed measure; values exceeding 0.5 are not uncommon in highly viscoelastic polymeric systems (Rajendra P. Chhabra et al., 2001).

In practice, The experimental determination of the first normal stress difference (N_1) is substantially more challenging than measuring the shear stress (σ). Measurement of the second normal stress difference (N_2) is even more difficult. Typically, N_2 is negative and of considerably smaller magnitude, generally around 10% of N_1. Until the mid-1970s, it was commonly assumed that $N_2 = 0$; however, subsequent studies have shown this assumption to be inaccurate (Brea et al., 1976).

Accordingly, in simple shear, a viscoelastic material is characterized by the functions $N_1(\dot{\gamma})$, $N_2(\dot{\gamma})$, and $\sigma(\dot{\gamma})$. On this basis, normal stress differences are frequently used to distinguish between inelastic fluids, for which ($N_1 \ll \sigma$) and viscoelastic fluids, for which ($N_1 \gg \sigma$) (Al-Eshmawy et al., 2024)(Rajendra P. Chhabra et al., 2001)

Thus far, the discussion has been confined to simple unidirectional shear flow (Gernon et al., 2012). The analysis now extends to two additional model flow configurations: oscillatory shear

flow, which provides a practical means of characterizing linear viscoelastic behavior, and elongational flow, which serves as an idealized representation of many industrially important processes (Agu et al., 2019; Brea et al., 1976; Ergun, 1952b; Philippsen et al., 2015).

II.3. Conclusion

This chapter has provided a comprehensive examination of the rheological behavior of the working fluid employed in this dissertation, encompassing both Newtonian and non-Newtonian characteristics. The discussion began with a detailed analysis of Newtonian fluids, which are governed by a linear stress–strain relationship and constant viscosity, enabling precise modeling through the Navier–Stokes framework. Their predictable flow behavior underpins numerous engineering and scientific applications, from hydrodynamic systems to biomedical and pharmaceutical processes.

In contrast, the chapter emphasized that many real-world materials deviate from Newtonian behavior, displaying non-linear or time-dependent rheological responses. Non-Newtonian fluids—including pseudoplastic, viscoplastic, dilatant, thixotropic, and viscoelastic types—demonstrate complex dependencies on shear rate, stress history, and deformation time. Among these, viscoelastic materials occupy a particularly important position, as they exhibit both fluid-like viscous and solid-like elastic properties, characterized by measurable normal stress differences.

Through this critical evaluation, it becomes evident that while Newtonian models provide the foundation for understanding fluid motion, the inclusion of non-Newtonian and viscoelastic effects is essential for accurately describing multiphase systems, suspensions, and polymeric materials. This understanding forms the theoretical basis for the experimental and analytical investigations presented in the subsequent chapters of this dissertation.

Chapter III.

Materials and Methods

Chapter III. Materials and Methods

III.1. Introduction

The flowing gas is uniformly distributed within a cylindrical gas-solid bed due to its uniform cross-sectional area, as pointed out by (Levenspiel, 1998) and (Kunii et al., 1991). From a different perspective, conical beds provide a longer contact path for gas-solid interactions, thereby influencing gas-solid reactions and mass transfer processes (Davidson et al., 1964). Conical beds also enhance gas distribution at the U_{mf} (Yates, 1988). In contrast, cylindrical beds are preferred for better mixing of solid particles due to their axial symmetry, which is particularly beneficial in processes like coating (Kunii et al., 1991)(1981; Wong, 2002) A discussion regarding the widely used correlations for predicting the minimum fluidization velocity of small solid particles. Moreover, cylindrical beds offer a larger and more efficient surface area for thermal transfer, contributing to drying and combustion processes (Warren L McCabe et al., 2005), and improved particle discharge, minimizing particle accumulation and bed clogging (Kunii et al., 1991). The tapered shape of conical beds facilitates upward particle movement, thereby aiding chemical reactions and granulation processes (Gernon et al., 2012). Additionally, this geometric shape enables easier and more controlled discharge of fine particles.

Several empirical correlations and theoretical models have been created to predict the U_{mf} under different operating conditions for various particle types. These models vary in their accuracy (Bahramian, 2021; Jaiswal et al., 1992; Shabanian et al., 2012). The previous models can be classified into two primary categories. Firstly, there are modifications of Ergun's equation (Ergun, 1952b, 1952a), such as the one proposed by (Wen et al., 1966). Secondly, there are numerous models that rely on the analysis of operating parameters to estimate the changes in U_{mf} as (Fu et al., 2019). Additionally, (Rasteh et al., 2015), (Khani, 2011), and (Fang et al., 2020) they all developed a dimensional analysis model to predict ΔP_{max} and U_{mf}. Therefore, there exist various correlations, some of which are presented in **Table III.1.**

Table III. 2. Obtainable correlations used for calculation of ΔP_{max} and U_{mf} in fluidized column.

Correlation for U_{mf}	Condition	Ref.
$Re_{mf} = (33.7^2 + 0.0408A_r)^{0.5} - 33.7$	–	(Wen et al., 1966)
$F_r = 0.2714\ (A_r)^{0.3197}(\sin)^{0.6092}(\frac{\varepsilon_0}{\emptyset_s})^{0.6108}$	–	(Sau et al., 2007)
$Re_{mf} = 7.16(A_r)^{0.393}\left(\frac{d_p}{D_0}\right)^{0.98}\left(\frac{\varepsilon_0}{\emptyset_s}\right)^{-0.833}(\cos\alpha)^{-275.486}$	*For 0 ≤α≤4.5°*	(Khani, 2011)
$Re_{mf} = 10.396(A_r)^{0.367}\left(\frac{d_p}{D_0}\right)^{0.889}\left(\frac{\varepsilon_0}{\emptyset_s}\right)^{-0.7.31}(\cos\alpha)^{-10.43}$	*For ºα>4.5*	
$Re_{mf} = 0.203(A_r)^{0.588}\left(\frac{\varepsilon_0}{\emptyset_s}\right)^{2.69}\left(\frac{H_0}{D_0}\right)^{0.276}(\cos\alpha)^{-6.42}$	*For Bo <0.05*	(Rasteh et al., 2015)
$Re_{mf} = 0.253(A_r)^{0.6368}(B_0)^{-0.0933}\left(\frac{\varepsilon_0}{\emptyset_s}\right)^{1.44}\left(\frac{H_0}{D_0}\right)^{0.278}(\cos\alpha)^{-6.47}$	*For Bo ≥0.05*	
$Re_{mf} = [(33.7^2 + 0.0408A_r)^{0.5} - 33.7]/[1 - \exp(-14.45\Delta P^{-0.3})]$	–	(Fu et al., 2019)
$U_{mf} = \frac{\sum_{i-1}^{n}(x_i {d_i}^{0.55})^{\left(\frac{2}{0.55(\rho_s-\rho_g)g}\right)}}{1653\mu_g}$	–	(Shao et al., 2020)
Correlation for ΔP_{max}		
$\Delta P_{max} = 7.457\left(\frac{D_1}{D_0}\right)^{0.038}\left(\frac{d_P}{D_0}\right)^{0.222}\left(\frac{H_s}{D_0}\right)^{0.642}\left(\frac{\rho_s}{\rho_g}\right)^{0.723}$	*Condition*	(Sau et al., 2007)
$\frac{\Delta P_{max}}{\rho_s g H_s} = 106.729\left(\frac{\rho_s}{\rho_g}\right)^{-0.522}\left(\frac{d_P}{D_0}\right)^{0.309}\left(\frac{H_0}{D_0}\right)^{-0.379}(\cos\alpha)^{-10.858}$	–	
$\frac{\Delta P_{max}}{\rho_s g H_s} = 163.419\left(\frac{\rho_s}{\rho_g}\right)^{-0.524}\left(\frac{d_P}{D_0}\right)^{0.269}\left(\frac{H_0}{D_0}\right)^{-0.976}(\cos\alpha)^{-3.277}$	*For 0 ≤α≤4.5° For ºα>4.5*	(Khani, 2011)
$EU_{mf} = 3.69 * 10^6(A_r)^{-0.547}\left(\frac{\varepsilon_0}{\emptyset_s}\right)^{-0.848}\left(\frac{H_0}{D_0}\right)^{-0.299}(\cos\alpha)^{6.33}$	*For Bo <0.05*	(Rasteh et al., 2015)
$EU_{mf} = 1.098 * 10^7(A_r)^{-0.626}(B_0)^{0.035}\left(\frac{\varepsilon_0}{\emptyset_s}\right)^{-0.914}\left(\frac{H_0}{D_0}\right)^{-0.319}(\cos\alpha)^{6.84}$	*For Bo ≥0.05*	

Over the past decade, artificial neural networks (ANNs) have become widely recognized and extensively utilized, thanks to their strong parallel processing capabilities, robustness, and their inherent capacity to derive highly non-linear and complex relationships between problem variables directly from experimental data, without requiring detailed prior knowledge of the system (Ammi et al., 2015)(Kamari et al., 2020; Marahel et al., 2022). Artificial neural networks employ a combination of weights and hidden neurons to represent intricate connections, making them proficient in managing input that is either abundant or imprecise (Anbazhagan et al., 2020).

This chapter contains three main parts:

- **Introduction and Theoretical Background**: It introduces the concept of artificial neural networks (ANNs) and their suitability for modeling complex fluidization systems.
- **Experimental Equations and Data Preparation**: It presents the development of dimensionless equations (π_1, π_2, and A_r) for predicting minimum fluidization velocity and pressure drop, along with a description of the collected experimental dataset.
- **Model Training and Evaluation**: It explains the process of training the Multilayer Perceptron (MLP) neural network using the Levenberg-Marquardt algorithm, including data splitting for training, validation, and testing phases.

III.2. Experimental Equations for Minimum Fluidization Velocity

Two dimensionless numbers were derived from the Ergun equation. The first, π_1, represents a dimensionless coefficient characterizing energy dissipation due to fluid friction within the fluidized bed. This parameter exhibits a positive correlation with the fluid velocity (U) in the Ergun equation and shares similar characteristics with the dimensionless viscous number, as shown in Equation III.1. The second dimensionless number, π_2, characterizes kinetic energy dissipation within the bed and is directly proportional to the square of the fluid velocity (U^2) in the Ergun equation, resembling the dimensionless inertial number, as shown in Equation III.2. Together with the Archimedes number, these dimensionless parameters serve as reliable independent variables for predicting the maximum pressure drop (ΔP_{max}) and the minimum fluidization velocity (U_{mf}). Additionally, the hydraulic diameter was incorporated to account for differences between cylindrical and conical beds, as represented in Equation III.3. The proposed model explicitly considers viscous energy dissipation, which arises from fluid viscosity, and

kinetic energy dissipation, resulting from particle motion. The study aims to investigate the influence of fluid and solid properties on fluidization behavior, while highlighting the role of hydraulic diameter. Consequently, the model provides improved predictions across a broad range of system geometries and dimensions.

$$\pi_1 = \left(\left(\frac{\mu_g}{\mu_e}\right)\left(1-\frac{\varepsilon}{\emptyset}\right)^2\right)/\left(\left(\frac{d_p H_0}{d_H^2}\right)^2\left(\frac{\varepsilon}{\emptyset}\right)^3\right) \qquad \text{(III.1)}$$

$$\pi_2 = \left(\left(\frac{\rho_g}{\rho_e}\right)\left(1-\frac{\varepsilon}{\emptyset}\right)\right)/\left(\left(\frac{d_p H_0}{d_H^2}\right)\left(\frac{\varepsilon}{\emptyset}\right)^3\right) \qquad \text{(III.2)}$$

$$d_H = \frac{4\left(r_0^2+r_1^2+r_0 r_1\right)*(cos(\alpha/2))}{3\left(r_0+r_1\right)} \qquad \text{(III.3)}$$

III.3. Artificial neural Networks(ANNs)

As a non-parametric computational methodology, neural networks acquire knowledge of the underlying data structure by iteratively adjusting internal parameters during the learning process (Kamari et al., 2020; Marahel et al., 2022). Artificial neural networks leverage hidden neurons in conjunction with weighted connections to model complex interdependencies, thereby providing robust performance in handling both high-volume and noisy input data (Anbazhagan et al., 2020). Neural networks are well-suited for a variety of applications, including regression, classification, time series analysis, and segmentation. Input data is typically scaled linearly to the interval (0,1) to ensure numerical stability and proper network performance. Neural networks can be broadly categorized into two types: multi-layer networks and radial basis networks. Predictive capabilities may be realized through either a single network or an ensemble of networks, depending on the complexity of the task and the desired accuracy (Rama Sastry, 2022). The multi-layer perceptron (MLP), featuring a non-linear feed-forward neural network (FFNN) architecture, is widely recognized as a leading regression model across numerous scientific and engineering disciplines (Hamadache et al., 2016; Melzi et al., 2019; Rama Sastry, 2022).

Numerous studies have employed feedforward neural networks (FFNN) to predict the minimum fluidization velocity (U_{mf}). For instance, Fu et al. (Fu et al., 2019), A feedforward neural network (FFNN) was applied to predict the minimum fluidization velocity (U_{mf}) in binary particle mixtures. The study demonstrated that the network produced highly accurate and reliable predictions. Collectively, these results indicate that FFNNs are a promising tool for forecasting

U_{mf} in fluidized bed reactors. Nevertheless, the precision of such predictions depends critically on both the quality and the quantity of training data used to develop the network.

III.3.1. Multilayer Perceptron (MLP)

The Multilayer Perceptron (MLP) network consists of three layers, allowing it to effectively model relationships between numerous input variables and output parameters. In this context, the input variables are referred to as independent variables, while the output parameters are considered dependent variables (Pezhhanfar et al., 2021). The number of nodes in the input and output layers corresponds to the number of independent and dependent variables, respectively. A hidden layer, positioned between the input and output layers, plays a critical role in the network architecture. The number of nodes within the hidden layer is typically determined by the user based on the complexity of the problem (Ammi et al., 2015; Atsamnia et al., 2017b). Neurons within each layer form connections to neurons in the subsequent layer via weighted links and associated biases (Pezhhanfar et al., 2021). The layers communicate information either internally or with external layers, as exemplified by the input layer. The output of each neuron can be expressed numerically using Equation III.4.

$$z_t = f(\sum_{h=1}^{N} W_{th}X_h + b_t) \qquad \text{(III.4)}$$

X_h denotes the input information, W_{th} represents the weight coefficient assigned to the input, and b_t is the bias term contributing to the neuron's output. The variable Z_t corresponds to the neuron's output after processing through the transfer function f. A variety of transfer functions are available, including the hyperbolic tangent sigmoid, radial basis, and logarithmic sigmoid functions. In this study, the hyperbolic tangent sigmoid (TANSIG) activation function was employed due to its widespread use in neural networks. The TANSIG function was chosen for its non-zero derivative across the entire input range, which ensures a balanced response. Moreover, it facilitates the modeling of non-linear interactions and effectively captures complex relationships between input and output variables. These properties are mathematically represented by Equation III.5.

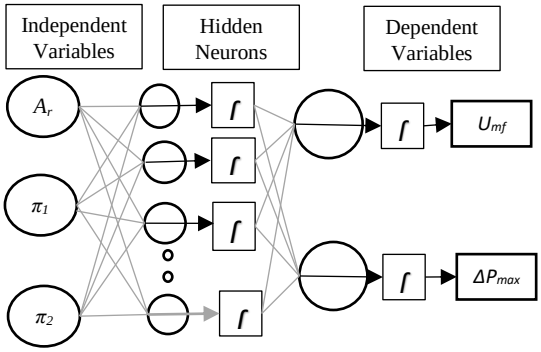
$$\text{Tansig}(Z) = 2/(1 + \exp(-2Z)) - 1 \qquad \text{(III.5)}$$

In this equation, Z represents the input to the TANSIG function, producing the corresponding output value. The application of the TANSIG activation function allows the MLP network to introduce non-linearity, thereby capturing complex relationships between input and output variables. This capability enhances the network's effectiveness in modeling and predicting the hydrodynamic parameters of interest.

III.4. Modelling procedure

III.4.1. Database collection

The initial step in designing and developing a Multilayer Perceptron (MLP) involves identifying the key independent variables that affect the dependent parameters (Benimam et al., 2020; Roubehie Fissa et al., 2019). A thorough review of existing literature has established that the hydrodynamics of a fluidization system are influenced by multiple factors. These include properties of the solid particles, such as diameter, density, and shape, as well as characteristics of the fluidizing gas, including viscosity and density. Additional engineering parameters of the bed—such as inlet diameter, porosity, and hydraulic diameter—also significantly affect fluidization behavior. To facilitate analysis, these variables were expressed in dimensionless form. The dimensionless parameter π_1 corresponds to viscous energy dissipation, characterizing the distribution of dynamic viscosity relative to liquid properties, particle geometry, and the hydraulic diameter of the bed. The Archimedes number (Ar) reflects the selection of fluids and solid particles within the system. Moreover, the dimensionless parameter π_2 represents kinetic energy dissipation and the distribution of density with respect to fluid properties and the hydraulic diameter. The maximum pressure drop (ΔP_{max}) and the minimum fluidization velocity (U_{mf}) were evaluated as functions of Ar, π_1, and π_2, as illustrated in Figure III.1 and Table III.2.



FigureIII. 1: The structure of the model presented in the prediction process.

TableIII. 2. The structure of the model presented in the prediction process

	DB for NN
Input	$A_r = d_p^3 \, g \, \rho_g \, (\rho_s - \rho_g)/\mu_g^2$ $\pi_1 = \left(\frac{\mu_g}{\mu_e}\right)\left(1 - \frac{\varepsilon}{\emptyset}\right)^2 \Big/ \left(\frac{d_p H_l}{d_H^2}\right)^2 \left(\frac{\varepsilon}{\emptyset}\right)^3$ $\pi_2 = \left(\frac{\rho_g}{\rho_e}\right)(1 - \frac{\varepsilon}{\emptyset}) \Big/ (\frac{d_p H_l}{d_H^2})\,(\frac{\varepsilon}{\emptyset})^3$
Output	U_{mf} , Δp_{max}

In this study, we employed a database called "DB," which was acquired from existing literature sources (Karimi et al., 2018; Korkerd et al., 2021). The database (DB) comprises 327 empirical data points characterizing fluidization behavior in both conical and cylindrical beds, with 192 observations pertaining to conical beds and 135 to cylindrical beds. A subset of this database was employed to predict the maximum pressure drop (ΔP_{max}) and the minimum fluidization velocity (U_{mf}). Particle sizes were selected according to Geldart's classification, focusing on representative sizes from the B and D groups. For additional details, refer to Appendix A in the Supporting Information section.

III.4.2. Training

Figure III.2 illustrates the sequential procedure followed in developing the model. The study utilized the percentage difference between experimentally measured values and computed parameters as the evaluation metric. During the training phase, the primary objective was to minimize discrepancies between predicted and observed values by adjusting the weights and biases of the Multilayer Perceptron (MLP). The Levenberg-Marquardt algorithm was employed to optimize network training. (Marquardt, 1963),as it has been shown to demonstrate superior performance in previous studies (Ariana et al., 2015; Farizhandi et al., 2016; Karimi et al., 2018; Vaferi et al., 2014). The complete experimental dataset was randomly divided into three subsets. Seventy percent of the data (229 instances) was used for model training, while 15% (49 instances) was reserved for validation. The remaining 15% (49 instances) served as a test set to evaluate the performance of the trained network.

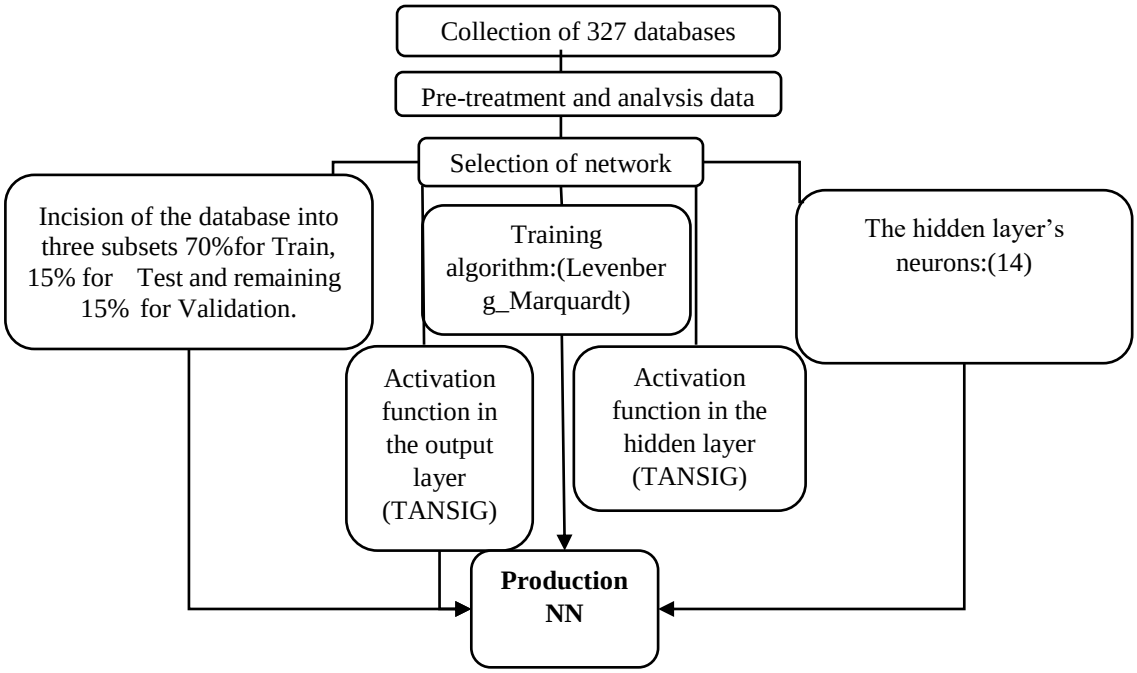


Figure III.2: The architectural design of the model proposed.

III.5. conclusion

This chapter detailed the methodological framework adopted for predicting key fluidization parameters (U_{mf} and ΔP_{max}) using artificial neural networks. It began with an overview of the theoretical background of ANNs and their relevance in modeling complex fluidization systems. Next, it introduced the development of dimensionless experimental equations derived from the Ergun equation to capture the influence of fluid and particle properties on system behavior. Furthermore, the chapter described the structure and functioning of the Multilayer Perceptron (MLP) neural network, emphasizing data collection, preprocessing, and the training process using the Levenberg-Marquardt algorithm. The use of a comprehensive experimental database, along with appropriate data partitioning for training, validation, and testing, ensures the reliability and accuracy of the developed model. This methodological approach sets the foundation for the results and analysis presented in the subsequent chapter.

Chapter IV

Results and discussion

Chapter **IV.** Results and discussion

IV .1. Introduction

In this chapter, the results obtained are discussed and organized into four parts:

- ✓ In the initial section, the influence of the independent variables on the dependent variables will be examined, as this step is essential for validating the modeling process (Al-Eshmawy et al., 2024; Bousselma et al., 2021; Irfan et al., 2012; Maiti et al., 2018; Melzi et al., 2019; Petrović et al., 2011).
- ✓ The topology of a Multi-Layer Perceptron (MLP) defines its overall architectural structure, including the number and arrangement of layers (input, hidden, and output layers), the quantity of neurons within each layer, and the connectivity scheme between neurons (Bar, Biswas, et al., 2010; Korkerd et al., 2021; Laxmi et al., 2011). This topology plays a fundamental role in determining the learning capacity and generalization performance of the neural network model (Bar, Bandyopadhyay, et al., 2010; Roubehie Fissa et al., 2019).
- ✓ Model checking is a powerful formal verification technique that systematically analyzes finite-state models of systems to determine whether they satisfy specified behavioral properties, often formulated in temporal logic. Its ability to provide counterexamples upon property violations makes it an essential tool in the development of safety-critical software and hardware systems (KIM, 2019).
- ✓ In the fourth section, the neural network was employed to validate the reinforcement relationship between the identified independent variables and their corresponding outcomes (Abdallah el hadj et al., 2017; Ayoubi et al., 2011; Lashkarbolooki et al., 2012). The analysis focused on examining the deviations observed between the independent variables and the predicted values of ΔP_{max} and U_{mf}.

IV.2. Examination of the Correlation Matrix

In quantitative modeling, evaluating the relationships between predictor (independent) variables and response (dependent) variables is a crucial step to ensure the reliability, robustness, and interpretability of the resulting model (Li et al., 2023). One of the most commonly employed statistical tools for this purpose is the correlation matrix, which offers a structured overview of

the linear relationships among variables. The matrix comprises correlation coefficients—typically expressed as Pearson's r—which quantify both the strength and direction of these linear associations (Roubehie Fissa et al., 2019). Correlation coefficients range from −1 to +1. Values approaching +1 indicate a strong positive linear relationship, meaning that as one variable increases, the other also increases consistently. Conversely, coefficients near −1 signify a strong negative linear relationship, in which the variables move in opposite directions. Values close to 0 suggest the absence of a linear relationship, although non-linear associations may still exist and should be investigated further (Felipe et al., 2007; Korkerd et al., 2021; Tahmasebpoor et al., 2015). Importantly, the correlation matrix can help identify potential issues such as multicollinearity, which occurs when two or more independent variables are highly correlated. Multicollinearity can compromise the predictive performance of a model by inflating variance and reducing the stability of parameter estimates.

Within the framework of artificial neural network modeling—particularly multilayer perceptron (MLP) architectures—correlation analysis provides valuable insights into the interdependence of variables and helps identify the most influential input features. This analysis is often complemented by a sensitivity study, which quantifies the extent to which variations in each input affect the model outputs. Table IV.1 presents both correlation coefficients and sensitivity measures, offering a comprehensive overview of the contributions of each independent variable to the prediction of dependent hydrodynamic parameters in the system under study (Abdallah el hadj et al., 2017; KIM, 2019; Rasteh et al., 2018).

Assessing the influence of independent variables on dependent variables is essential for validating the modeling process. A correlation matrix provides a tabular representation of correlation coefficients among variables, typically ranging from −1 to +1. A coefficient approaching +1 indicates a strong positive association, while a coefficient nearing −1 signifies a strong negative relationship. Additionally, a correlation coefficient of zero implies the absence of a linear relationship, although non-linear relationships may still exist (Aleksić et al., 2014). Table IV.1 presents the correlation coefficients that depict the relationships between independent variables and dependent parameters, along with a comprehensive assessment of the sensitivity of the MLP model.

Table IV 1. The linear relationship's values. And the sensitivity analysis in Samples: Train, Test, Validation.

Dependent variables	**Independent variables**		
	A_r	**π_1**	**π_2**
U_{mf}	0.8763	-0.2965	-0.2476
ΔP_{max}	0.0512	-0.5680	-0.6239
MLP 3-14-2 (Sensitivity analysis)	15.423	19.389	9.389

A_r has been recognized as having the highest linear dependence with U_{mf} because it influences various parameters such as viscosity and solid particle diameter. Likewise, π_1 and π_2 show the highest linear dependence with ΔP_{max}, where (H_0/d_H^2) shows the change in bed stock associated with the decrease in bed pressure. In addition, it is observed that U_{mf} displays an increase with higher bed stock (Korkerd et al., 2021). The correlation coefficients indicate that none of the independent variables have a zero value, supporting our assumption.

IV.3. MLP Topology

The architecture of the MLP neural network is primarily defined by the number of hidden layers and the number of neurons within each layer. In the context of gas–solid fluidization, as noted by (Laxmi et al., 2011). The results indicate that a multilayer perceptron (MLP) network with a single hidden layer can accurately predict the ΔP_{max} and U_{mf} parameters, achieving a precision exceeding 95%. Furthermore, selecting an appropriate number of neurons in the hidden layer is critical to attaining a satisfactory level of predictive accuracy within an acceptable margin of error. (Bar, Biswas, et al., 2010). The predictive performance of the MLP network can be evaluated using various statistical metrics, including the correlation coefficient (R), root mean square error (RMSE), mean square error (MSE), and absolute average relative deviation (AARD) (Abdallah el hadj et al., 2017; Karimi et al., 2018; Korkerd et al., 2021; Lashkarbolooki et al., 2012). Additionally, the coefficient of determination, commonly denoted as R^2, is a statistical metric used to quantify the proportion of the total variation in the dependent variable that is explained by the model (Karimi et al., 2018; Marahel et al., 2022; Melzi et al., 2019). The MLP network can be configured with the minimum number of neurons required to achieve sufficient predictive accuracy by identifying the optimal number of hidden neurons. Figures IV.1(a,3b,5,c,7,d,9,e) and IV.2(a,4,b,6,c,8,d,10,e) illustrate the data points corresponding to

AARD, RMSE, MSE, R, and R^2 metrics for multiple MLP networks used to predict ΔP_{max} and U_{mf}. These networks varied in the number of hidden neurons, and predictive accuracy improved progressively as the hidden layer size increased. Maximum accuracy was observed with fourteen neurons in the hidden layer, with negligible improvement when increasing to fifteen neurons. To mitigate bias and the effects of weight initialization on results, the MLP network was trained multiple times using the entire dataset.

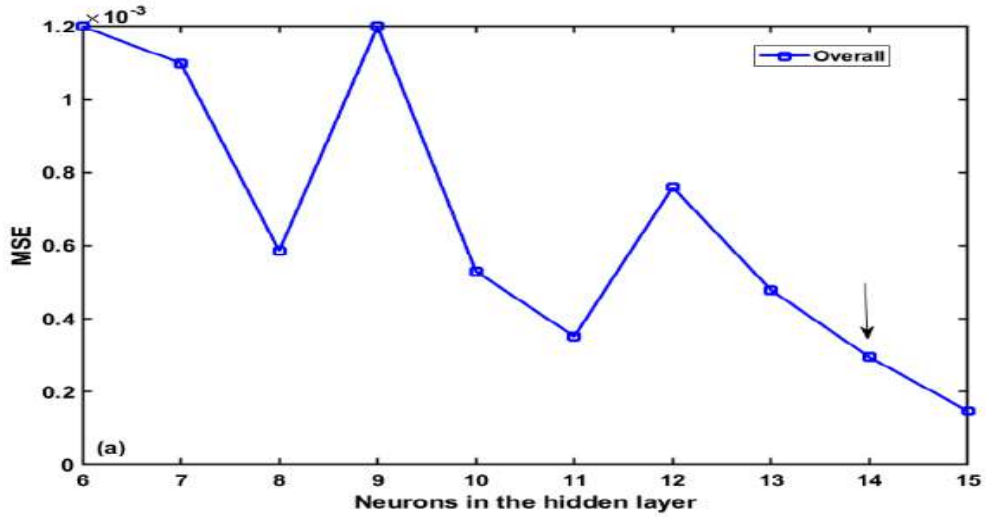


Figure IV. 1.a: Related overall MSE of different MLP topologies in prediction experimental data of the U_{mf}.

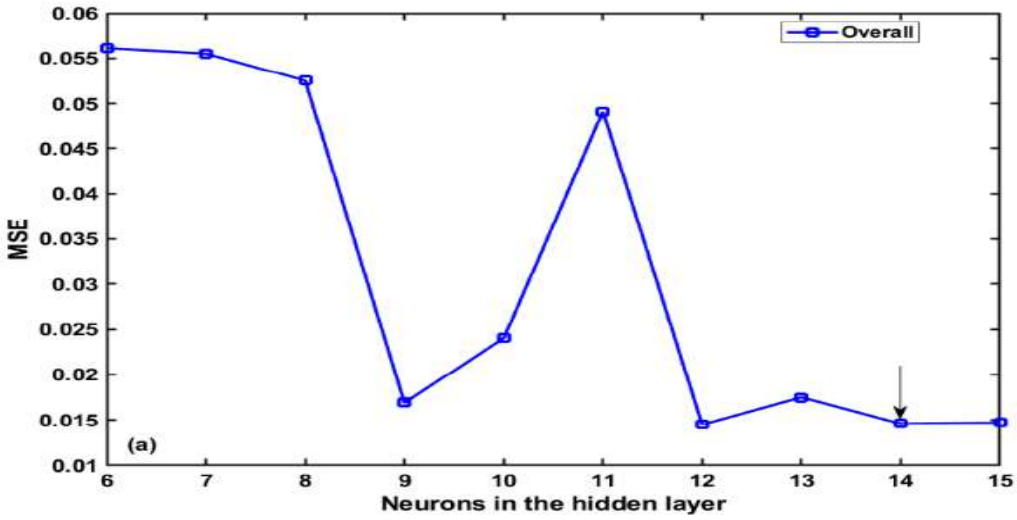


Figure IV. 2.a: Related overall (a) MSE of different MLP topologies in prediction experimental data of the ΔP_{max}.

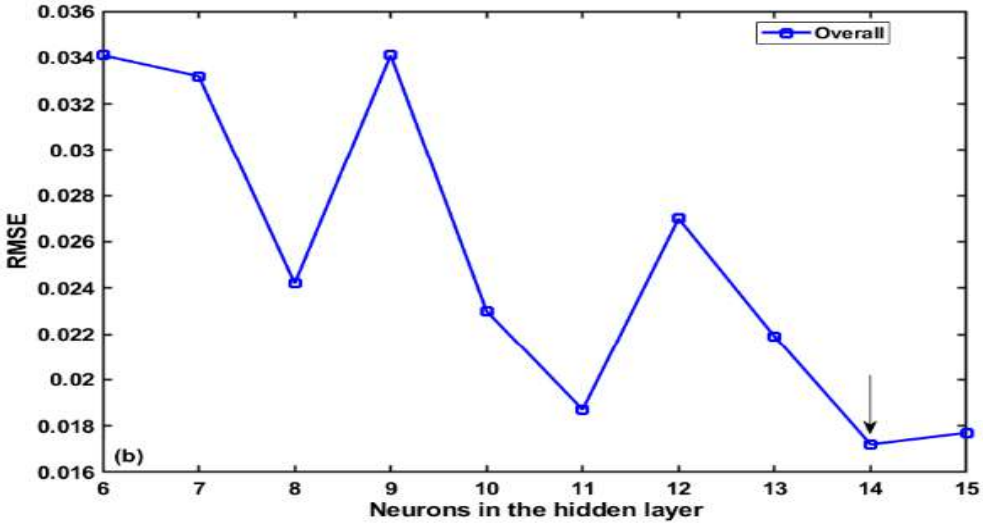


Figure IV. 3.b: Related overall RMSE of different MLP topologies in prediction experimental data of the U_{mf}.

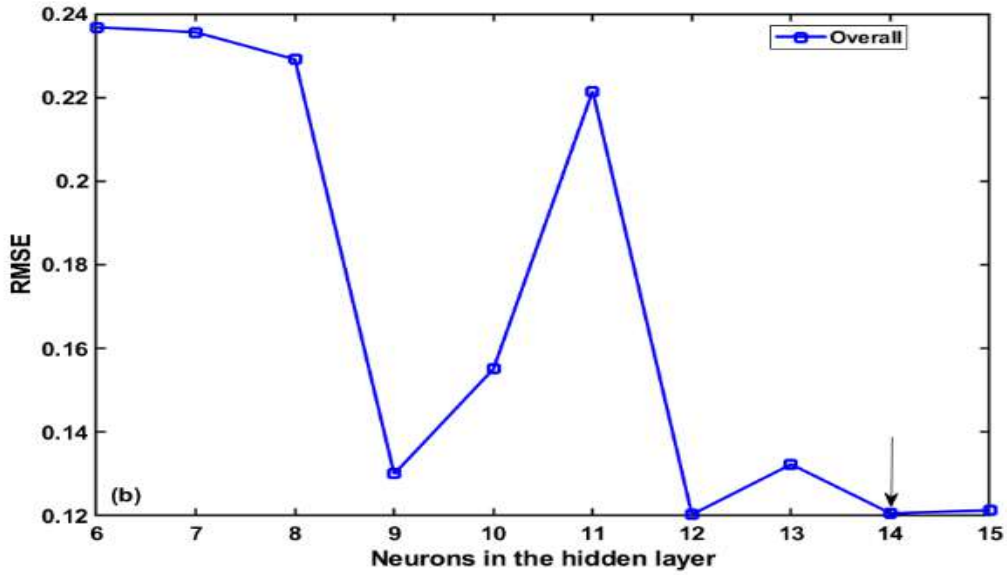


Figure IV. 4.b: Related overall RMSE of different MLP topologies in prediction experimental data of the ΔP_{max}.

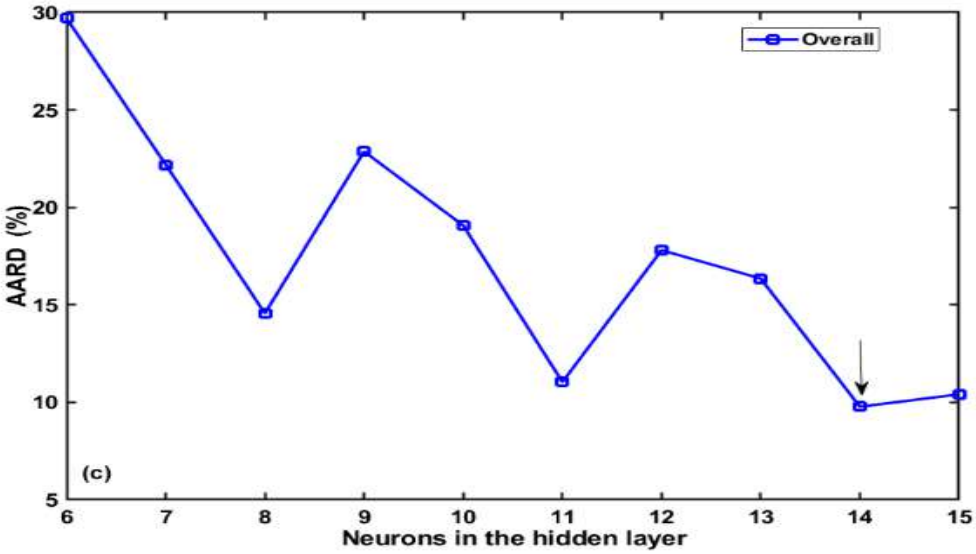


Figure IV. 5.c: Related overall AARD of different MLP topologies in prediction experimental data of the U_{mf}.

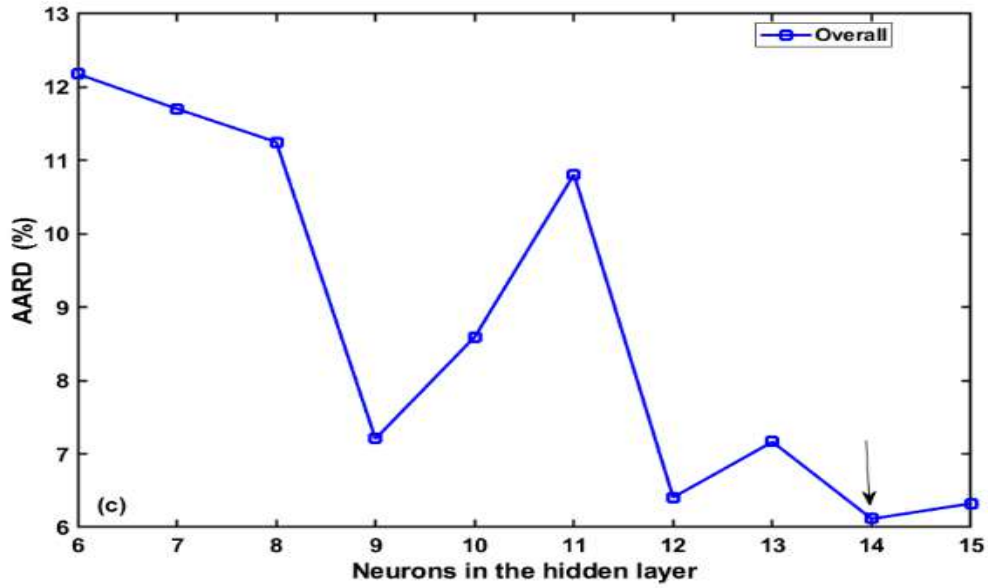


Figure IV. 6.c: Related overall AARD of different MLP topologies in prediction experimental data of the ΔP_{max}.

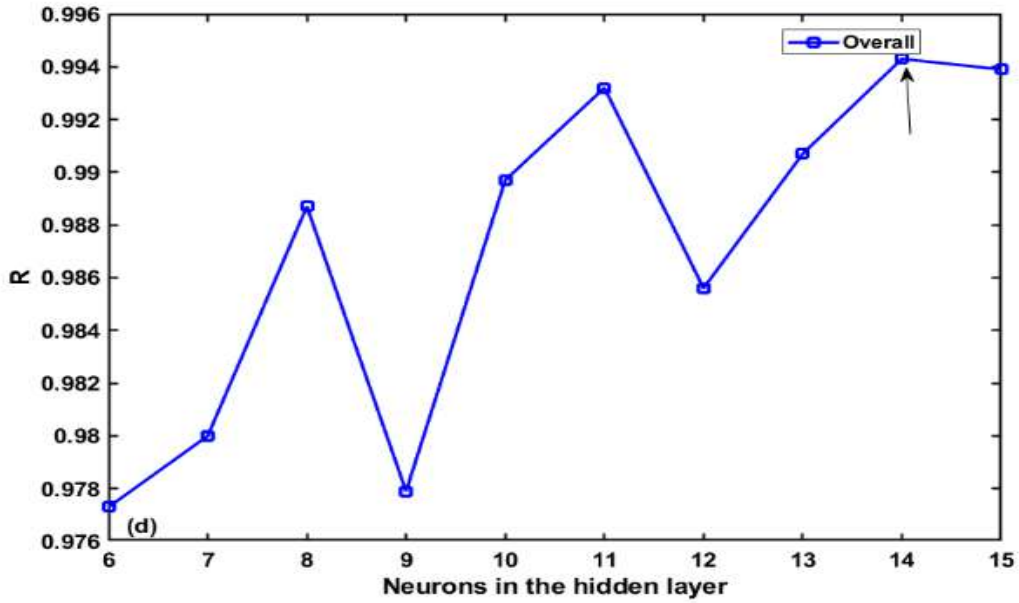


Figure IV. 7.d: Related overall R of different MLP topologies in prediction experimental data of the U_{mf}.

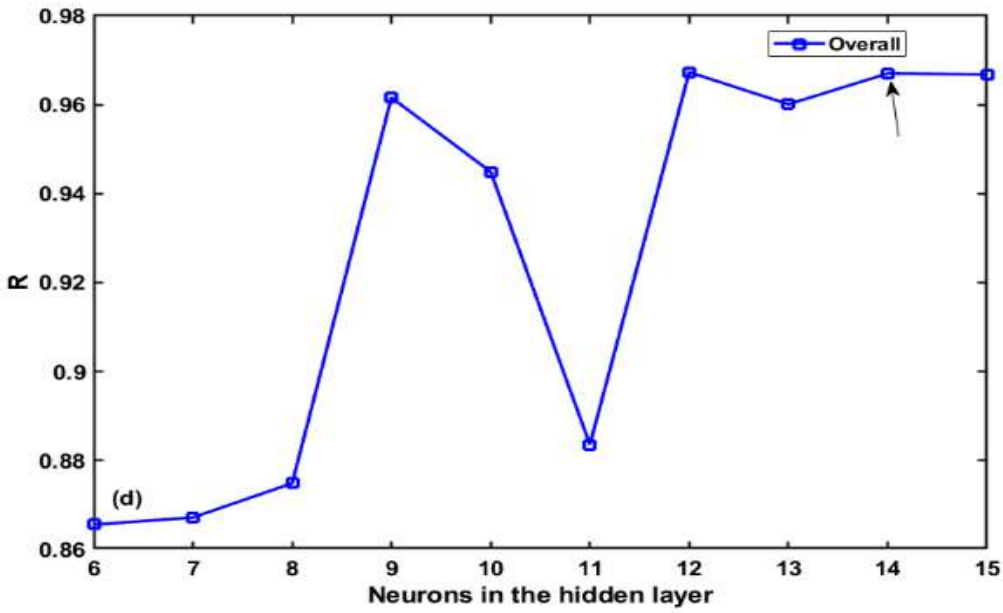


Figure IV. 8.d: Related overall R of different MLP topologies in prediction experimental data of the ΔP_{max}.

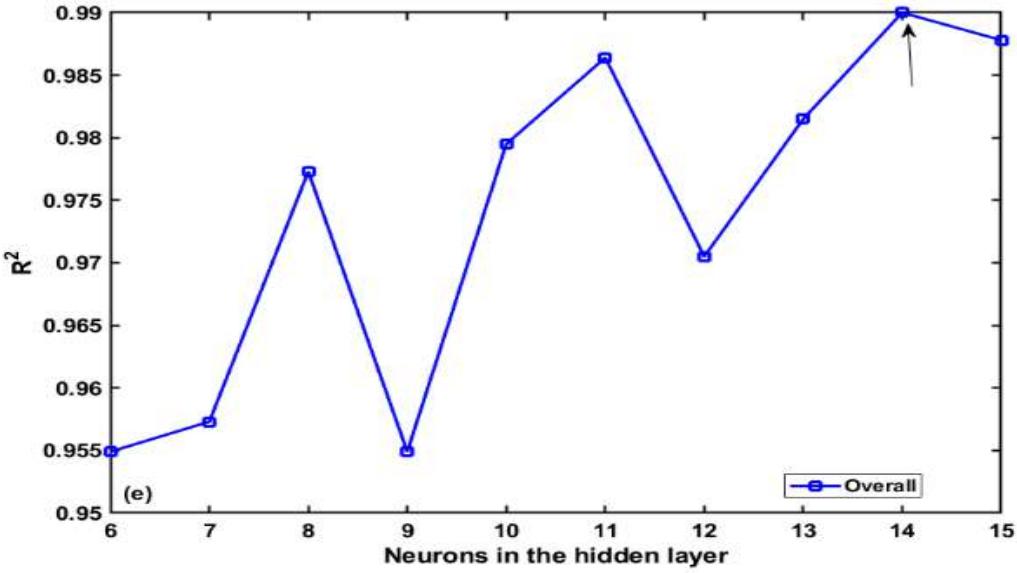


Figure IV. 9.e: Related overall R^2 of different MLP topologies in prediction experimental data of the U_{mf}.

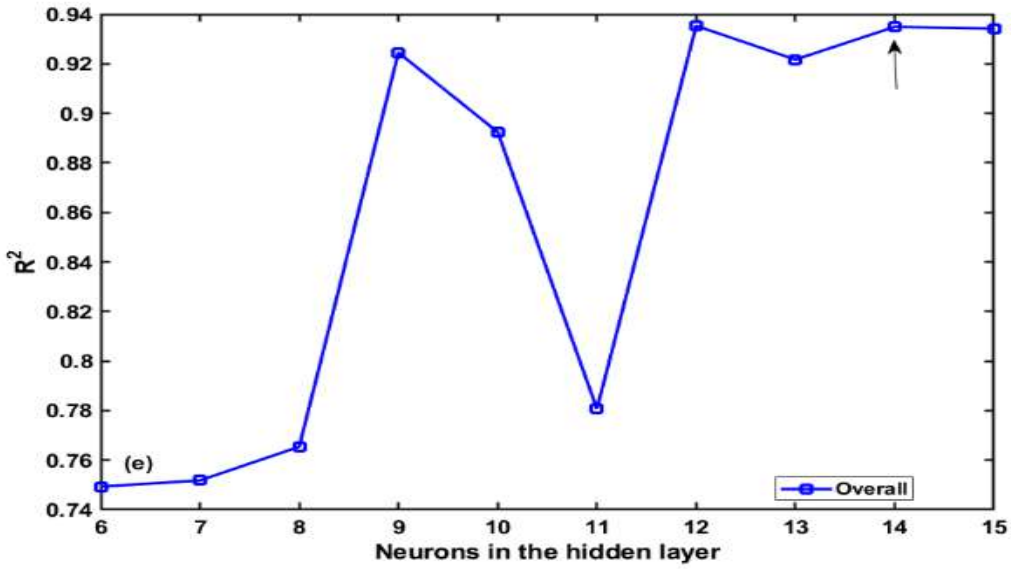


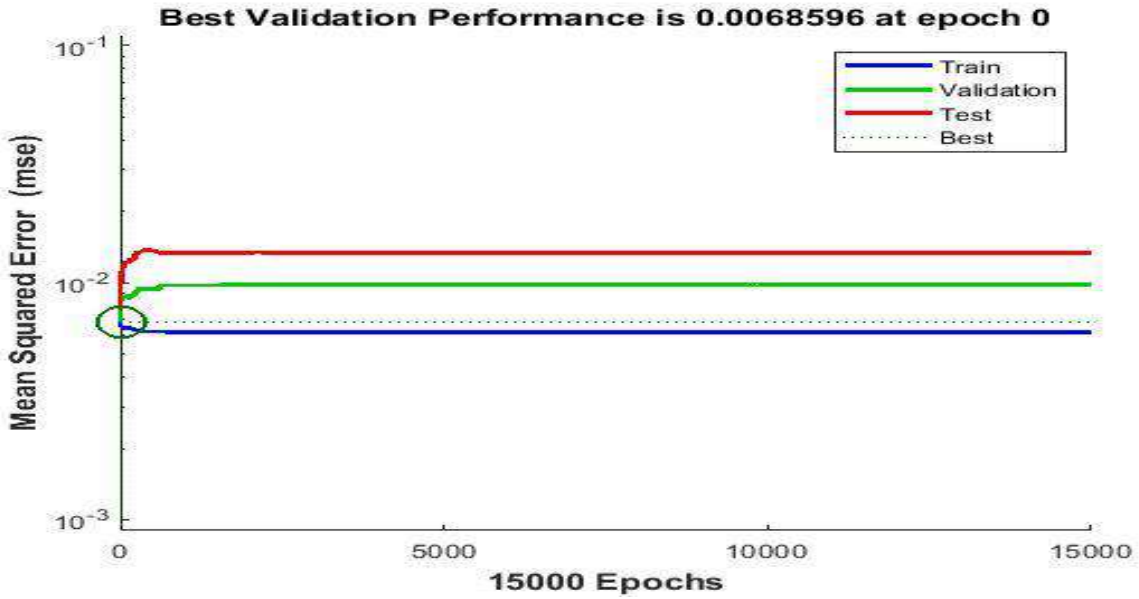
Figure IV. 10.e: Related overall R^2 of different MLP topologies in prediction experimental data of the ΔP_{max}.

Table IV.2 presents the optimal results, highlighting the most favorable MLP network configuration. The aggregated performance metrics were as follows: AARD values of 6.11% and 9.77%, MSE values of 0.0146 and 2.9×10^{-4}, RMSE values of 0.120 and 0.0172, R^2 values of 0.935 and 0.989, and correlation coefficients (R) of 0.967 and 0.994 for ΔP_{max} and U_{mf}, respectively. A comprehensive analysis of statistical errors indicated that the optimal MLP architecture is a two-layer feed-forward network with fourteen hidden neurons. This conclusion was reinforced through consolidation of data from previous studies to ensure accuracy and reliability. The results provide empirical evidence demonstrating the effectiveness of the developed MLP model in accurately predicting ΔP_{max} and U_{mf} under the studied conditions. Notably, the optimal network architecture comprises three neurons in the input layer, fourteen neurons in the hidden layer, and two neurons in the output layer. The predictive performance of the MLP network was further evaluated using validation data, as illustrated in the validation performance plots. Figure IV.6 depicts the variation of Mean Squared Error (MSE) with respect to the number of training epochs.

Table IV. 2. The statistically sound analysis.

Hidden neuron	**Statistical index**	U_{mf} *(m/s)*	ΔP_{max} *(Kpa)*
6	MSE	0.0012	0.0561
	RMSE	0.0341	0.2368
	AARD	29.7	12.1807
	R	0.9773	0.8656
	R^2	0.9549	0.7493
7	MSE	0.0011	0.0555
	RMSE	0.0332	0.2356
	AARD	22.18	11.7043
	R	0.98	0.8672
	R^2	0.9573	0.7518
8	MSE	0.0005862	0.0525
	RMSE	0.0242	0.2291
	AARD	14.5626	11.2526
	R	0.9887	0.8749
	R^2	0.9773	0.7654
9	MSE	0.0012	0.0169
	RMSE	0.0341	0.1300
	AARD	22.8695	7.2070
	R	0.9779	0.9616
	R^2	0.9549	0.9245
10	MSE	0.00053	0.0241
	RMSE	0.0230	0.1551
	AARD	19.07	8.5947
	R	0.9897	0.9449
	R^2	0.9795	0.8924
11	MSE	0.0003514	0.0491
	RMSE	0.0187	0.2215
	AARD	11.0381	10.8107

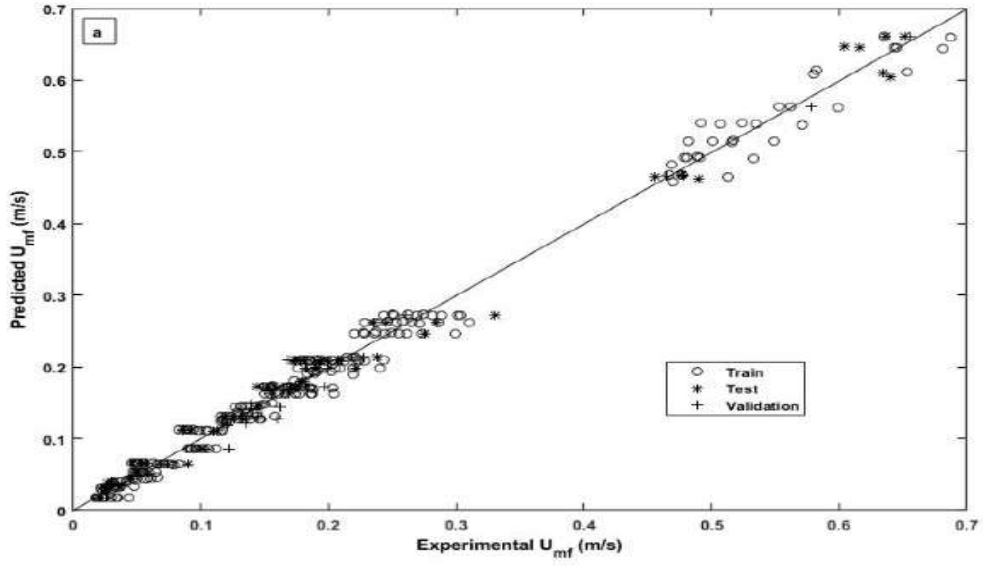
	R	0.9932	0.8836
	R^2	0.9864	0.7807
	MSE	0.00076	0.0145
	RMSE	0.0276	0.1203
12	AARD	17.805	6.4072
	R	0.9856	0.9673
	R^2	0.9705	0.9353
	MSE	0.0004785	0.0175
	RMSE	0.0219	0.1323
13	AARD	16.3479	7.1647
	R	0.9907	0.9601
	R^2	0.9815	0.9217
	MSE	**0.000294**	**0.0146**
	RMSE	**0.0172**	**0.1206**
	AARD	**9.7726**	**6.1144**
14	**R**	**0.9943**	**0.967**
	R^2	**0.9886**	**0.935**
	MSE	0.000315	0.0147
	RMSE	0.017	0.1213
	AARD	10.4095	6.3235
15	R	0.9939	0.9668
	R^2	0.9878	0.9342



FigureIV. 11: Validation plot of MLP.

IV.4. Model checking

IV.*4.1. Estimating the Accuracy of the MLP Model employing data from experience*



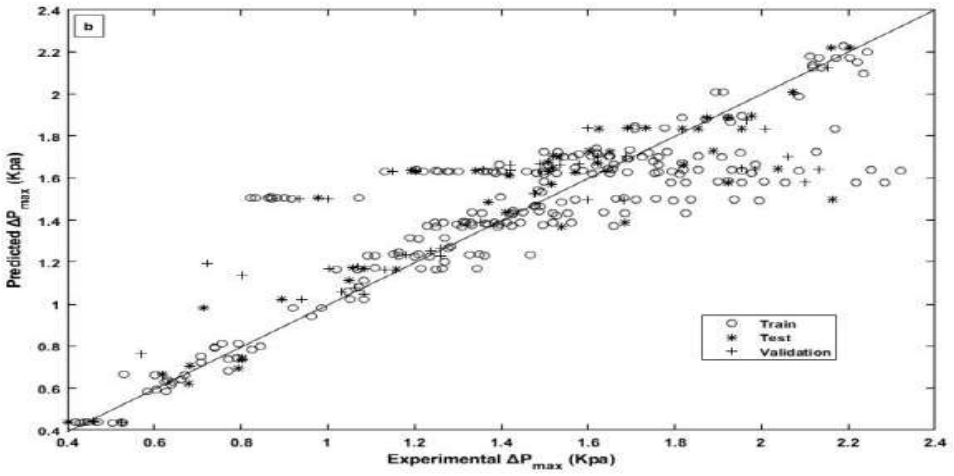


Fig. 12: The experimental data is contrasted with the data generated by the MLP for(a) U_{mf} and (b) ΔP_{max}.

Figure IV.12 depicts the progression of network performance over time. The figure illustrates the linear correlation between the experimentally measured values of ΔP_{max} and U_{mf} and the corresponding predictions generated by the optimal MLP network using the full experimental dataset. The results indicate a satisfactory level of predictive accuracy.

IV.*4.2. Estimating the precision level of the MLP Model through Comparison with Previous Research*

Table IV.3 provides a comparative analysis of the prediction results obtained in this study against those reported in previous research. The table highlights the predictive accuracy of ΔP_{max} and U_{mf} using the Average Absolute Relative Deviation (AARD) as the evaluation metric. This comparison is based on the methodologies and criteria employed in prior studies. Furthermore, our results are evaluated alongside models developed by earlier researchers to assess the relative performance of the proposed approach (Fu et al., 2019; Khani, 2011; Sau et al., 2007; Shao et al., 2020; Wen et al., 1966), As shown in Table IV.3, it is important to note that the correlation coefficients used for comparison with our network are provided in Table III.1. Notably, these previous studies demonstrate lower predictive accuracy compared to the proposed MLP network.

TableIV. 3: The Predictive performance of several paradigms was evaluated in term of AARD.

Proposed model	**AARD (%)** U_{mf}	**AARD (%)** ΔP_{max}	**Ref.**
Khani et al.	39.74	25.94	(Khani, 2011)
Sau et al.	61.61	56.99	(Sau et al., 2007)
Shao et al.	33.80	-	(Shao et al., 2020)
Fu et al	34.30	-	(Fu et al., 2019)
Wen and Yu	26.22	-	(Wen et al., 1966)
This study	9.77	6.11	This study

About the anticipated performance of U_{mf}, as depicted in Table 4, our optimized MLP network demonstrated a superior AARD of 9.77% compared to the models cited in the existing literature, as Sau et al. 2007 (Sau et al., 2007) which had 61.61% with AARD, Khani $^{et\ al.}$ ^{2011} (Khani, 2011) also gave the AARD of 39.74%, Fu et al. 2019 (Fu et al., 2019) had the AARD of 34.30%, Shao et al. 2020 (Shao et al., 2020) also gave a large AARD of 33.80%, and (Wen and Yu 1966 (Wen et al., 1966) which also had the AARD of 26.22%. In addition, our Multilayer Perceptron (MLP) network exhibited superior accuracy in forecasting ΔP_{max}, with an Average Absolute Relative Deviation (AARD) of 6.11%. This performance outperformed the outcomes reported in previous studies, precisely Sau et al. 2007 (Sau et al., 2007) with an AARD of 56.99%, and Khani $^{et\ al.}$ ^{2011} (Khani, 2011) also gave a large AARD of 25.94%.

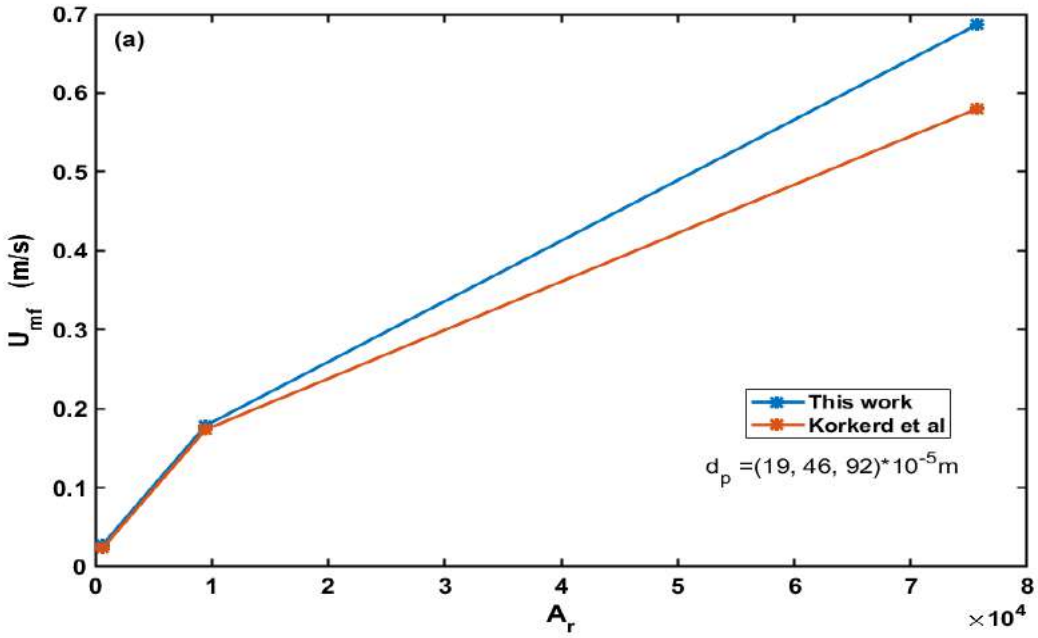
The lack of consideration for specific characteristics in prior studies can be identified as the ca use for the imprecise forecasts of ΔP_{max} and U_{mf}. The investigation conducted by Wen and Yu did not explicitly focus on bed inventory, and similarly, the studies conducted by Khani (2011) (Khani, 2011) and Sau (2007) (Sau et al., 2007) likewise overlooked the consideration of bed geometry. Furthermore, Sau (2007) [24] created the sine function (sin α), which does not align with a cylindrical shape's characteristics and yields zero values. The findings of our prediction investigation demonstrate that our proposed model, which considers the hydraulic diameter and the intricate characteristics of dynamic and kinetic forces, produces the most optimal outcomes. Furthermore, including particle diameters falling within the B-D range of the Geldart classification further illustrated our model's efficacy, establishing it as the most suitable option for the fluidization process.

IV.*5. Parametric study*

In this section, the network was employed to validate the relationships between the independent variables and their corresponding outcomes. The study involved analyzing the deviations between the independent variables and the predicted values of ΔP_{max} and U_{mf}.

IV.5.1. Influence of the Archimedes number on ΔP_{max} and U_{mf}

Figure IV.13 illustrates the effect of the Archimedes number (Ar) on the maximum pressure drop (ΔPmax) and the minimum fluidization velocity (U_{mf}). A clear relationship is observed between Ar and U_{mf}, with U_{mf} increasing as Ar increases. Similarly, ΔPmax also rises with increasing Ar. As previously defined, U_{mf} represents the velocity at which particles become suspended and exhibit behavior analogous to that of a fluid (Hossain et al., 2023), occurring when the upward tensile strength matches the gravitational force. As a result, an augmentation in U_{mf} yields a corresponding augmentation in gravitational forces, leading to a higher A_r. The relationship between the Archimedes number and the maximum pressure drop is complex and is affected by various elements, such as particle diameters (Bahramian, 2021), morphology, and bed



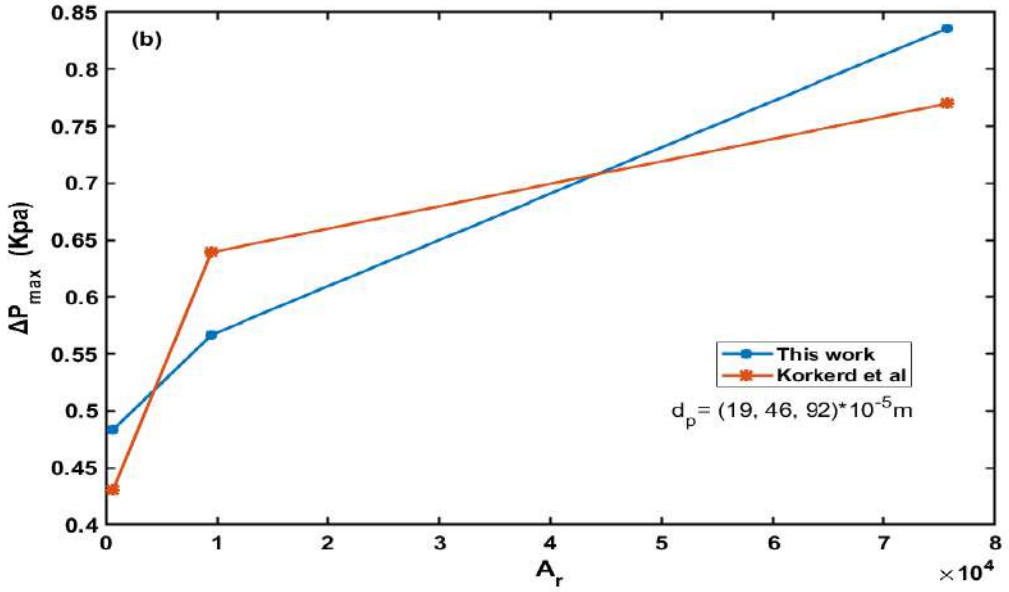


Fig. 13: Impact of the Archimedes number on the (a) U_{mf} and (b) ΔP_{max}

properties. This phenomenon provides clarification regarding the observed marginal increase.

IV.5.2. The Impact of Viscous energy dissipation parameter on ΔP_{max} and U_{mf}

Viscous energy dissipation plays a significant role in determining ΔP_{max} and U_{mf} in fluidized bed systems. As fluid passes through the bed, energy is dissipated due to viscous resistance arising from friction between the fluid and the solid particles (Gao et al., 2022; Kunii et al., 1991). Energy dissipation within the system directly affects both the overall pressure drop and the fluidization behavior. Viscous energy loss plays a crucial role in the observed reduction of pressure across the fluidized bed. As fluid flows over a packed or fluidized bed, its velocity decreases due to viscous effects. Consequently, the pressure along the flow direction diminishes as the fluid interacts with the particles, overcoming their resistance (Islam et al., 2021). Furthermore, viscous energy dissipation acts as a counteracting force to fluidization by reducing the velocity of the fluid as it passes through the bed (Gao et al., 2022; Hossain et al., 2023). Essentially, U_{mf} is determined when equilibrium is achieved between the drag force exerted by the fluid and the gravitational weight of the particles (El ajouri et al., 2022). Fluidization occurs when the drag force exerted by the fluid surpasses the weight of the particles as a result of increased fluid velocity (An et al., 2022; Islam et al., 2021).

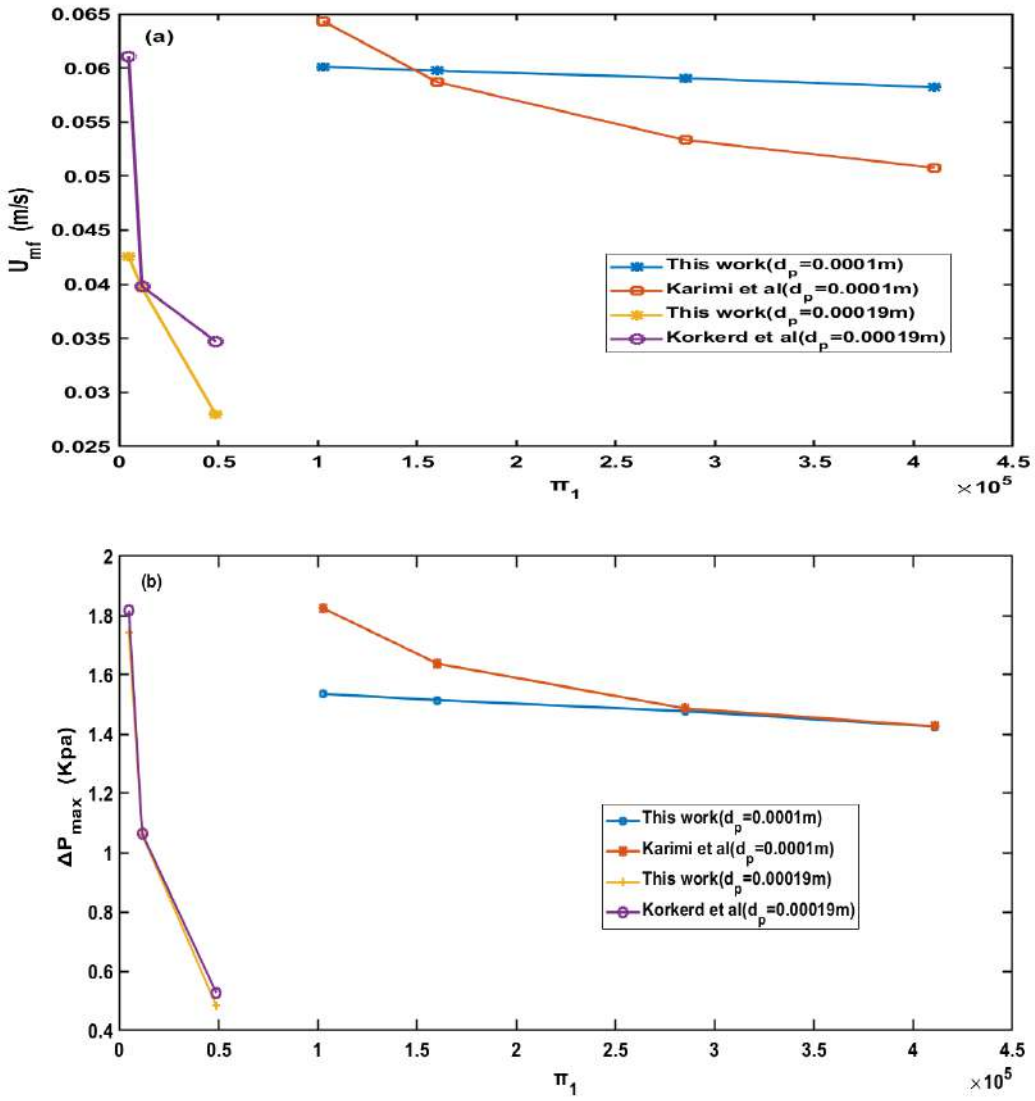


Figure IV. 14: The impact of π_1 on the (a) U_{mf} and (b)ΔP_{max}

Furthermore, the magnitude of the drag forces acting on particles is strongly affected by viscous energy dissipation. As the fluid flows through the bed, energy is dissipated due to viscous forces, generating resistance to the flow. This resistance impedes particle motion, thereby influencing U_{mf}. The relationship is illustrated in Figure IV.14, which demonstrates an inverse correlation between ΔP_{max} and U_{mf} with viscous energy dissipation. As viscous energy dissipation increases, both ΔP_{max} and U_{mf} decrease correspondingly.

IV.5.3. The Impact of Kinetic Energy Dissipation parameter on ΔP_{max} and U_{mf}

The dissipation of kinetic energy plays a significant role in determining both the maximum pressure drop (ΔP_{max}) and the minimum fluidization velocity (U_{mf}) in fluidized bed systems (Davarpanah et al., 2021). As fluid flows through a packed or fluidized bed, kinetic energy is dissipated due to collisions between the fluid and the particles (El ajouri et al., 2022; Hossain et al., 2023). The dissipation of kinetic energy influences both the pressure drop and the fluidization characteristics of the system. Specifically, kinetic energy dissipation contributes to the pressure drop observed in fluidized beds (Gao et al., 2022). As a liquid flows through a bed of particles, interactions between the moving and stationary particles lead to collisions that dissipate kinetic energy (An et al., 2022; El ajouri et al., 2022). With increasing fluid velocity, both the number and frequency of collisions between the fluid and the particles rise correspondingly (Hossain et al., 2023). Consequently, the pressure differential across the system increases, indicating that kinetic energy dissipation resulting from particle–fluid collisions directly affects ΔP_{max} in a fluidized bed. In cases where the fluid velocity is below U_{mf}, particles within the bed undergo a settling process, forming a stationary or densely packed arrangement. Under these conditions, kinetic energy dissipation is crucial in overcoming interparticle forces and initiating the fluidization process (Gao et al., 2022; Islam et al., 2021). During this process, interactions between the fluid and stationary particles facilitate the breakdown of interparticle bonds, thereby reducing resistance to fluidization. Consequently, when kinetic energy dissipation is significant, a higher U_{mf} is required to achieve fluidization (Gidaspow, 1994). In summary, kinetic energy dissipation decreases the energy available to counteract the gravitational forces acting on particles. As a result, achieving fluidization requires a higher gas velocity (Hossain et al., 2023; Mehmood et al., 2023). Furthermore, the augmentation of kinetic energy dissipation can amplify the agitation and blending of particles inside the bed (An et al., 2022; Davarpanah et al., 2021; Gao et al., 2022; Hossain et al., 2023), This leads to a more uniform distribution of particles and gas flow within the bed. Improved mixing can increase resistance to gas flow, resulting in a higher pressure drop. Conversely, when kinetic energy dissipation is reduced, the bed may exhibit more heterogeneous flow patterns or channeling, leading to a lower pressure drop. The data presented in Figure IV.15 demonstrates a negative correlation between kinetic energy dissipation and both ΔP_{max} and U_{mf}, as predicted by the multilayer perceptron (MLP) model.

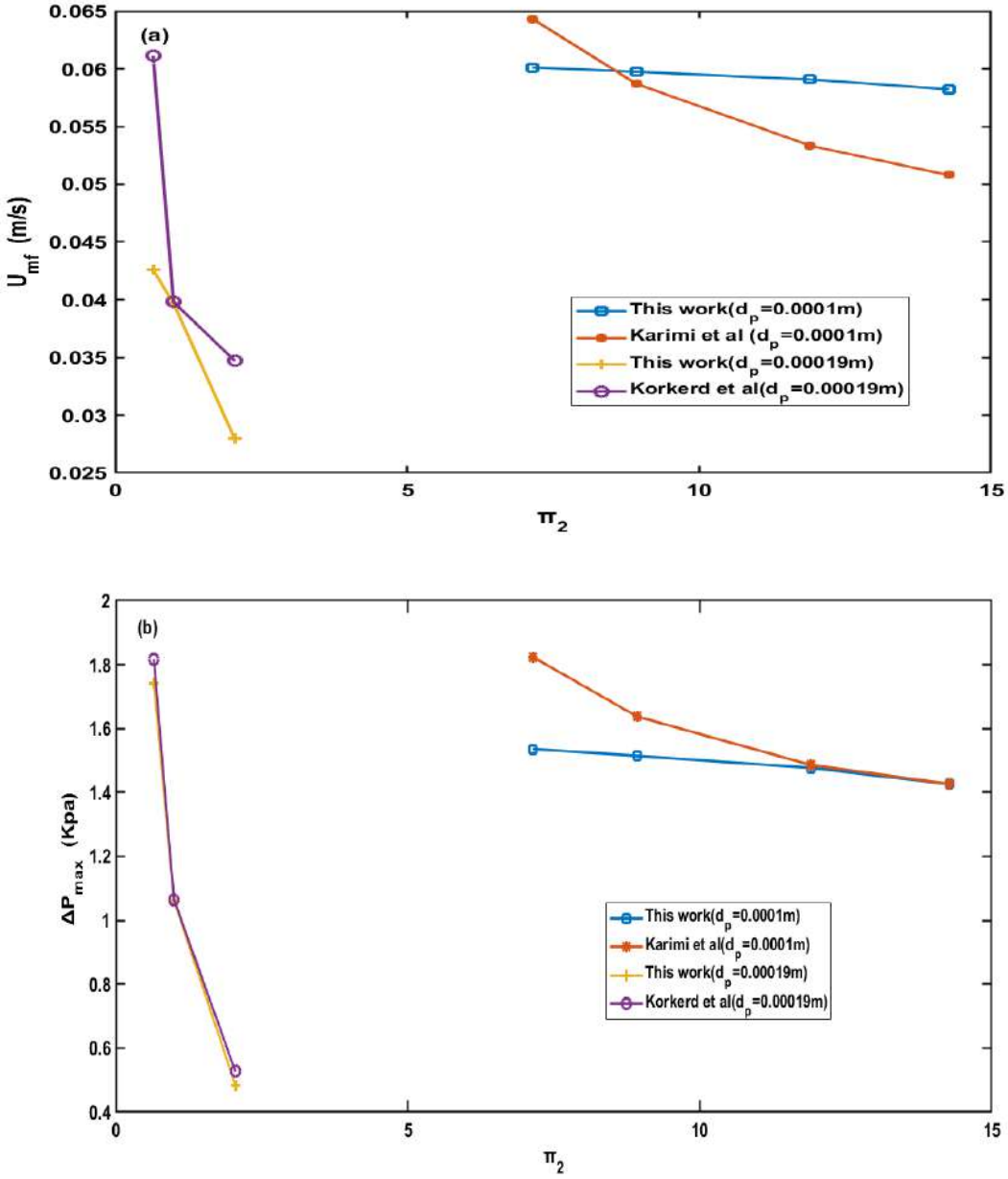


Figure IV. 15: The impact of π_2 on the (a) U_{mf} and (b) ΔP_{max}

IV.6. The mathematical expressions employed for the computation of error rates.

The statistical performance criteria employed in this study are consistent with those utilized in previous publications (Amiri et al., 2023; Ammi et al., 2015; Atsamnia et al., 2017b; Benimam et al., 2020; Hamadache et al., 2016; Melzi et al., 2019; Roubehie Fissa et al., 2019; Salehi et al., 2023) ;

$$\mathrm{AARDX}\ (\%) = \frac{100\ \sum_i^n \left(X_i^{cal} - X_i^{exp}\right)}{n\ X_i^{exp}} \qquad \text{(IV.1)}$$

$$\mathrm{MSE} = \sum_i^n \left(X_i^{cal} - X_i^{exp}\right)^2 / n \qquad \text{(IV.2)}$$

$$\mathrm{RMSE} = \sqrt{\sum_i^n \left(X_i^{cal} - X_i^{exp}\right)^2 / n} \qquad \text{(IV.3)}$$

$$R = \frac{\sum_i^n ((X_i^{cal} - X_{mean}^{cal})(X_i^{exp} - X_{mean}^{exp}))}{\sum_i^n ((X_i^{cal} - X_{mean}^{cal})^2)} \qquad \text{(IV.4)}$$

$$R^2 = 1 - \left(\frac{\sum_i^n \left(X_i^{cal} - X_{mean}^{cal}\right)^2}{\sum_i^n (X_i^{cal} - X_i^{exp})^2}\right) \qquad \text{(IV.5)}$$

IV.7. Information necessary for the utilization of the developed MLP model...

In academic research, it is crucial to provide a detailed description of the instruments employed, such as the Multi-Layer Perceptron (MLP) developed in this study. Such thorough documentation ensures optimal reproducibility and performance within the specific research context. Through an extensive series of experiments and iterative optimization, we have developed an MLP network with the following specifications:

The suggested MLP model has a topology of 3–14–2.

1. TableIV. 4, displays the weights and biases associated with the improved MLP.
2. A logarithmic TANSIG transfer function was employed for all neurons.
3. TableIV. 5, presents the ranges of independent variables and dependent parameters, along with the corresponding standard deviations (STD) values.

TableIV. 4: The best MLP model's bias and Weight coefficients.

Neurons	**Hidden layer Weights (W_{tr})[a]**			**Biases**	**Output layer Weights (W_{tr})[b]**		**Biases**
1	1.7071	1.2924	1.35	0.1903	-37.8843	7.0045	-5.6698
2	5.0476	6.8865	-1.527	5.8316	1.799	125.2531	-86.0185
3	-10.8053	-118.0286	47.5407	-69.433	2.6354	-1.9186	
4	33.9927	-1.7304	2.2004	-35.24	8.5704	8.4417	
5	42.4932	49.2003	-6.4956	25.0998	431.8926	-0.90483	
6	-13.5768	-2.793	2.6809	-12.0514	123.0009	-121.167	
7	-2.0527	7.0506	-4.5856	2.1677	-294.897	59.2541	
8	412.2147	-124.3889	118.4507	397.1431	-152.9009	26.0209	
9	0.038393	4.9068	0.16484	6.0589	5.9332	458.2113	
10	124.9774	268.9693	-216.1003	70.7105	10.3989	-6.8768	
11	-46.8483	-1.411	2.1616	-44.7058	35.0317	35.812	
12	53.8069	0.86227	-1.8655	51.184	1772.8825	-3.2328	
13	9.458	14.9516	-0.23538	25.869	-512.8851	-507.370	
14	-0.065414	3.9811	-4.5948	0.83989	-1198.942	244.4938	

a Weight connection from the input layer to the hidden layer. b Weight connection from the hidden layer to the output layer

TableIV. 5: Statistical analysis of parameters

Parameters	**Symbol**	**Unit**	**Minimum**	**Maximum**	**Mean**	**STD**
Archemide number	A_r	-	308.94	67598.42	16459.75	20011.38
Viscosity number	π_1	-	0.00	60311.99	3796.96	10836.80
Cinetic number	π_2	-	0.000032	2.277048	0.280739	0.498362
Minimum velocity	U_{mf}	m/s	0.17400	0.687700	0.195267	0.160959
Pressure drop	ΔP_{max}	Kpa	0.331400	2.517710	1.420973	0.473686

IV.8. Conclusion

This study's results suggest that the built MLP model demonstrated higher performance compared to other models when it came to predicting the values of ΔP_{max} and U_{mf}. The Average Absolute Relative Deviation (AARD) for ΔP_{max} was determined to be 6.11%, while for U_{mf}, it was found to be 9.77%. The model that was put out demonstrated a Mean Squared Error (MSE) of 0.0146 and 2.9×10^{-4}, along with Root Mean Squared Error (RMSE) values of 0.120 and 0.0172 for the prediction of ΔP_{max} and U_{mf}, respectively. In addition, the regression coefficients for ΔP_{max} and U_{mf} are 0.967 and 0.994, respectively. The corresponding coefficients of determination, R^2, are 0.935 and 0.989, demonstrating a high level of concordance between the experimental and predictive data.

General conclusion and Outlook

General Conclusion and Outlook

The present study successfully developed and validated a novel modeling framework for predicting key hydrodynamic parameters—namely the maximum pressure drop (ΔP_{max}) and the minimum fluidization velocity (U_{mf})—in both conical and cylindrical gas–solid fluidized beds. By deriving two new dimensionless numbers (π_1 and π_2) based on the Ergun equation, this research established an improved understanding of the dissipation of viscous and kinetic energy in fluidized systems. These parameters, in combination with the Archimedes number and the hydraulic diameter, provided a robust and physically meaningful input set for the construction of an artificial neural network model.

The multilayer perceptron (MLP) network, optimized with a 3–14–2 topology, demonstrated exceptional predictive performance and strong correlation with experimental data. The achieved statistical indicators—AARD of 6.11% and 9.77%, RMSE of 0.120 and 0.0172, and R^2 values of 0.935 and 0.989 for ΔP_{max} and U_{mf} respectively—confirm the precision and reliability of the developed model. Compared with previously published correlations, the proposed approach significantly enhances prediction accuracy, especially through the inclusion of geometrical and energy-dissipation parameters often neglected in earlier models. The integration of hydraulic diameter as a differentiating parameter between bed geometries further strengthens the generalization capacity of the model.

Beyond its methodological contributions, this study highlights the potential of artificial intelligence—specifically neural network-based modeling—in fluidization research. The results demonstrate that data-driven models, when guided by dimensionless physical insights, can bridge the gap between empirical correlations and complex multiphase flow phenomena. Such models not only reduce computational cost compared with CFD simulations but also maintain high predictive reliability across a wide range of operating conditions.

Outlook

While the developed MLP model offers a valuable predictive tool, several avenues remain open for future exploration. Extending the database to include broader particle types, fluid properties, and operational regimes will enhance the model's universality. Furthermore, coupling

the proposed neural architecture with hybrid physics-informed approaches could improve its interpretability and extrapolative performance. Incorporating real-time monitoring and adaptive learning algorithms would also allow the model to dynamically update as new experimental data become available.

Future research should also investigate the application of the proposed dimensionless framework to other multiphase systems such as liquid–solid or gas–liquid fluidized beds. Additionally, exploring the influence of non-Newtonian fluids, particle shape irregularities, and bed-scale turbulence through deep learning or hybrid ANN–CFD techniques could yield a more comprehensive understanding of fluidization behavior.

Ultimately, the developed approach contributes not only to the accurate prediction of ΔP_{max} and U_{mf} but also lays the groundwork for intelligent, data-driven optimization of industrial fluidized bed systems. By merging fundamental physical principles with machine learning techniques, this research paves the way toward more efficient, adaptive, and sustainable designs in chemical and process engineering.

References bibliographic

References bibliographic

Abd-Rabbo, M. A., Sakr, R. Y., Mohammad, M. A., & Mandour, M. M. (2020). Heat Transfer From Elliptic Cylinder Immersed In A Fluidized Bed. *Journal of Engineering Research*, *166*(Jun), M68–M83. doi: 10.21608/erj.2020.138868

Abdallah el hadj, A., Laidi, M., Si-Moussa, C., & Hanini, S. (2017). Novel approach for estimating solubility of solid drugs in supercritical carbon dioxide and critical properties using direct and inverse artificial neural network (ANN). *Neural Computing and Applications*, *28*(1), 87–99. doi: 10.1007/s00521-015-2038-1

Aghajani, M., Müller-Steinhagen, H., & Jamialahmadi, M. (2004). Experimental results and models for solid/liquid fluidized beds involving newtonian and non-newtonian liquids. *Developments in Chemical Engineering and Mineral Processing*, *12*(3–4), 403–426. doi: 10.1002/apj.5500120415

Agu, C. E., Tokheim, L. A., Eikeland, M., & Moldestad, B. M. E. (2019). Improved models for predicting bubble velocity, bubble frequency and bed expansion in a bubbling fluidized bed. *Chemical Engineering Research and Design*, *141*, 361–371. doi: 10.1016/j.cherd.2018.11.002

Aguirre, F., Sebastian, A., Le Gallo, M., Song, W., Wang, T., Yang, J. J., Lu, W., Chang, M.-F., Ielmini, D., & Yang, Y. (2024). Hardware implementation of memristor-based artificial neural networks. *Nature Communications*, *15*(1), 1974.

Al-Eshmawy, H., Abdelfatah, M. A., & El-Fiky, G. S. (2024). A proposed neural network model for obtaining precipitable water vapor. *Journal of Applied Geodesy*, *18*(2), 177–187.

Aleksić, I., Crossed D Signuriš, J., Ibrić, S., & Parojčić, J. (2015). An investigation into the usefulness of different empirical modeling techniques for better control of spray-on fluidized bed melt granulation. *International Journal of Pharmaceutics*, *496*(2), 627–635. doi: 10.1016/j.ijpharm.2015.11.001

Aleksić, I., Crossed D Signuriš, J., Ilić, I., Ibrić, S., Parojčić, J., & Srčič, S. (2014). In silico modeling of in situ fluidized bed melt granulation. *International Journal of Pharmaceutics*, *466*(1–2), 21–30. doi: 10.1016/j.ijpharm.2014.02.045

Ali Reza, B., & Mansour, K. (2010). CFD modeling of TiO2 nano-agglomerates hydrodynamics in a conical fluidized bed unit with experimental validation. *Iranian Journal of Chemistry and Chemical Engineering*, *29*(2), 105–120.

Amiri, S., Larki, E., Esmaile, N., & Mofavvaz, S. (2023). The application of fuzzy inference system and adaptive neuro-fuzzy inference system as artificial intelligence methods for modeling and prediction of the ceftriaxone removal percentage using nano zero-valent iron coupled with strontium hexaferrite. *Iranian Journal of Chemistry and Chemical Engineering*.

Ammi, Y., Khaouane, L., & Hanini, S. (2015). Prediction of the rejection of organic compounds (neutral and ionic) by nanofiltration and reverse osmosis membranes using neural networks. *Korean Journal of Chemical Engineering*, *32*(11), 2300–2310. doi: 10.1007/s11814-015-

0086-y

An, Z., Wang, H., & Zhang, Y. (2022). Prediction of defluidization behavior using particle apparent viscosity. *Korean Journal of Chemical Engineering*, *39*(10), 2875–2882.

Anbazhagan, S., Thiruvengadam, V., & Kulanthai, K. (2020). Adaptive neuro-fuzzy inference system and artificial neural network modeling for the adsorption of methylene blue by novel adsorbent in a fixed-bed column method. *Iranian Journal of Chemistry and Chemical Engineering*, *39*(6), 75–93. doi: 10.30492/ijcce.2019.36407

Ariana, M. A., Vaferi, B., & Karimi, G. (2015). Prediction of thermal conductivity of alumina water-based nanofluids by artificial neural networks. *Powder Technology*, *278*, 1–10.

Atsamnia, D., Hamadache, M., Hanini, S., Benkortbi, O., & Oukrif, D. (2017a). Prediction of the antibacterial activity of garlic extract on E. coli, S. aureus and B. subtilis by determining the diameter of the inhibition zones using artificial neural networks. *Lwt*, *82*, 287–295. doi: 10.1016/j.lwt.2017.04.053

Atsamnia, D., Hamadache, M., Hanini, S., Benkortbi, O., & Oukrif, D. (2017b). Prediction of the antibacterial activity of garlic extract on E. coli, S. aureus and B. subtilis by determining the diameter of the inhibition zones using artificial neural networks. *Lwt*, *82*, 287–295. doi: 10.1016/j.lwt.2017.04.053

Ayoubi, S., & Sahrawat, K. L. (2011). Comparing multivariate regression and artificial neural network to predict barley production from soil characteristics in Northern Iran. *Archives of Agronomy and Soil Science*, *57*(5), 549–565. doi: 10.1080/03650341003631400

Bahramian, A. R. (2021). Application of the force balance model and fractal scaling analysis for size estimation of the complex-agglomerates in a conical fluidized bed. *Iranian Journal of Chemistry and Chemical Engineering*, *40*(3), 955–970. doi: 10.30492/ijcce.2020.38038

Bai, D., Issangya, A. S., & Grace, J. R. (1999). Characteristics of gas-fluidized beds in different flow regimes. *Industrial and Engineering Chemistry Research*, *38*(3), 803–811. doi: 10.1021/ie9803873

Bai, W., Chu, D., & He, Y. (2021). The minimum fluidization velocity and dynamic characteristics of agglomerated carbon nanotube in a tapered fluidized bed at elevated temperature. *Chemical Engineering Research and Design*, *168*, 239–253. doi: 10.1016/j.cherd.2021.02.014

Bar, N., Bandyopadhyay, T. K., Biswas, M. N., & Das, S. K. (2010). Prediction of pressure drop using artificial neural network for non-Newtonian liquid flow through piping components. *Journal of Petroleum Science and Engineering*, *71*(3–4), 187–194. doi: 10.1016/j.petrol.2010.02.001

Bar, N., Biswas, M. N., & Das, S. K. (2010). Prediction of pressure drop using artificial neural network for gas non-newtonian liquid flow through piping components. *Industrial and Engineering Chemistry Research*, *49*(19), 9423–9429. doi: 10.1021/ie1007739

Benimam, H., Si-Moussa, C., Laidi, M., & Hanini, S. (2020). Modeling the activity coefficient at infinite dilution of water in ionic liquids using artificial neural networks and support vector

machines. *Neural Computing and Applications*, *32*(12), 8635–8653. doi: 10.1007/s00521-019-04356-w

Biswal, K. C., Bhowmik, T., & Roy, G. K. (1985). Prediction of Minimum Fluidization Velocity for Gas-Solid Fluidization of Regular Particles in Conical Vessels. In The Chemtcal Engmeenng Journal (Vol. 30).

Biswal, K. C., & Roy, G. K. (1985). Prediction of Fluctuation Ratio for Gas-Solid Fluidization of Irregular Particles in Conical Vessels. *Journal of the Institution of Engineers (India): Chemical Engineering Division*, *65*(February 1983), 32–35.

Bouarra, N., Kherouf, S., Nadji, N., Nouri, L., Boudjemaa, A., Djerad, S., & Bachari, K. (2024). Quantitative structure-electrochemistry relationship modeling of a series of anticancer agents using MLR and ANN approaches. *Chemical Product and Process Modeling*, *0*.

Bousselma, A., Abdessemed, D., Tahraoui, H., & Amrane, A. (2021). Artificial Intelligence and Mathematical Modelling of the Drying Kinetics of Pre-treated Whole Apricots. *Kemija u Industriji*, *69*(11–12), 137–152. doi: 10.15255/kui.2020.079

Brea, F. M., Edwards, M. F., & Wilkinson, W. L. (1976). The flow of non-Newtonian slurries through fixed and fluidised beds. *Chemical Engineering Science*, *31*(5), 329–336. doi: 10.1016/0009-2509(76)80001-2

Broniarz-Press, L., Agacinski, P., & Rozanski, J. (2007). Shear-thinning fluids flow in fixed and fluidised beds. *International Journal of Multiphase Flow*, *33*(6), 675–689. doi: 10.1016/j.ijmultiphaseflow.2006.12.004

Chalermsinsuwan, B., Chanchuey, T., Buakhao, W., Gidaspow, D., & Piumsomboon, P. (2012). Computational fluid dynamics of circulating fluidized bed downer: Study of modeling parameters and system hydrodynamic characteristics. *Chemical Engineering Journal*, *189–190*, 314–335. doi: 10.1016/j.cej.2012.02.020

Chen, J., Li, H., Lv, X., & Zhu, Q. (2015). A structure-based drag model for the simulation of Geldart A and B particles in turbulent fluidized beds. *Powder Technology*, *274*, 112–122. doi: 10.1016/j.powtec.2015.01.010

Chen, X., Zhong, W., & Heindel, T. J. (2019). Using stereo XPTV to determine cylindrical particle distribution and velocity in a binary fluidized bed. *AIChE Journal*, *65*(2), 520–535. doi: 10.1002/aic.16485

Chhabra, R. P. (1993). Estimation of the minimum fluidization velocity for beds of spherical particles fluidized by power law liquids. *Powder Technology*, *76*(2), 225–228. doi: 10.1016/S0032-5910(05)80031-2

Chhabra, Raj P, & Patel, S. A. (2023). *Bubbles, drops, and particles in non-Newtonian fluids*. CRC press.

Chhabra, Rajendra P., Comiti, J., & Machač, I. (2001). Flow of non-Newtonian fluids in fixed and fluidised beds. *Chemical Engineering Science*, *56*(1), 1–27. doi: 10.1016/S0009-2509(00)00207-4

Comments on “comparison of commonly used correlations for minimum fluidization velocity of

small solid particles." (1981). In Powder Technology (Vol. 30, Issue 1, pp. 95–96). doi: 10.1016/0032-5910(81)85031-0

Davarpanah, M., Shi, H., Nikrityuk, P., & Hashisho, Z. (2021). Verification of semi-empirical relations for predicting fluidization in a fluidized bed using CFD. *Chemical Engineering Research and Design*, *173*, 289–304. doi: 10.1016/j.cherd.2021.07.017

Davidson, J. F., & Harrison, D. (1964). Fluidised particles. *Journal of the Franklin Institute*, *277*(2), 194. doi: 10.1016/0016-0032(64)90081-x

Delebarre, A. (2004). Revisiting the Wen and Yu equations for minimum fluidization velocity prediction. *Chemical Engineering Research and Design*, *82*(5), 587–590. doi: 10.1205/026387604323142621

Depypere, F., Pieters, J. G., & Dewettinck, K. (2005). Expanded bed height determination in a tapered fluidised bed reactor. *Journal of Food Engineering*, *67*(3), 353–359. doi: 10.1016/j.jfoodeng.2004.04.039

Dilmi, M., Benseghir, A., Dilmi, M., & Benseridi, H. (2023). Calculation of Reynolds equation for the generalized non-Newtonian fluids and its asymptotic behavior in a thin domain. *Georgian Mathematical Journal*, *0*.

El-Moumen, H., & El Akchioui, N. (2024). Fluidization of Stochastic Petri Nets via Continuous Petri Nets: Comparative Study. *Journal of Control, Automation and Electrical Systems*, 1–14.

El ajouri, O., Lahlaouti, M. L., & Kharbouch, B. (2022). CFD-simulation of gas-solid flow in bubbling fluidized bed reactor. *E3S Web of Conferences*, *336*. doi: 10.1051/e3sconf/202233600059

Ergun, S. (1952a). Determination of geometric surface area of crushed porous solids. *Analytical Chemistry*, *24*(2), 388–393.

Ergun, S. (1952b). Fluid flow through packed columns. *Chem. Eng. Prog.*, *48*(2), 89–94.

Esam Saleh, & Touzout Feriel. (2021). Decontamination of water by dead biomass. *UNIVERSITE YAHIA FARES DE MEDEA Http://Dspace.Univ-Medea.Dz/Handle/123456789/4956*. Retrieved from http://dspace.univ-medea.dz/handle/123456789/4956

Fang, S., Wei, Y., Fu, L., Tian, G., & Qu, H. (2020). Modeling of the minimum fluidization velocity and the incipient fluidization pressure drop in a conical fluidized bed with negative pressure. *Applied Sciences*, *10*(24), 8764.

Farizhandi, A. A. K., Zhao, H., & Lau, R. (2016). Modeling the change in particle size distribution in a gas-solid fluidized bed due to particle attrition using a hybrid artificial neural network-genetic algorithm approach. *Chemical Engineering Science*, *155*, 210–220. doi: 10.1016/j.ces.2016.08.015

Felipe, C. A. S., & Rocha, S. C. S. (2007). Prediction of minimum fluidization velocity of gas-solid fluidized beds by pressure fluctuation measurements - Analysis of the standard deviation methodology. *Powder Technology*, *174*(3), 104–113. doi:

10.1016/j.powtec.2007.01.015

Feng, R., Li, J., Cheng, Z., Yang, X., & Fang, Y. (2017). Influence of particle size distribution on minimum fluidization velocity and bed expansion at elevated pressure. *Powder Technology*, *320*, 27–36. doi: 10.1016/j.powtec.2017.07.024

Frikha, S. (2023). Numerical and experimental study of the fluidization of alumina particles. *Euro-Mediterranean Journal for Environmental Integration*, 1–9.

Fu, Z., Zhu, J., Barghi, S., Zhao, Y., Luo, Z., & Duan, C. (2019). Minimum fluidization velocity growth due to bed inventory increase in an Air Dense Medium Fluidized Bed. *Chemical Engineering Journal*, *359*, 1372–1378.

Gao, Z., Liu, G., Guo, X., & Lu, H. (2022). A dynamic coefficient of restitution applied to two-fluid model in liquid-solid fluidized bed. *Powder Technology*, *402*, 117335.

Geldart, D. (2004). Expansion of gas fluidized beds. *Industrial and Engineering Chemistry Research*, *43*(18), 5802–5809. doi: 10.1021/ie040180b

Gernon, T. M., & Gilbertson, M. A. (2012). Segregation of particles in a tapered fluidized bed. *Powder Technology*, *231*, 88–101. doi: 10.1016/j.powtec.2012.07.053

Gidaspow, D. (1994). *Multiphase flow and fluidization: continuum and kinetic theory descriptions*. Academic press.

Gupta, S. K., Agarwal, V. K., Singh, S. N., Seshadri, V., Mills, D., Singh, J., & Prakash, C. (2009). Prediction of minimum fluidization velocity for fine tailings materials. *Powder Technology*, *196*(3), 263–271. doi: 10.1016/j.powtec.2009.08.003

Hamadache, M., Hanini, S., Benkortbi, O., Amrane, A., Khaouane, L., & Moussa, C. S. (2016). Artificial neural network-based equation to predict the toxicity of herbicides on rats. *Chemometrics and Intelligent Laboratory Systems*, *154*, 7–15. doi: 10.1016/j.chemolab.2016.03.007

Han, M., Zhou, Y., & Zhu, J. (2020). Improvement on flowability and fluidization of Group C particles after nanoparticle modification. *Powder Technology*, *365*, 208–214. doi: 10.1016/j.powtec.2019.07.026

Heddam, S. (2016). Secchi Disk Depth Estimation from Water Quality Parameters: Artificial Neural Network versus Multiple Linear Regression Models? *Environmental Processes*, *3*(2), 525–536. doi: 10.1007/s40710-016-0144-4

Hossain, N., & Metcalfe, R. (2023). Performance analysis of a 2D numerical model in estimating minimum fluidization velocity for fluidized beds. *Particuology*, *77*, 116–127.

Irfan, M. F., Mjalli, F. S., & Kim, S. D. (2012). Modeling of NH 3-NO-SCR reaction over CuO/γ-Al 2O 3 catalyst in a bubbling fluidized bed reactor using artificial intelligence techniques. *Fuel*, *93*, 245–251. doi: 10.1016/j.fuel.2011.09.043

Islam, M. T., & Nguyen, A. V. (2021). Effect of particle size and shape on liquid–solid fluidization in a HydroFloat cell. *Powder Technology*, *379*, 560–575. doi: 10.1016/j.powtec.2020.10.080

Jaiswal, A. K., Sundararajan, T., & Chhabra, R. P. (1992). Simulation of non-newtonian fluid flow through fixed and fluidized beds of spherical particles. *Numerical Heat Transfer; Part A: Applications*, *21*(3), 275–297. doi: 10.1080/10407789208944877

Jing, S., Hu, Q., Wang, J., & Jin, Y. (2000). Fluidization of coarse particles in gas-solid conical beds. *Chemical Engineering and Processing: Process Intensification*, *39*(4), 379–387. doi: 10.1016/S0255-2701(99)00103-8

Kamari, E., Hajizadeh, A. A., & Kamali, M. R. (2020). Experimental investigation and estimation of light hydrocarbons gas-liquid equilibrium ratio in gas condensate reservoirs through artificial neural networks. *Iranian Journal of Chemistry and Chemical Engineering*, *39*(6), 163–172. doi: 10.30492/ijcce.2019.36496

Karimi, M., Vaferi, B., Hosseini, S. H., & Rasteh, M. (2018). Designing an Efficient Artificial Intelligent Approach for Estimation of Hydrodynamic Characteristics of Tapered Fluidized Bed from Its Design and Operating Parameters. *Industrial and Engineering Chemistry Research*, *57*(1), 259–267. doi: 10.1021/acs.iecr.7b02869

Kato, K., Shibasakl, H., Tamura, K., Arita, S., Wang, C., & Takarada, T. (1989). Particle holdup in a fast fluidized bed. In Journal of Chemical Engineering of Japan (Vol. 22, Issue 2, pp. 130–136). doi: 10.1252/jcej.22.130

Kawase, Y., & Ulbrecht, J. J. (1985). Mass and momentum transfer with non-Newtonian fluids in fluidized beds. *Chem. Engng. Commun.*, *32*(1–5), 263–288. doi: 10.1080/00986448508911651

Kelfoun, K., & Proaño, A. (2023). Large-scale volcanic deposit fluidization by dilute pyroclastic density currents. *Nature Geoscience*, *16*(6), 499–504.

Khan, A. R., & Richardson, J. F. (1990). Corrections for "fluid-particle interactions and flow characteristics of fluidized beds and settling suspensions of spherical particles." *Chemical Engineering Communications*, *92*(1), 245. doi: 10.1080/00986449008911433

Khani, M. H. (2011). Models for prediction of hydrodynamic characteristics of gas-solid tapered and mini-tapered fluidized beds. *Powder Technology*, *205*(1–3), 224–230. doi: 10.1016/j.powtec.2010.09.018

Khaouane, L., Si-Moussa, C., Hanini, S., & Benkortbi, O. (2012). Optimization of culture conditions for the production of pleuromutilin from pleurotus mutilus using a hybrid method based on central composite design, neural network, and particle swarm optimization. *Biotechnology and Bioprocess Engineering*, *17*(5), 1048–1054. doi: 10.1007/s12257-012-0254-4

Korkerd, K., Soanuch, C., Gidaspow, D., Piumsomboon, P., & Chalermsinsuwan, B. (2021). Artificial neural network model for predicting minimum fluidization velocity and maximum pressure drop of gas fluidized bed with different particle size distributions. *South African Journal of Chemical Engineering*, *37*, 61–73. doi: 10.1016/j.sajce.2021.04.003

Krzywanski, J., Blaszczuk, A., Czakiert, T., Rajczyk, R., & Nowak, W. (2014). Artificial intelligence treatment of NOX emissions from CFBC in air and oxy-fuel conditions. *CFB-11: Proceedings of the 11th International Conference on Fluidized Bed Technology*, *July*

2022, 619–624.

Kulicke, W.-M., & Wallbaum, U. (1985). Determination of first and second normal stress differences in polymer solutions in steady shear flow and limitations caused by flow irregularities. *Chemical Engineering Science*, *40*(6), 961–972.

Laidi, M., & Hanini, S. (2013). Optimal solar COP prediction of a solar-assisted adsorption refrigeration system working with activated carbon/methanol as working pairs using direct and inverse artificial neural network. *International Journal of Refrigeration*, *36*(1), 247–257. doi: 10.1016/j.ijrefrig.2012.09.016

Lashkarbolooki, M., Vaferi, B., & Mowla, D. (2012). Using Artificial Neural Network to Predict the Pressure Drop in a Rotating Packed Bed. *Separation Science and Technology (Philadelphia)*, *47*(16), 2450–2459. doi: 10.1080/01496395.2012.665975

Laxmi, R. R., & Kumar, A. (2011). Weather based forecasting model for crops yield using neural network approach. *Statistics and Applications*, *9*, 55–69.

Leturia, M., Benali, M., Lagarde, S., Ronga, I., & Saleh, K. (2014). Characterization of flow properties of cohesive powders: A comparative study of traditional and new testing methods. *Powder Technology*, *253*, 406–423. doi: 10.1016/j.powtec.2013.11.045

Li, Z., Wang, C., & Wang, Q. (2023). On eigenvalues of a high-dimensional Kendall's rank correlation matrix with dependence. *Science China Mathematics*, *66*(11), 2615–2640.

Lin, C. L., Wey, M. Y., & You, S. Da. (2002). The effect of particle size distribution on minimum fluidization velocity at high temperature. *Powder Technology*, *126*(3), 297–301. doi: 10.1016/S0032-5910(02)00074-8

Liu, L., Li, J., Yang, J., Wang, J., Wang, Y., Chen, S., Feng, L., Xie, C., & Zhu, J. (2023). The absorbing boundary conditions of Newtonian fluid flowing across a semi-infinite plate with different velocities and pressures. *Zeitschrift Für Naturforschung A*, *0*.

M Mandour, M., A Abd-Rabboa, M., Y Sakrb, R. Y., & A Mohammada, M. (2020). Heat Transfer From Elliptic Cylinder Immersed In A Fluidized Bed. *Engineering Research Journal*, *166*, 389–405.

Machac, I., Mikulasek, P., & Ulbrichova, W. A. (1993). *Non-newtonian fluidization particle beds of spherical-*. *48*(11).

Machač, I., Šiška, B., Lecjaks, Z., & Bena, J. (1997). Fluidization of spherical particle beds with non-Newtonian fluids in columns of rectangular cross-section. *Chemical Engineering Science*, *52*(19), 3409–3414. doi: 10.1016/S0009-2509(97)00135-8

Maiti, S. B., Let, S., Bar, N., & Das, S. K. (2018). Non-spherical solid-non-Newtonian liquid fluidization and ANN modelling: Minimum fluidization velocity. *Chemical Engineering Science*, *176*, 233–241. doi: 10.1016/j.ces.2017.10.050

Malkin, A. Y., & Isayev, A. I. (2022). *Rheology: concepts, methods, and applications*. Elsevier.

Marahel, F., Mombeeni Goodajdar, B., Basari, N., Niknam, L., & Ghazali, A. A. (2022). Applying Neural Network Model for Adsorption Methyl Paraben (MP) Dye Using Ricinus

Communis-capeed Fe3O4 NPs Synthesized from Aqueous Solution. *Iranian Journal of Chemistry and Chemical Engineering*, *41*(7), 2358–2377. doi: 10.30492/ijcce.2021.527025.4636

Marquardt, D. W. (1963). An algorithm for least-squares estimation of nonlinear parameters. *Journal of the Society for Industrial and Applied Mathematics*, *11*(2), 431–441.

Marseille, E. C. (n.d.). *7 lits fluidises*.

Mathur, K. B., & Gishler, P. E. (1955). A technique for contacting gases with coarse solid particles. *AIChE Journal*, *1*(2), 157–164. doi: 10.1002/aic.690010205

Matsusaka, S., Kobayakawa, M., Mizutani, M., Imran, M., & Yasuda, M. (2013). Bubbling behavior of a fluidized bed of fine particles caused by vibration-induced air inflow. *Scientific Reports*, *3*, 1–5. doi: 10.1038/srep01190

McCabe, Warren L, Smith, J. C., & Harriott, P. (2005). Adsorption and Fixed-Bed Separations. *Unit Operations of Chemical Engineering*, 836–878.

McCabe, Warren Lee, Smith, J. C., & Harriott, P. (1993). *Unit operations of chemical engineering* (Vol. 5). McGraw-hill New York.

Mehdizad, M., & Kouhikamali, R. (2018). Numerical investigation of the minimum fluidization velocity in a gas–solid fluidized bed using discrete phase model. In Journal of the Brazilian Society of Mechanical Sciences and Engineering (Vol. 40, Issue 5). Springer Verlag. doi: 10.1007/s40430-018-1176-7

Mehmood, A., Muhammad, A., Sattar, H., & Jamal, Y. (2023). Understanding parameters affecting system transfer efficiency (STE) of powder coatings in the paint industry. *Iranian Journal of Chemistry and Chemical Engineering*.

Melzi, N., Zentou, H., Laidi, M., Hanini, S., Ammi, Y., & Khaouane, L. (2019). Usporedna studija predviđanja koeficijenta molekularne difuzije za polarni i nepolarni binarni plin pomoću neuronskih mreža i višestrukih linearnih regresija. *Kemija u Industriji*, *68*(11–12), 573–582. doi: 10.15255/kui.2019.010

Mića, V., Jelena, J., Goran, V., Branislav, S., & Aleksandar, P. (2015). Experimental investigation of the drying kinetics of corn in a packed and fluidized bed. *Iranian Journal of Chemistry and Chemical Engineering*, *34*(3), 43–49.

Olazar, M., San José, M. J., Aguayo, A. T., Arandes, J. M., & Bilbao, J. (1994). Hydrodynamics of nearly flat base spouted beds. *The Chemical Engineering Journal and The Biochemical Engineering Journal*, *55*(1–2), 27–37. doi: 10.1016/0923-0467(94)87003-9

Ounnar, A., Arrar, J., & Bentahar, F. (2009). Hydrodynamic behaviour of upflowing jet in fluidized bed: Velocity profiles of sand particles. *Chemical Engineering and Processing: Process Intensification*, *48*(2), 617–622. doi: 10.1016/j.cep.2008.07.005

Padhi, S. K., Singh, R. K., & Agrawal, S. K. (2010). Effect of twisted tape baffles on pressure drop, fluctuation and expansion ratios in gas - Solid fluidized bed. *Iranian Journal of Chemistry and Chemical Engineering*, *29*(1), 33–40.

Peng, Y., & Fan, L. T. (1997). *Hydrodynamic characteristics of fluidization in liquid-solid tapered beds* (Vol. 52, Issue 14).

Petrović, J., Chansanroj, K., Meier, B., Ibrić, S., & Betz, G. (2011). Analysis of fluidized bed granulation process using conventional and novel modeling techniques. *European Journal of Pharmaceutical Sciences*, *44*(3), 227–234. doi: 10.1016/j.ejps.2011.07.013

Pezhhanfar, S., Zarei, M., Shekaari Teymourloue, T., & Khalilzadeh, M. (2021). Neural Network, Isotherm, and Kinetic Study for Wastewater Treatment Using Populus alba's Pruned Material. *Iranian Journal of Chemistry and Chemical Engineering*, *40*(6), 1868–1881. doi: 10.30492/ijcce.2020.43472

Philippsen, C. G., Vilela, A. C. F., & Zen, L. D. (2015). Fluidized bed modeling applied to the analysis of processes: Review and state of the art. *Journal of Materials Research and Technology*, *4*(2), 208–216. doi: 10.1016/j.jmrt.2014.10.018

Qiao, Z., Wang, Z., Zhang, C., Yuan, S., Zhu, Y., & Wang, J. (2012). PVAm–PIP/PS composite membrane with high performance for CO_2/N_2 separation. *AIChE Journal*, *59*(4), 215–228. doi: 10.1002/aic

Rama Sastry, S. V. A. (2022). Prediction of Optimum Process Parameters for Karanja Biodiesel Production Using Support Vector Machine, Genetic Algorithm and Particle Swarm Optimization. *Iranian Journal of Chemistry and Chemical Engineering*, *41*(5), 1821–1833. doi: 10.30492/IJCCE.2021.128278.4153

Rasteh, M., Farhadi, F., & Ahmadi, G. (2018). Empirical models for minimum fluidization velocity of particles with different size distribution in tapered fluidized beds. *Powder Technology*, *338*, 563–575. doi: 10.1016/j.powtec.2018.07.077

Rasteh, M., Farhadi, F., & Bahramian, A. (2015). Hydrodynamic characteristics of gas-solid tapered fluidized beds: Experimental studies and empirical models. *Powder Technology*, *283*, 355–367. doi: 10.1016/j.powtec.2015.06.002

Raza, N., Ahsan, M., Mehran, M. T., Naqvi, S. R., & Ahmad, I. (2021). Computational analysis of the hydrodynamic behavior for different air distributor designs of fluidized bed gasifier. *Frontiers in Energy Research*, *9*, 692066.

Reed, R., Prausnitz, J., & Sherwood, T. (1977). The properties of gases and liquids. *McGraw-Hill, New York.*

Reina, J., Velo, E., & Puigjaner, L. (2000). Predicting the minimum fluidization velocity of polydisperse mixtures of scrap-wood particles. *Powder Technology*, *111*(3), 245–251. doi: 10.1016/S0032-5910(00)00226-6

Rezrazi, A., Hanini, S., & Laidi, M. (2016). An optimisation methodology of artificial neural network models for predicting solar radiation: a case study. *Theoretical and Applied Climatology*, *123*(3–4), 769–783. doi: 10.1007/s00704-015-1398-x

Roubehie Fissa, M., Lahiouel, Y., Khaouane, L., & Hanini, S. (2019). QSPR estimation models of normal boiling point and relative liquid density of pure hydrocarbons using MLR and MLP-ANN methods. *Journal of Molecular Graphics and Modelling*, *87*, 109–120. doi:

10.1016/j.jmgm.2018.11.013

Saleh, E. A., Khaouane, L., Hanini, S., & Laidi, M. (2023). Development of Novel Dimensionless Parameters for Accurate Estimation of Properties in Fluidized Beds. *Iranian Journal of Chemistry and Chemical Engineering*.

Salehi, R., Rahimzadeh, H., Heidarian, P., & Salimi, F. (2023). An AI-Based Modelling of a Sorption Enhanced Chemical-Looping Methane Reforming Unit. *Iran. J. Chem. Chem. Eng. Research Article Vol*, *42*(7).

San José, M. J., Olazar, M., Alvarez, S., & Bilbao, J. (1998). Local bed voidage in conical spouted beds. *Industrial and Engineering Chemistry Research*, *37*(6), 2553–2558. doi: 10.1021/ie9707681

Sau, D. C., Mohanty, S., & Biswal, K. C. (2007). Minimum fluidization velocities and maximum bed pressure drops for gas-solid tapered fluidized beds. *Chemical Engineering Journal*, *132*(1–3), 151–157. doi: 10.1016/j.cej.2007.01.036

Shabanian, J., Jafari, R., & Chaouki, J. (2012). Fluidization of Ultrafine Powders. *International Review of Chemical Engineering*, *4*(1), 16–50.

Shahrbabaki, A. S., Kalantar, V., & Mansouri, S. H. (2023). Analytical and numerical considerations of the minimum fluidization velocity of the molybdenite particles. *Computational Particle Mechanics*, *10*(4), 769–776.

Shao, Y., Li, Z., Zhong, W., Bian, Z., & Yu, A. (2020). Minimum fluidization velocity of particles with different size distributions at elevated pressures and temperatures. *Chemical Engineering Science*, *216*, 115555.

Shaul, S., Rabinovich, E., & Kalman, H. (2012). Generalized flow regime diagram of fluidized beds based on the height to bed diameter ratio. *Powder Technology*, *228*, 264–271. doi: 10.1016/j.powtec.2012.05.029

Shu, J., Lakshmanan, V. I., & Dodson, C. E. (2000). Hydrodynamic study of a toroidal fluidized bed reactor. *Chemical Engineering and Processing: Process Intensification*, *39*(6), 499–506. doi: 10.1016/S0255-2701(00)00097-0

Si-Moussa, C., Hanini, S., Derriche, R., Bouhedda, M., & Bouzidi, A. (2008). Prediction of high-pressure vapor liquid equilibrium of six binary systems, carbon dioxide with six esters, using an artificial neural network model. *Brazilian Journal of Chemical Engineering*, *25*(1), 183–199. doi: 10.1590/S0104-66322008000100019

Sutkar, V. S., Deen, N. G., & Kuipers, J. A. M. (2013). Spout fluidized beds: Recent advances in experimental and numerical studies. *Chemical Engineering Science*, *86*, 124–136. doi: 10.1016/j.ces.2012.06.022

Tahmasebpoor, M., Zarghami, R., Sotudeh-Gharebagh, R., & Mostoufi, N. (2015). Characterization of fluidized beds hydrodynamics by recurrence quantification analysis and wavelet transform. *International Journal of Multiphase Flow*, *69*, 31–41.

Tangier, J. L., Benelmir, R., & El Ganaoui, M. (2012). Fluidisation de particules de bois en lit mixte: faisabilité et contrôle du procédé. *Mechanics and Industry*, *13*(1), 69–76. doi:

10.1051/meca/2012001

Tannous, K., Hemati, M., & Laguerie, C. (1994). POWDER Caractkristiques au minimum de fluidisation et expansion des couches fluidisees de particules de la catkgorie D de Geldart. In Powder Technology (Vol. 80).

Turki, D., & Fatah, N. (2008). Behavior and fluidization of the cohesive powders: Agglomerates sizes approach. *Brazilian Journal of Chemical Engineering*, *25*(4), 697–711. doi: 10.1590/S0104-66322008000400007

Vaferi, B., Karimi, M., Azizi, M., & Esmaeili, H. (2013). Comparison between the artificial neural network, SAFT and PRSV approach in obtaining the solubility of solid aromatic compounds in supercritical carbon dioxide. *The Journal of Supercritical Fluids*, *77*, 44–51.

Vaferi, B., Rahnama, Y., Darvishi, P., Toorani, A., & Lashkarbolooki, M. (2013). Phase equilibria modeling of binary systems containing ethanol using optimal feedforward neural network. *The Journal of Supercritical Fluids*, *84*, 80–88.

Vaferi, B., Samimi, F., Pakgohar, E., & Mowla, D. (2014). Artificial neural network approach for prediction of thermal behavior of nanofluids flowing through circular tubes. *Powder Technology*, *267*, 1–10.

Vandeputte, T., Ghijs, M., Nopens, I., & De Beer, T. (2023). A Colourful Way to Unravel the Important Fluidization-Related Granule Size Effect on Semi-Continuous Drying. *AAPS PharmSciTech*, *25*(1), 11.

Vitesse Minimale de Fluidisation et Expansion des Couches Fluidisks par UnGaZ V_ THONGLIMP, N. HIQUILY et C. LAGUERIE. (n.d.).

Wang, D., Lian, B., Wang, X., Chen, X., Wang, J., & Wang, F. (2023). Influence of rheological characteristics on the fluidization catastrophe of tailings flows. *Journal of Mountain Science*, *20*(9), 2628–2643.

Wang, J., Shao, Y., & Zhu, J. (2023). Improving flow and fluidization quality of fine and ultrafine particles via nanoparticle modulation. *Nano Research*, *16*(10), 12013–12025.

Weber, J. M., & Mei, J. S. (2013). Bubbling fluidized bed characterization using electrical capacitance volume tomography (ECVT). *Powder Technology*, *242*, 40–50. doi: 10.1016/j.powtec.2013.01.044

Wen, C. Y., & Yu, Y. H. (1966). A generalized method for predicting the minimum fluidization velocity. *AIChE Journal*, *12*(3), 610–612.

Wong, A. C. Y. (2002). Use of angle of repose and bulk densities for powder characterization and the prediction of minimum fluidization and minimum bubbling velocities. *Chemical Engineering Science*, *57*(14), 2635–2640. doi: 10.1016/S0009-2509(02)00150-1

Xu, C. C., & Zhu, J. (2009). Prediction of the minimum fluidization velocity for fine particles of various degrees of cohesiveness. *Chemical Engineering Communications*, *196*(4), 499–517. doi: 10.1080/00986440802483855

Yates, J. G. (1988). Gas fluidization technology. *The Chemical Engineering Journal*, *37*(2), 134–

135. doi: 10.1016/0300-9467(88)80042-x

Yates, J. G., & Simons, S. J. R. (1994). Experimental methods in fluidization research. *International Journal of Multiphase Flow*, *20*(SUPPL. 1), 297–330. doi: 10.1016/0301-9322(94)90076-0

Zardari, B. A. (2023). *Artificial Neural Networks : An Overview Artificial Neural Networks : An Overview*. *August*. doi: 10.58496/MJCSC/2023/015

Zhang, J., Qian, W., Lu, J., & Chen, G. (2022). Fluidization Prediction of Liquefiable Cargo: Based on FINN and UBCSAND Constitutive Models. *Journal of Marine Science and Application*, *21*(2), 210–227.

Zhou, D., Dong, S., Wang, H., & Bi, H. T. (2009). Minimum fluidization velocity of a three-phase conical fluidized bed in comparison to a cylindrical fluidized bed. *Industrial and Engineering Chemistry Research*, *48*(1), 27–36. doi: 10.1021/ie8001974

Zhou, Y., & Zhu, J. (2019). Group C+ particles: Enhanced flow and fluidization of fine powders with nano-modulation. *Chemical Engineering Science*, *207*, 653–662. doi: 10.1016/j.ces.2019.06.056

Zhou, Y., & Zhu, J. (2020). Prediction of dense phase voidage for group C+ fluidized bed reactor. *Chemical Engineering Journal*, *402*(July), 126217. doi: 10.1016/j.cej.2020.126217

Appendix

Appendix A. Part of the database used in this work.

A_r	π_1	π_2	U_{mf}	ΔP_{max}
372.52	0.00015173	0.00027456	0.05596235	1.5434507
372.52	6.3526E-05	0.00017766	0.05630251	1.56430614
372.52	2.2134E-05	0.00010487	0.05656059	1.57995981
372.52	8.2524E-06	6.4032E-05	0.05670635	1.58873412
795.74	0.0001424	0.00026141	0.07123618	1.8027308
795.74	5.962E-05	0.00016915	0.07176339	1.82242617
795.74	2.0773E-05	9.9845E-05	0.07216322	1.83706414
795.74	7.745E-06	6.0966E-05	0.07238898	1.84521514
1632.24	0.00013364	0.00024894	0.10380981	2.0656557
1632.24	5.5953E-05	0.00016108	0.10480413	2.08394242
1632.24	1.9496E-05	9.5082E-05	0.10555883	2.09733868
1632.24	7.2686E-06	5.8057E-05	0.10598518	2.10472601
3670.98	0.00012541	0.00023711	0.14457648	2.06822277
3670.98	5.2509E-05	0.00015342	0.14579497	2.08491721
3670.98	1.8296E-05	9.0561E-05	0.14671636	2.09714856
3670.98	6.8212E-06	5.5297E-05	0.14723554	2.1038946
372.52	0.00051	0.00050338	0.05517442	1.4942197
372.52	0.00021353	0.00032571	0.05578435	1.5324392
372.52	7.44E-05	0.00019226	0.05625099	1.56116375
372.52	2.7739E-05	0.0001174	0.05651601	1.57726671
795.74	0.00047864	0.00047927	0.07001405	1.75535241
795.74	0.0002004	0.00031012	0.07096021	1.79224233
795.74	6.9825E-05	0.00018306	0.07168356	1.81947287
795.74	2.6033E-05	0.00011177	0.07209417	1.83455452
1632.24	0.0004492	0.00045641	0.10150848	2.02044327
1632.24	0.00018807	0.00029532	0.10328969	2.05579505
1632.24	6.553E-05	0.00017432	0.10465351	2.0812194
1632.24	2.4432E-05	0.00010644	0.10542846	2.09505386
3670.98	0.00042155	0.00043471	0.14173593	2.0269346
3670.98	0.0001765	0.00028128	0.14393699	2.05922036
3670.98	6.1497E-05	0.00016603	0.14561074	2.08243128
3670.98	2.2928E-05	0.00010138	0.14655739	2.09506215
372.52	0.00157944	0.00088585	0.0539038	1.4124445
372.52	0.00066129	0.00057319	0.05493819	1.47922537
372.52	0.00023041	0.00033834	0.05574057	1.52972051
372.52	8.5905E-05	0.00020659	0.05620053	1.55807993
795.74	0.00148233	0.00084343	0.06804062	1.67384519

A_r	π_1	π_2	U_{mf}	ΔP_{max}
14197.13	7.9953E-06	7.2967E-05	0.18993124	1.63812065
29984.71	0.00010688	0.00025731	0.25189687	1.67830857
29984.71	4.6966E-05	0.00017057	0.2513596	1.67598165
29984.71	1.8208E-05	0.0001062	0.25095924	1.67423883
29984.71	7.079E-06	6.622E-05	0.25070982	1.67314925
4088.62	0.00047779	0.000608	0.12098418	1.37319526
4088.62	0.00020994	0.00040303	0.12387051	1.44640852
4088.62	8.1392E-05	0.00025095	0.12605686	1.50069169
4088.62	3.1644E-05	0.00015647	0.12743429	1.53425931
8123.27	0.00042251	0.00055045	0.15947447	1.46649996
8123.27	0.00018565	0.00036488	0.16230251	1.52913872
8123.27	7.1974E-05	0.00022719	0.16443299	1.57531295
8123.27	2.7983E-05	0.00014166	0.16577021	1.60378192
14197.13	0.00037386	0.00049896	0.18417356	1.52129858
14197.13	0.00016428	0.00033075	0.18642423	1.56770075
14197.13	6.3688E-05	0.00020594	0.18811346	1.60192915
14197.13	2.4761E-05	0.00012841	0.18917105	1.62307036
29984.71	0.00033101	0.00045282	0.25309801	1.68346074
29984.71	0.00014545	0.00030017	0.2521613	1.67944879
29984.71	5.6388E-05	0.0001869	0.25146093	1.67642156
29984.71	2.1923E-05	0.00011654	0.25102361	1.67451953
16524.65	2.1906E-05	0.00013711	0.16845143	1.13236663
16524.65	1.1235E-05	9.8192E-05	0.16887159	1.141161
16524.65	4.4815E-06	6.2016E-05	0.16926329	1.14937935
16524.65	2.2929E-06	4.436E-05	0.16945487	1.15340559
26036.6	1.9091E-05	0.00012255	0.21001474	1.24276009
26036.6	9.7909E-06	8.7766E-05	0.21016269	1.2459122
26036.6	3.9055E-06	5.5431E-05	0.21030039	1.24884782
26036.6	1.9982E-06	3.965E-05	0.21036766	1.25028261
43599.86	1.6654E-05	0.00010973	0.25093138	1.39477999
43599.86	8.5414E-06	7.8581E-05	0.2510629	1.39710747
43599.86	3.4071E-06	4.963E-05	0.25118523	1.39927199
43599.86	1.7432E-06	3.55E-05	0.25124497	1.40032881
60995.96	1.4544E-05	9.8413E-05	0.27417741	1.37643453
60995.96	7.4591E-06	7.0478E-05	0.27432045	1.37881365
60995.96	2.9754E-06	4.4512E-05	0.27445347	1.38102611
60995.96	1.5223E-06	3.1839E-05	0.27451842	1.3821063
16524.65	7.3633E-05	0.00025138	0.16722519	1.10683776

A_r	π_1	π_2	U_{mf}	ΔP_{max}
13102.6	0.00022839	0.00036278	0.19011172	1.68904112
13102.6	5.9476E-05	0.00018513	0.1927233	1.73838547
13102.6	2.9385E-05	0.00013013	0.19353931	1.75343734
595.43	51390.0996	2.10189037	0.0174	0.5069047
418.53	51390.0996	2.10189037	0.0174	0.41535534
308.94	51390.0996	2.10189037	0.0174	0.38845116
595.43	11624.679	0.99967957	0.03279635	1.05380751
418.53	11624.679	0.99967957	0.03024834	1.01725969
308.94	11624.679	0.99967957	0.02874568	0.95283463
595.43	4770.77279	0.64041972	0.03087175	1.86326635
418.53	4770.77279	0.64041972	0.02951728	1.76292175
308.94	4770.77279	0.64041972	0.02861735	1.63597891
8449.8	13022.6766	1.05808476	0.2031231	0.63483855
5939.31	13022.6766	1.05808476	0.15812558	0.67489867
4384.14	13022.6766	1.05808476	0.11602298	0.72694854
8449.8	2191.85089	0.43408606	0.17526238	1.14246383
5939.31	2191.85089	0.43408606	0.15232144	0.98487765
4384.14	2191.85089	0.43408606	0.11523383	0.73254662
8449.8	813.917286	0.26452119	0.20795038	2.04649193
5939.31	813.917286	0.26452119	0.17465302	1.96081663
4384.14	813.917286	0.26452119	0.14223463	1.86124262
67598.42	2083.62825	0.4232339	0.61849581	0.7735386
47514.52	2083.62825	0.4232339	0.49806974	0.77860587
35073.09	2083.62825	0.4232339	0.48447479	0.77352128
67598.42	547.962723	0.21704303	0.6353361	1.52268844
47514.52	547.962723	0.21704303	0.53119211	1.41575781
35073.09	547.962723	0.21704303	0.47832321	1.40466087
67598.42	223.985837	0.13876521	0.64984243	2.22698919
47514.52	223.985837	0.13876521	0.56237099	2.15304144
35073.09	223.985837	0.13876521	0.50154279	2.13631044
595.43	48852.7134	2.04934311	0.0174	0.43377157
418.53	48852.7134	2.04934311	0.0174	0.41863652
308.94	48852.7134	2.04934311	0.0174	0.41319418
595.43	11624.679	0.99967957	0.03279635	1.05380751
418.53	11624.679	0.99967957	0.03024834	1.01725969
308.94	11624.679	0.99967957	0.02874568	0.95283463
595.43	4923.4279	0.65058512	0.03066102	1.79267935

A_r	π_1	π_2	U_{mf}	ΔP_{max}
4384.14	881.434385	0.27527408	0.14688166	1.91929161
67598.42	2191.85089	0.43408606	0.61838504	0.7700581
47514.52	2191.85089	0.43408606	0.49716728	0.76811809
35073.09	2191.85089	0.43408606	0.48541127	0.76818633
67598.42	520.907063	0.21161695	0.63237146	1.45335775
47514.52	520.907063	0.21161695	0.53330362	1.46451367
35073.09	520.907063	0.21161695	0.47929188	1.45176255
67598.42	209.99025	0.13435997	0.64721361	2.19973559
47514.52	209.99025	0.13435997	0.55961255	2.15034362
35073.09	209.99025	0.13435997	0.50331071	2.16902011
595.43	44310.8511	1.95175535	0.0174	0.44465489
418.53	44310.8511	1.95175535	0.0174	0.47630483
308.94	44310.8511	1.95175535	0.0174	0.49915075
595.43	12213.1783	1.02467156	0.02966593	1.06317794
418.53	12213.1783	1.02467156	0.02743723	1.01313634
308.94	12213.1783	1.02467156	0.02614241	0.93571063
595.43	5428.07926	0.68311437	0.03078251	1.72096977
418.53	5428.07926	0.68311437	0.02945369	1.64705372
308.94	5428.07926	0.68311437	0.02858479	1.54821248
8449.8	8334.51301	0.84646781	0.17171763	0.63493623
5939.31	8334.51301	0.84646781	0.12655445	0.57972419
4384.14	8334.51301	0.84646781	0.09702558	0.60349108
8449.8	2083.62825	0.4232339	0.17996869	1.2749043
5939.31	2083.62825	0.4232339	0.1581343	1.16629765
4384.14	2083.62825	0.4232339	0.13996007	1.26169978
8449.8	813.917286	0.26452119	0.20795038	2.04649193
5939.31	813.917286	0.26452119	0.17465302	1.96081663
4384.14	813.917286	0.26452119	0.14223463	1.86124262
67598.42	1889.91225	0.40307991	0.61876369	0.78148325
47514.52	1889.91225	0.40307991	0.49948211	0.79691924
35073.09	1889.91225	0.40307991	0.48264666	0.78577012
67598.42	520.907063	0.21161695	0.63237146	1.45335775
47514.52	520.907063	0.21161695	0.53330362	1.46451367
35073.09	520.907063	0.21161695	0.47929188	1.45176255
67598.42	209.99025	0.13435997	0.64721361	2.19973559
47514.52	209.99025	0.13435997	0.55961255	2.15034362
35073.09	209.99025	0.13435997	0.50331071	2.16902011

A_r	π_1	π_2	U_{mf}	ΔP_{max}
595.43	48852.7134	2.04934311	0.0174	0.43377157
418.53	48852.7134	2.04934311	0.0174	0.41863652
308.94	48852.7134	2.04934311	0.0174	0.41319418
595.43	11077.7128	0.97587767	0.03562952	1.06558291
418.53	11077.7128	0.97587767	0.0328737	1.04282829
308.94	11077.7128	0.97587767	0.03122692	0.98985795
595.43	4923.4279	0.65058512	0.03066102	1.79267935
418.53	4923.4279	0.65058512	0.02934368	1.69876014
308.94	4923.4279	0.65058512	0.02847041	1.5786809
8449.8	9234.91746	0.89101875	0.18900293	0.63561693
5939.31	9234.91746	0.89101875	0.14989428	0.62935008
4384.14	9234.91746	0.89101875	0.11688512	0.64519627
8449.8	2136.7122	0.4285913	0.17773659	1.21157589
5939.31	2136.7122	0.4285913	0.15542682	1.07948135
4384.14	2136.7122	0.4285913	0.13544732	1.17577629
8449.8	813.917286	0.26452119	0.20795038	2.04649193
5939.31	813.917286	0.26452119	0.17465302	1.96081663
4384.14	813.917286	0.26452119	0.14223463	1.86124262
67598.42	2308.72937	0.44550937	0.61828708	0.7668412
47514.52	2308.72937	0.44550937	0.49612805	0.7562455
35073.09	2308.72937	0.44550937	0.48635313	0.76333799
67598.42	483.93166	0.20396815	0.63346269	1.5182754
47514.52	483.93166	0.20396815	0.53645747	1.53772251
35073.09	483.93166	0.20396815	0.48083048	1.52144635
67598.42	203.479322	0.1322606	0.64520649	2.1746362
47514.52	203.479322	0.1322606	0.55726874	2.14084598
35073.09	203.479322	0.1322606	0.50416144	2.18389981

Appendix B Additional results were obtained using the STATISTICA 10 software.

Ar =A_r

Pi1 = π_1

Pi2 = π_2

U = U_{mf}

DP = ΔP_{max}

Summary of active networks (Spreadsheet2)							
Index	Net. name	Training perf.	Test perf.	Validation perf.	Training error	Test error	Validation error
1	MLP 3-16-2	0.908834	0.846606	0.914633	0.034425	0.051966	0.029940

	Network weights (Spreadsheet2)	
Weight ID	Connections 1.MLP 3-16-2	Weight values 1.MLP 3-16-2
1	Ar --> hidden neuron 1	1.4235
2	pi1 --> hidden neuron 1	10.7392
3	pi2 --> hidden neuron 1	-16.2815
4	Ar --> hidden neuron 2	1.3881
5	pi1 --> hidden neuron 2	-6.7260
6	pi2 --> hidden neuron 2	-21.4012
7	Ar --> hidden neuron 3	1.7659
8	pi1 --> hidden neuron 3	-10.3798
9	pi2 --> hidden neuron 3	-19.6215
10	Ar --> hidden neuron 4	3.5637
11	pi1 --> hidden neuron 4	-4.6952
12	pi2 --> hidden neuron 4	-4.1261
13	Ar --> hidden neuron 5	3.0000
14	pi1 --> hidden neuron 5	-5.9130
15	pi2 --> hidden neuron 5	-9.6185
16	Ar --> hidden neuron 6	-0.6422
17	pi1 --> hidden neuron 6	-23.1656
18	pi2 --> hidden neuron 6	2.3937
19	Ar --> hidden neuron 7	-48.4580
20	pi1 --> hidden neuron 7	-15.6011
21	pi2 --> hidden neuron 7	8.4070
22	Ar --> hidden neuron 8	4.8580
23	pi1 --> hidden neuron 8	-1.9311
24	pi2 --> hidden neuron 8	0.2709
25	Ar --> hidden neuron 9	0.5774
26	pi1 --> hidden neuron 9	-5.8086
27	pi2 --> hidden neuron 9	-0.2410
28	Ar --> hidden neuron 10	5.1902
29	pi1 --> hidden neuron 10	2.2689
30	pi2 --> hidden neuron 10	-3.2203
31	Ar --> hidden neuron 11	5.9428
32	pi1 --> hidden neuron 11	3.5242
33	pi2 --> hidden neuron 11	-1.9236
34	Ar --> hidden neuron 12	0.2250
35	pi1 --> hidden neuron 12	3.8039
36	pi2 --> hidden neuron 12	-3.9015
37	Ar --> hidden neuron 13	0.3127
38	pi1 --> hidden neuron 13	3.2473
39	pi2 --> hidden neuron 13	-5.7648
40	Ar --> hidden neuron 14	3.1799
41	pi1 --> hidden neuron 14	0.0720
42	pi2 --> hidden neuron 14	-2.9679
43	Ar --> hidden neuron 15	1.5960

	Correlation coefficients (Spreadsheet2)					
	U Train	U Test	U Validation	DP Train	DP Test	DP Validation
1.MLP 3-16-2	0.977314	0.982111	0.975653	0.840354	0.711100	0.853612

	Predictions statistics (Spreadsheet2) Target: U
Statistics	1.MLP 3-16-2
Minimum prediction (Train)	0.022283
Maximum prediction (Train)	0.574789
Minimum prediction (Test)	0.023087
Maximum prediction (Test)	0.573631
Minimum prediction (Validation)	0.022280
Maximum prediction (Validation)	0.574573
Minimum prediction (Missing)	
Maximum prediction (Missing)	
Minimum residual (Train)	-0.093143
Maximum residual (Train)	0.106587
Minimum residual (Test)	-0.057631
Maximum residual (Test)	0.120760
Minimum residual (Validation)	-0.097453
Maximum residual (Validation)	0.132637
Minimum standard residual (Train)	-0.502011
Maximum standard residual (Train)	0.574468
Minimum standard residual (Test)	-0.252811
Maximum standard residual (Test)	0.529738
Minimum standard residual (Validation)	-0.563206
Maximum standard residual (Validation)	0.766542

Samples	Data statistics (Spreadsheet2) Ar Input	pi1 Input	pi2 Input	U Target	DP Target
Minimum (Train)	371.96	202.8	0.30671	0.017400	0.331400
Maximum (Train)	75694.35	410543.9	14.28193	0.681300	2.479120
Mean (Train)	19457.87	33618.4	3.75294	0.191856	1.411522
Standard deviation (Train)	25667.76	54266.5	2.90545	0.159769	0.480943
Minimum (Test)	371.96	207.6	0.31224	0.023400	0.470200
Maximum (Test)	75694.35	102636.0	7.14096	0.687700	2.242900
Mean (Test)	20282.28	17584.0	2.83767	0.187860	1.473463
Standard deviation (Test)	25560.05	21409.0	1.73462	0.161119	0.452168
Minimum (Validation)	666.75	467.6	0.47319	0.022600	0.459500
Maximum (Validation)	75694.35	116059.5	9.70393	0.634700	2.517710
Mean (Validation)	25322.46	18056.6	2.89893	0.218616	1.412655
Standard deviation (Validation)	23934.30	93059.9	3.49773	0.132111	0.523424
Minimum (Missing)					
Maximum (Missing)					
Mean (Missing)					
Std (Missing)					
Minimum (Overall)	371.96	202.8	0.30671	0.017400	0.331400
Maximum (Overall)	75694.35	410543.9	14.28193	0.687700	2.517710
Mean (Overall)	20460.19	28883.8	3.48782	0.195267	1.420973
Standard deviation (Overall)	26060.48	47631.9	2.66003	0.160959	0.473686

Networks	Sensitivity analysis (Spreadsheet2) Samples: Train, Test, Validation pi1	pi2	Ar
1.MLP 3-16-2	15.43810	13.34051	2.777423